Predicting the future: Predictive control for astronomical adaptive optics

Kooten M.A.M. van

Author: Kooten, M.A.M. van
Title: Predicting the future: Predictive control for astronomical adaptive optics
Issue Date: 2020-11-04

Predicting the Future

Predictive Control for Astronomical Adaptive Optics

Maaike A. M. van Kooten

Front cover design was made from simulated phase screen of full atmospheric turbulence and a residual phase screen using predictive control. I enjoy watercolor painting as a hobby and used a watercolor effect to create the final cover design.

Predicting the Future

Predictive Control for Astronomical Adaptive Optics

Proefschrift

ter verkrijging van
de graad van Doctor aan de Universiteit Leiden,
op gezag van de Rector Magnificus prof. mr. C.J.J.M. Stolker;
volgens besluit van het College voor Promoties,
te verdedigen op 4 november 2020
klokke 16:15 uur

door

Maaike Anna Maria van Kooten

geboren te Richmond, Canada
in 1992

Promotiecommissie:

Promotor: Prof.dr.ir. N. Doelman
Copromotor: Dr.ir. M. Kenworthy

Overige leden:

Prof.dr. H. Rottgering	Leiden Universiteit
Prof.dr. C. Keller	Leiden Universiteit
Prof.dr. B. R. Brandl	Leiden Universiteit
Dr.ir. G. Witvoet	Technische Universiteit Eindhoven
Dr. S. Kendrew	European Space Agency

Keywords: adaptive optics, control, prediction, turbulence

ISBN 978-94-6361-467-2

An electronic copy of this thesis can be found at https://openaccess.leidenuniv.nl

To my husband for his limitless support and dedication.

"It's a dangerous business, going out your door. You step onto the road, and if you don't keep your feet, there's no knowing where you might be swept off to".

J.R.R. Tolkien,
The Fellowship of the Ring

Acknowledgements

> “For the Quest is achieved, and now all is over. I am glad you are here with me. Here at the end of all things”
>
> J.R.R. Tolkien, *The Return of the King*

At the end of a PhD I can now proudly declare that I am an independent researcher ready to head out into academia and make contributions to my field. Yet, I am most definitely not a self-standing researcher, but rely on my peers, colleagues, friends, and family to not only support me but to inspire me. Without the people around me, my work would not only be impossible, but also not as much fun.

Without my peers and colleagues—David, Steven, Emiel, Sebastiaan, Kelsey, Alex and so many more—this dissertation would not have been possible. I am thankful for all the support, knowledge, conversation, and laughter you have supplied. I have enjoyed our coffee times, group meetings, conference trips, and daily office life. I have learned so much from you all.

My supervisors, Niek and Matt, have both guided me in my research as well as my future career. Thank you for giving me the opportunity to work with you. Thank you for treating me as an equal while at the same time gently guiding me to successfully completing my PhD. I look forward to our future collaborations.

To my friends, thank you for constantly inspiring and supporting me. Doing life together, sharing our successes and failures, laughing together, and learning from each other. Thank you all for welcoming me into your lives and becoming a great support system in the Netherlands.

To my family, thank you for putting up with a stressed-out bachelor student that often put her school work ahead of her family. To my younger sister Emma, thanks for putting up with me. Mom and Dad, thank you for always believing in and encouraging me to go for it. Mom, thank you for trying to teach me work-life balance! Dad, you are an inspiration. Now I can truly appreciate all the hard work you put in as a professor growing up and be in awe of your publication record.

Last but definitely not the least, thank you to my husband who has been my most constant support and advisor. Jon thank you for all the in depth discussion and debates. I am so grateful I can discuss and share my work with you. We are here together at the end of our PhDs. "I am glad you are here with me. Here at the end of all things, [Jon]”

Contents

Summary

The field of exoplanet research is rapidly advancing through the development of new technology, observing techniques, and post-processing methods. In the last 30 years, thousands of exoplanet candidates have been found through various methods. These discoveries have revealed a zoo of exoplanetary systems looking very different from our own Solar System; orbital period, mass, and radius can all vary greatly from system to system. This dissertation contains two very distinctive parts, both related to the measurement of exoplanetary systems.

The first part of this dissertation, Chapter 2, investigates 8 light curves (flux of a star as a function of time) found in the Kepler data archive. These light curves show periodic brightening events that look different from a normal exoplanet signal (which typically shows a decrease in light intensity). To understand what these signals might be, we investigate two possible mechanisms to explain the observed light curves, namely: forward scattering from an optically thin dust cloud, and tidal interactions from a close binary star system. From modelling and fitting to the data, we find that both of these models can explain the observed data. To truly determine if the signals are due to a binary star system or possibly a dust cloud around a star radial velocity data would be needed.

The second part of this dissertation, Chapters 3 through 6, focuses on high-contrast imaging (HCI) that spatially separates the stellar light from that of the orbiting exoplanet. Current HCI instruments are more sensitive to exoplanets orbiting far out from their host star. To probe the regions close-in to the star, the extreme adaptive optics (XAO) system needs to improve in performance. An XAO system aims to correct for any aberrations of the phase of the incoming light in real-time. However, some residual phase disturbance remains in the corrected signal due, in part, to the continuous evolution of turbulence during the time it takes the XAO to measure the phase and subsequently correct for the aberrations (or the so-called servo-lag). The variance of this residual disturbance needs to be minimised. This servo-lag error typically results in a butterfly pattern near the star in the image plane, preventing HCI from achieving the necessary contrasts to image close-in exoplanets. This dissertation focuses on data-driven predictive control to address the servo-lag error.

We first investigate why current efforts in prediction have not led to the expected gains in performance when comparing simulation results to on-sky tests. We specifically study what effects could be missing from current simulations that might explain the differences. All simulations performed for adaptive optics control do not include any non-stationary behaviour of atmospheric turbulence that is a main source of phase aberrations. In simulations with time-varying turbulence caused by varying wind speed, we demonstrate that an XAO system loses performance. For a standard integral controller, sub-second wind speed fluctuations affect contrast by less than 5%. Wind speed changes on longer timescales, however, lead to a much larger loss in contrast than theoretically expected. A linear data-driven predictor will also lose performance due to the inability to track the varying statistics compared to its optimal implementation. With the understanding of how prediction performs in simulation under time varying conditions, we apply a linear data-driven predictor to VLT/SPHERE XAO telemetry. We find for the 27 various observing conditions studied, the predictive control XAO correction is more reliable and consistent. The optical turbulence, however, as seen by VLT/SPHERE appears to be time-invariant. We also find that using previous states of the phase at a given point in space as input to the predictor has a larger impact than providing the predictor knowledge about neighbouring measurements.

As HCI systems are being built for the next generation of large telescopes, it is necessary to fully understand the relation between atmospheric turbulence, predictive control, and contrast. To do this, it is imperative to first understand the main differences in the performance of linear prediction at various observatory locations. This requires a good understanding of the telescopes, their instruments and the full implementation of their controllers, as well as the atmosphere above the observatories. At specific sites, different predictive control schemes might be better suited due to the statistical behaviour of atmosphere, telescope vibrations, etc. Since the raw contrast is the critical performance index for HCI, determining whether predictive control can be used to directly optimise the raw contrast is an interesting research direction. Another crucial step for XAO control is to have flexible instruments and telescope facilities to allow for the testing of new control schemes for further development. Being able to test controllers in real-life situations under a variety of conditions is invaluable. By looking into the topics outlined above, the control community can provide the best performance for HCI systems such that the contrast at smaller angular resolutions will allow for the imaging, and subsequent characterisation, for far away and close-in exoplanets.

Samenvatting

Onderzoek naar exoplaneten vordert snel doordat er veel ontwikkelingen zijn in nieuwe technologieën, waarneemtechnieken, en data reductie. In de laatste 30 jaar zijn er duizenden kandidaat exoplaneten ontdekt door middel van verschillende methodes. Deze ontdekkingen hebben een dierentuin aan planetaire stelsels onthuld die allemaal erg verschillen met ons eigen Zonnestelsel; omlooptijden, massa, en straal kunnen heel erg verschillen tussen de verschillende systemen. Dit proefschrift behandelt twee onderwerpen, beiden gerelateerd aan waarnemingen van exoplanetaire systemen.

Het eerste deel van het proefschrift onderzoekt 8 lichtkrommes (stellaire flux als functie van tijd) uit het Kepler data archief. Deze lichtkrommes vertonen periodieke helderheids fluctuaties die anders zijn dan signalen die op exoplaneten wijzen (deze vertonen typisch een helderheids vermindering). Om te begrijpen wat deze signalen kunnen zijn onderzoeken we twee mogelijke mechanismen: voorwaartse verstrooiing van een optisch dunne stofwolk en getijden interacties van een dubbelstersysteem dat op korte afstand om zich heen draait. Door middel van modelleren en fitten aan data vinden we dat beiden modellen de waargenomen data kunnen verklaren. Om echt te bepalen of de signalen komen door een dubbelstersysteem of een mogelijke stofwolk rondom een ster zijn er radiale snelheidsgegevens nodig.

Het tweede deel van dit proefschrift richt zich op *high-contrast imaging* (HCI), het vakgebied dat zich richt op het ruimtelijk scheiden van sterlicht en licht afkomstig van een exoplaneet. De huidige HCI-instrumenten zijn het gevoeligst voor exoplaneten die ver weg van hun moederster staan. Om de gebieden dichtbij de ster te onderzoeken moet het extreem adaptieve optica (XAO) systeem verbeterd worden. Een XAO systeem probeert *real-time* fase aberraties in het inkomende licht te corrigeren. Er blijft echter enige restfase-verstoring achter in het gecorrigeerde signaal, gedeeltelijk als gevolg van de evoluerende turbulentie gedurende de tijd die de XAO nodig heeft om de fase aberraties te meten en vervolgens te corrigeren (de zogenaamde de *servo-lag*). De variantie van het verstorings residue moet uiteindelijk geminimaliseerd worden. De *servo-lag* resulteert typisch in een vlinder patroon dichtbij de ster in het beeldvlak, wat ervoor zorgt dat HCI niet het benodigde contrast haalt om exoplaneten die dichtbij hun moederster staan waar te nemen. Dit proefschrift richt zich op datagedreven voorspellende controle om de *servo-lag* fout te corrigeren.

Door middel van het vergelijken van simulatieresultaten met telescoop waarnemingen onderzoeken we eerst waarom de huidige voorspellende controle inspanningen niet hebben geleid tot de verwachte prestatieverbetering. We onderzoeken specifiek welke effecten er ontbreken in huidige simulaties die de verschillen zouden kunnen verklaren. In alle simulaties uitgevoerd voor XAO controle ontbreekt niet-stationair gedrag van atmosferische turbulentie, wat een belangrijke bron is van fase-aberraties. In simulaties waarin de turbulentie in de tijd varieert, veroorzaakt door

een variërende windsnelheid, laten we zien dat de prestaties van een XAO-systeem minder worden. Voor een standaard integrale controller beïnvloeden windfluctuaties van minder dan een seconde het contrast met minder dan 5%. Veranderingen in windsnelheid op langere tijdschalen leiden echter tot een veel groter contrastverlies dan theoretisch voorspeld. Een lineaire datagestuurde voorspeller zal daarom ook minder goed werken, in vergelijking met de optimale implementatie, vanwege het onvermogen om de variërende statistiek te volgen. Met dit inzicht van hoe voorspellende controle presteert in simulatie onder tijdsafhankelijke omstandigheden, passen we een lineaire datagestuurde voorspeller toe op VLT /SPHERE XAO-telemetrie. We vinden dat, voor de 27 verschillende onderzochte observatieomstandigheden, de voorspellende controle XAO-correctie betrouwbaarder en consistenter is. De optische turbulentie, zoals waargenomen door VLT /SPHERE, lijkt echter tijdinvariant te zijn. We vinden ook dat als we de voorspeller tijdelijk gecorreleerde data in plaats van ruimtelijk gecorreleerde data verstrekken dat de kwaliteit beter wordt.

Aangezien op dit moment HCI-systemen worden gebouwd voor de volgende generatie grote telescopen, is het noodzakelijk om de relatie tussen atmosferische turbulentie, voorspellende controle en contrast volledig te begrijpen. Het is noodzakelijk om eerst de belangrijkste verschillen in kwaliteit van lineaire voorspelling op verschillende observatoriumlocaties te begrijpen. Dit vereist een goed begrip van de telescopen, hun instrumenten en de volledige implementatie van hun controllers, evenals de atmosfeer boven de observatoria. Op bepaalde locaties kunnen verschillende voorspellende controleschema's beter geschikt zijn vanwege het statistische gedrag van de atmosfeer, telescooptrillingen, etc. Aangezien het ruwe contrast de kritische prestatie-index is voor HCI, is het bepalen of voorspellende controle kan worden gebruikt om direct het ruwe contrast te optimaliseren een interessante onderzoeksrichting. Een andere cruciale stap om verdere ontwikkeling van XAO-controle mogelijk te maken is het beschikken over flexibele instrumenten en telescoopfaciliteiten om nieuwe controle schema's te testen. Het is van onschatbare waarde om controllers te kunnen testen in realistische situaties onder verschillende omstandigheden. Door de hierboven geschetste onderwerpen te onderzoeken, kan de controlegemeenschap de beste XAO-correctie leveren voor HCI-systemen, zodat het contrast bij kleinere hoekresoluties de beeldvorming en daaropvolgende karakterisering mogelijk maakt voor verre en dichtbij gelegen exoplaneten.

Chapter 1

Introduction

> "The wide world is all about you: you can fence yourselves in, but you cannot for ever fence it out."
>
> J.R.R. Tolkien, *The Fellowship of the Ring*

Giordano Bruno in the 16th century wrote "this space we declare to be infinite... in it are an infinity of worlds of the same kind as our own". Even with these early speculations on the existence of earth-like planets, it was not until the late 1980s that the first signs of a scientific detection of an exoplanet was made by Campbell et al. (1988). Unable to rule out intrinsic stellar variations as the source of the Doppler shifting in the observer radial velocity measurements of Gamma Cephei A., the confirmation of the exoplanet came later by Hatzes et al. (2003). The search for the first detection of an exoplanet continued until Wolszczan and Frail (1992) discovered variations in the period of a pulsar (i.e., pulsar timing method), using the Arecibo radio telescope, revealing two earth-sized planets orbiting a rotating neutron star. Shortly thereafter, 51 Pegasi b was indirectly detected at Haute-Provence Observatory by Mayor and Queloz (1995). The radial velocity measurements revealed a 4 day period hot Jupiter orbiting a main sequence star. Within a relatively short period of time, thousands of detections were subsequently made using primary radial velocity measurements and transit event detections, see Figure 1.1. With new and improved technology, the field of exoplanets has now moved from exoplanet detection to exoplanet characterisation. From a theoretical point of view, the discovery of a diverse population of exoplanets in different stages of their life-cycles, has made the fields of exoplanets and planet formation dynamic and rapidly evolving with many questions yet to be answered. Some of these questions include 1. how unique is our solar system, 2. how do planets form, and 3. is there life on other planets? To answer these questions, more in-depth studies of individual systems are needed for exoplanets in all stages of their evolution. This includes studying systems across a large portion of the electro-magnetic spectrum. Furthermore, the population sample of exoplanets must continue to increase to better understand planet formation and evolution, all the while trying to understand how the Solar System fits into these narratives. The rest of this introduction is dedicated to summarising current methods for detecting and characterising exoplanets; the tools that will help answer these fundamental questions. Specifically, we will explore the current challenges faced in directly imaging exoplanets and motivate the work that follows in this dissertation.

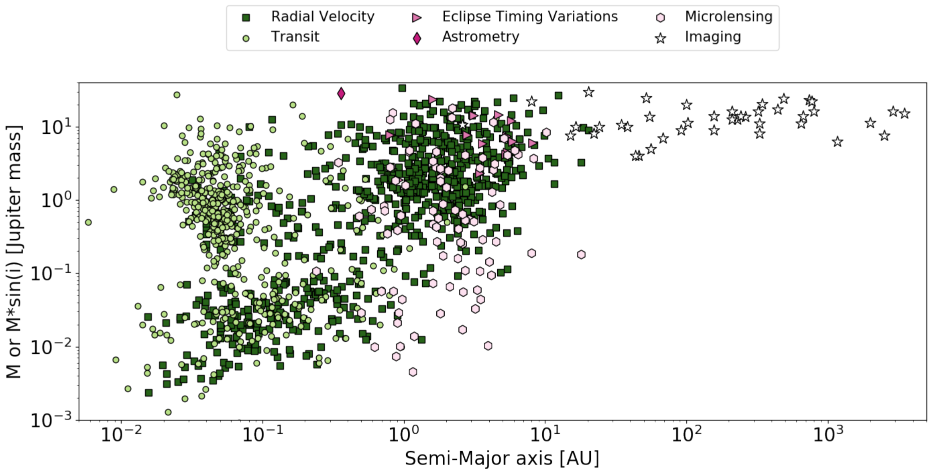

Figure 1.1: Mass or upper-mass limit ($Msin(i)$; for radial velocity only) of exoplanet candidates, sorted by discovery method, as a function of semi-major axis. Data NASA Exoplanet Archive accessed on 13/03/2020.

1.1 Indirect Methods for Detecting Exoplanets

Imaging exoplanets directly is a challenging task due to the required spatial resolution and contrast ($10^{-6} - 10^{-7}$ at separations of < 1 arc-seconds [symbol: "]). As a result, the majority of exoplanets are discovered with indirect techniques. Through indirect methods such as radial velocity measurements, transit photometry, and others (see summary of methods in Table 1.1), thousands of exoplanets have been detected, with their masses and/or radii estimated. Figure 1.1 provides a summary of current exoplanet candidates, categorised by the discovery method. In this section, we will briefly discuss indirect methods before taking an in-depth look at the direct imaging.

Radial Velocity

The radial velocity method—or Doppler spectroscopy—is a spectroscopic method for detecting exoplanets and binary star systems. It relies on taking series of spectra of a given star and finding periodic variations in the spectral time series that are not due to intrinsic stellar variations. The periodic signal is a result of a secondary body "pulling" on the primary body causing slight changes in position and therefore velocity as they orbit their centre of mass. By extracting the amplitude and period of the fluctuation as in Figure 1.2, information on the masses and orbital parameters of the system can be extracted. The method is, however, limited due to the lack of knowledge of the inclination, i, of the system, making it possible to only determine an upper mass limit.

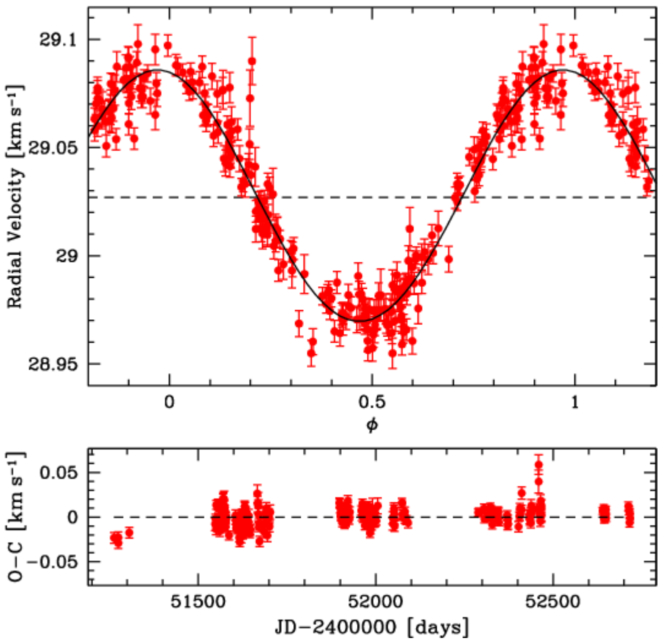

Figure 1.2: Radial velocity measurements (red) for HD 83443 as a function of folded phase with the best Keplerian planetary solution shown in solid. The bottom panel shows the residuals. Figure from Mayor, Udry, et al. (2004).

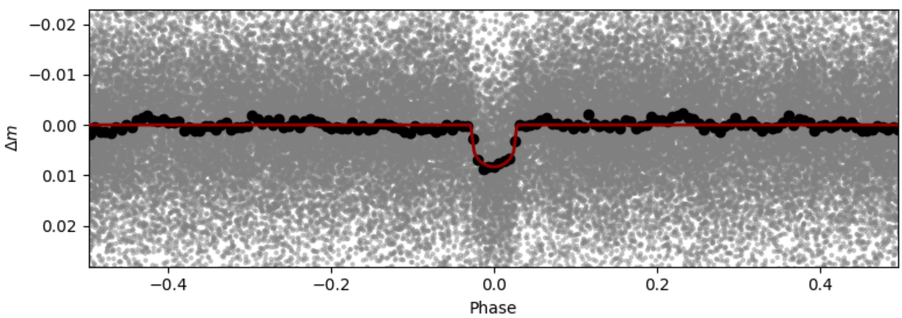

Figure 1.3: MASCARA light curve for the MASCARA-4b exoplanet. The grey points show all of the MASCARA data, while the solid black shows the averaged data. The red curve indicates the best fit. Figure from Dorval et al. (2020).

Table 1.1: Summary of the strengths and weaknesses of different exoplanet detection methods (based on Advanced School on Exoplanetary Science (1st : 2015 : Vietri sul Mare et al. (2016)).

Method	Strengths	Weaknesses
Radial velocity	As follow-up to transit events, allows for exoplanet confirmation; lower-limit mass estimation; get density estimation when combined with transit data	Sensitive to intrinsic stellar variability; bias towards larger close-in exoplanets
Transit photometry	Radius estimation; sensitive to multiple planets; atmosphere characteristics; easy for large surveys	Only sensitive to edge-on systems; measures relative radii; needs to capture multiple transit events; bias towards smaller semi-major-axis
Pulsar timing	Sensitive to all exoplanet masses for non-face-on systems	Very rare due to being a dead system
Microlensing	Sensitive to close-in, earth-like exoplanets	One-time events; unlikely to occur; degeneracies
Astrometry	Independent of stellar type and sensitive to all inclinations	More sensitive to larger, close-in exoplanets; needs well control systematics
Direct imaging	Direct measurement of thermal and/or reflected light; direct characterisation; does not require long baseline	Sensitive to face-on systems; bias towards young, large-separation exoplanets; bias toward nearby systems

Transit Photometry

Charbonneau, Brown, Latham, et al. (2000) detected the first transiting exoplanet, HD 209458b, and since then thousands of transiting exoplanet candidates have been discovered. The transiting method uses precision photometry of a given star over long periods of time. When a planet moves in front of the host star it blocks some of the emitted photons, resulting in a reduction of flux of the star as seen from the observer. The light curve—stellar flux as a function of time—of the recently discovered MASCARA-4b (Dorval et al., 2020) passing in front of its host star is shown in Figure 1.3. The light curve was taken by the Multi-site all-sky camera (MASCARA; Lesage et al. (2014)), a simple ground-based instrument looking for exoplanets with many locations around the world. With space-based telescopes such the

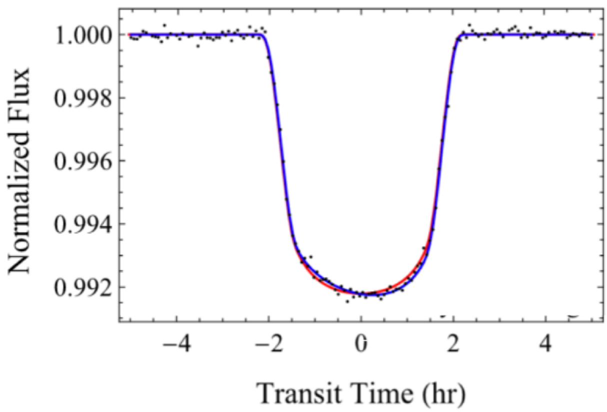

Figure 1.4: Light curve for MASCARA-4b as observed by TESS (black dots) with two different models of the exoplanet. Figure modified from Ahlers et al. (2020).

Kepler telescope (see Borucki et al., 2010) and its successor the Transiting Exoplanet Survey Satellite (TESS; Ricker et al. (2015)), the achievable photometric precision is much better compared to ground-based instruments, allowing the transiting method to discover planets with small radii and therefore relatively smaller masses as seen in Figure 1.1. Figure 1.4 shows the improvement in data quality with the light curve of Mascara-4b taken by TESS published by Ahlers et al. (2020). With telescopes such as Kepler, however, very bright stars are difficult to observe due to detector saturation. Ground-based observations from instruments such as MASCARA will therefore remain important.

The eclipse-timing variations (ETV) approach closely studies the periodicity of a transiting exoplanet, making use of many light curve measurements. In a great number of cases, slight variations in the timing of transits are observed. These variations often result from a transiting exoplanet experiencing the gravitational pull of another as-yet undetected planet, changing the time of the transits slightly. ETV is very effective in tightly packed planetary systems and is sensitive to earth-like masses.

When combined with measurements taken at different wavelengths, the light curve of an exoplanet can provide more information than just the radius and period of the exoplanet. Using transit spectroscopy at the start and end of each transit event (primary eclipse), the light from the host star that travels through the exoplanet's atmosphere can be measured. Some of the light will be absorbed by the atmosphere, allowing the chemical composition of the exoplanet's atmosphere to be inferred from the spectroscopic observation. When the exoplanet passes behind the host star (secondary eclipse), the thermal radiation and reflected light from the planet can be detected as it initially disappears and later reappears, providing information once again about the atmosphere of the exoplanet. Using the Hubble Space Telescope, Charbonneau, Brown, Noyes, et al. (2002) detected a dimming of sodium absorption during an exoplanet's transit, indicative of clouds on the exoplanet. Snellen et al. (2010) found evidence for winds in the upper atmosphere of HD 209458b from transit spectroscopy measurements of carbon monoxide. These discoveries and many others show the power of transit spectroscopy for exoplanet characterisation.

Beyond exoplanet detection

Transiting photometry not only allows for the discovery of exoplanets in an efficient way, but with large surveys such as Kepler, light curves can also be determined for every object in the field-of-view. With this type of data there is a very high potential to detect odd planetary systems that might look very different from what is expected along with signals not due to exoplanets at all. With new efforts to uncover them in archival data by Wheeler and Kipping (2019) and other groups that seek to find outlier signals, new knowledge on planet formation, disk dynamics, or stellar behaviour might be found. Specifically, the discovery of new brightening events in the Kepler data, leads me to ask **what type of astronomical objects could we be seeing in these newly found brightening events?**

1.2 High Contrast Imaging

Using an arsenal of different observing techniques the exoplanet community has primarily relied on indirect methods to detect the effects an exoplanet has on its host star, rather than directly observing the exoplanet itself. In the last 20 years, direct imaging has overcome previous technological barriers to allow for the imaging of the exoplanet itself in reflected light or thermal emission. High-contrast imaging (HCI) enables the direct imaging of exoplanets.

HCI systems image exoplanets by suppressing the light from the host star to reveal the faint exoplanet as shown in Figure 1.6. To date, HCI systems have reached post-processed contrasts of 10^{-6} at spatial separations of 200 milli-arc-second (mas) as determined by Zurlo et al. (2016). *Contrast* is defined as an object's flux compared to its host star's flux in terms of a specified signal-to-noise ratio (SNR). For post-processed images, the post-processed contrast is often defined using $SNR = 5$ or "5σ" detection. The performance of an HCI system is then given in terms of a contrast curve (contrast as a function of radial distance from the centre of the point-spread-function, psf). Since the first HCI detection, 3 exoplanets orbiting HR8799 by Marois, Macintosh, et al. (2008), many large, far out exoplanets have been discovered as shown in Figure 1.1. The orbital periods of the exoplanets around HR8799 range from 45–100 years while the orbital periods of exoplanets, such as 51 Pegasi b mentioned above, are on the order of days. These examples clearly show the different regimes that the methods operate within. HCI systems have also discovered protoplanetary, and circumstellar disks (e.g., Avenhaus et al., 2018; Sissa et al., 2018). By combining direct imaging with high resolution spectroscopy, the exoplanet community is now using HCI to characterize exoplanets. With better understanding of the exoplanets currently seen and the recently imaged disks, a clearer picture of planet formation can be made.

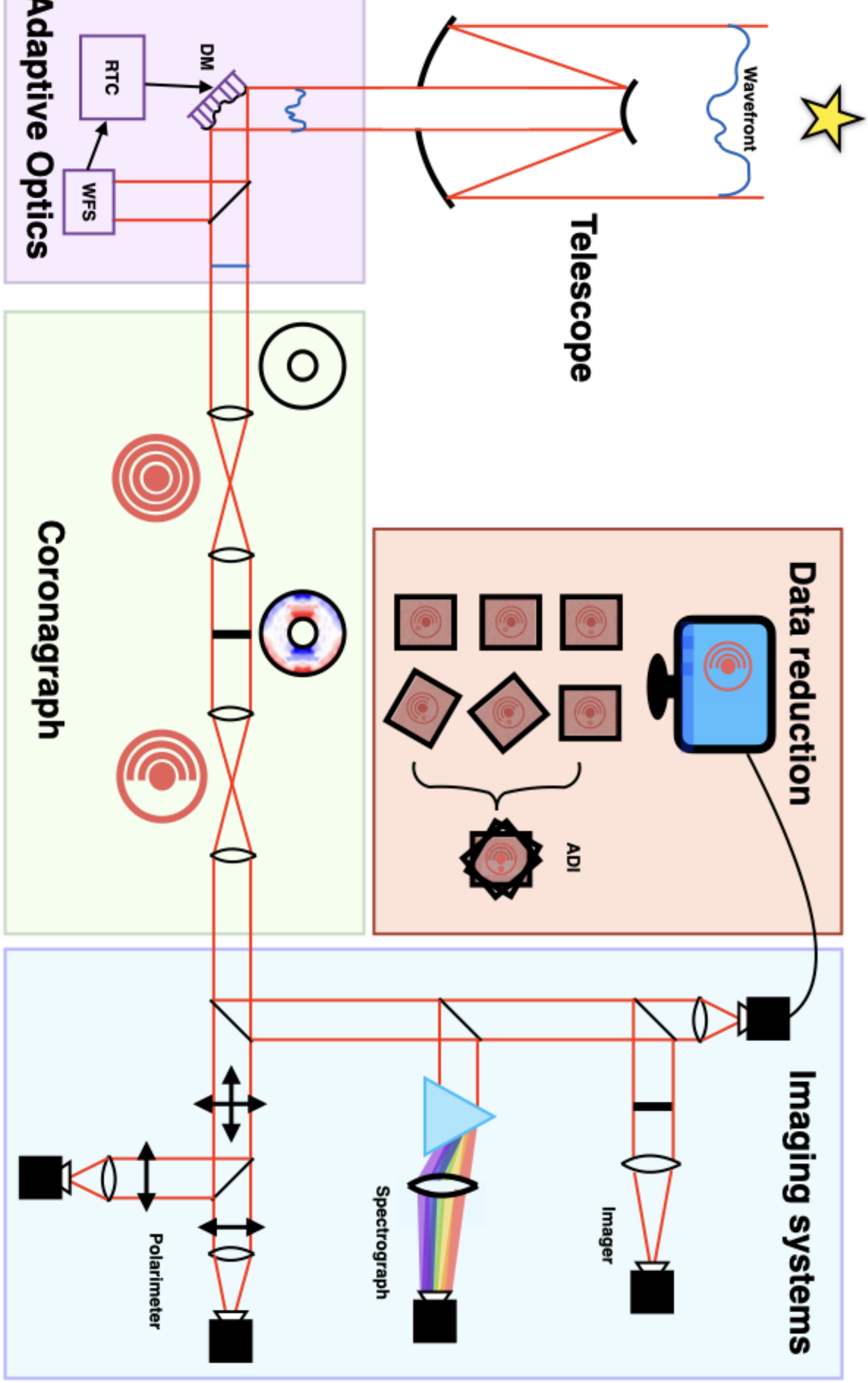

Figure 1.5: Schematic of an HCI system showing the four important components – adaptive optics, coronagraph, imaging systems, and data reduction – of the instrument. Image courtesy of David Doelman.

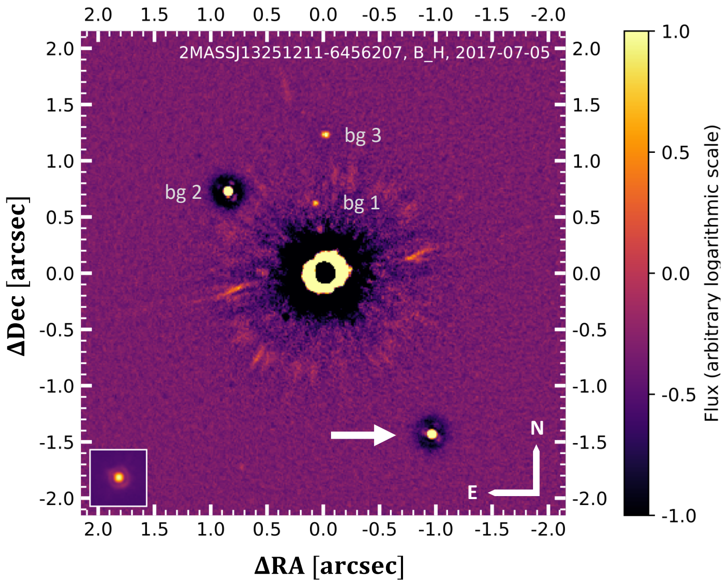

Figure 1.6: Reduced VLT/SPHERE H-band imaging data for TYC8998-760-1. The arrow indicates the far-out co-moving companion while the other objects are background objects (abbrev. bg) as seen by Bohn et al. (2019).

A schematic of an HCI system is shown in Figure 1.5. The extreme adaptive optics (XAO) system (see Section 1.3 for more details) removes aberrations due to atmospheric turbulence and other sources of error, in order to deliver the requisite spatial resolution. The corrected electric-field is relayed through a coronagraph, such as the vector-apodizing phase plate (vAPP) developed by Snik et al. (2012), to suppress the light of the host star over specified spatial frequencies. This creates a dark hole (often a ring) in the focal plane spanning from a prescribed inner working angle (iwa) to an outer working angle (owa). In Figure 1.6 there is a dark area in the centre of psf where the core has been blocked. There is then a halo of light in a butterfly shape (i.e., wind-driven halo, WDH, due to wind blowing turbulent patches across the telescope aperture; see Section 1.3.1) and then the dark ring starting at the iwa suppressing the star light out to the owa. At larger separations, exoplanets are revealed using data reduction techniques, such as angular differential imaging (ADI) developed by Marois, Lafreniere, et al. (2006). ADI relies on diversity introduced into a set of images taken in sequence by field rotation during the observation in order to reduce quasi-static aberrations (slowly changing aberrations). Finally, polarisation, spectroscopy, imaging, and focal plane wavefront sensing all further help to increase the achievable contrast of the system.

HCI challenges

Despite the discovery HCI systems have provided, there are many challenges associated with HCI, preventing the systems from being sensitive to small angular spatial separations (i.e., exoplanets that are either further away or have a small semi-major-axis, a). Currently, technological problems prevent HCI systems from achieving the necessary performance. Two major limiters of HCI systems are the unseen aberrations (by the XAO system) within an instrument's science path (e.g., non-common path aberrations) and the servo-lag error (i.e., the temporal error) Artigau et al. (2018). Removal of non-common path aberrations (NCPA; combination of chromatic errors and alignment and lens aberrations) can be done using focal-plane wavefront sensing techniques. Bos et al. (2019) reports on different methods applied to an HCI system using the vAPP to remove NCPA. **The servo-lag error, however, poses a significant challenge and requires a more in-depth look at the adaptive optics (AO) system.** The servo-lag error manifests itself as the WDH as described by Cantalloube, Por, et al. (2018) and occurs when the turbulence is moving faster than the XAO can handle. Figure 1.7 shows the focal plane with and without the WHD; it clearly shows how the region near the iwa becomes contaminated by speckles. From Cantalloube, Farley, et al. (2020), we know the conditions that cause the WDH at VLT/SPHERE occur $30-40\%$ of the time.

1.3 Adaptive Optics

An AO system provides the spatial resolution required for astronomical imaging with large telescopes. The diffraction limit of a telescope (and estimation of the angular

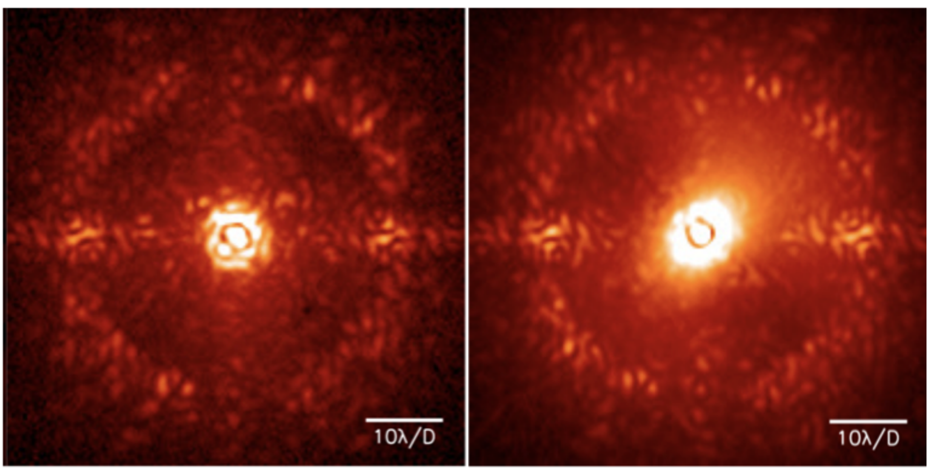

Figure 1.7: Focal plane images without (left) and with (right) the WDH for VLT/SPHERE. Taken from Cantalloube, Farley, et al. (2020).

resolution) is given by $\frac{\lambda}{D}$ with λ being the wavelength and D being the telescope diameter. As the diameter of the telescope gets larger, the resolution is greater. In the presence of turbulence, however, the diffraction limit becomes $\frac{\lambda}{r_0}$ with r_0 being the Fried parameter — the coherence length of turbulence — which has values of 10–15 cm for $\lambda = 500nm$ (Hardy, 1998) and $r_0 \propto \lambda^{\frac{6}{5}}$. Large ground-based telescopes, $D >> r_0$, are severely limited in terms of their angular resolution compared to what they could otherwise achieve if there was no atmosphere. AO corrects for the turbulence in real-time, limiting the impact of the turbulence, and delivering the resolution needed for the science goals of the instrument. An XAO system is an AO system that pushes the diffraction limit as close as possible to the theoretical value.

Figure 1.8 shows the different components of an AO (or XAO) system. The deformable mirror (DM) is a thin mirror (continuous or segmented) with actuators that allow for the shape of the mirror's surface to be deformed. The actuator mechanism can be, among others, voice coil based, or, more popular for XAO, micro-electro-mechanical systems (MEMS) based. The actuator type influences the packing density, the stroke, the linearity, coupling, response time, hysteresis, and creep of the DM; all important factors for the controller and maximum performance. The wavefront sensor (WFS) measures the phase component of the incoming electric-field for a given reference object in the field-of-view: the guide star. The WFS encodes the phase of the incoming wavefront in the flux measured by the WFS camera. Figure 1.8 shows a pyramid WFS which uses a pyramid-shaped optical component to perform a knife-edge test (see Goodwin and Wyant (2006) for details) in two dimensions, creating four images of the pupil plane that encode the local derivatives of the wavefront. From the local derivatives, the phase of the electric-field can be reconstructed (for more information see Kooten et al. (2017)). The WFS often senses in a different wavelength than the science path, using a beam splitter to provide as many photons as possible to both the WFS and the science focal plane to reduce the exposure time needed for a good SNR for both cameras. The real-time-computer (RTC) takes the information from the WFS camera and translates the signal to actuator commands for the DM. An AO system can operate in two different configurations: closed-loop (WFS measures the residual phase) or open-loop (WFS measures the full phase). Closed-loop configuration is most often used.

As mentioned above, an XAO system is the same as a basic AO system but with a larger number of degrees-of-freedom for a given field-of-view. An XAO system needs to deliver a high correction over a small field-of-view using an on-axis target as the guide star. This is done by making use of a high-order DM where the number of actuators is much greater ($> 2\times$) than an AO system for the same D and field-of-view. The XAO system is also required to run much faster, aiming for a WFS frame rate on the order of a couple of kiloHertz (kHz).

AO performance metrics and error terms

The Strehl ratio and variance of the phase are both used to describe the performance of an AO system. *Strehl ratio* (SR) is the ratio of the peak image intensity of the aberrated psf of a point source, compared to the maximum intensity of the idealised

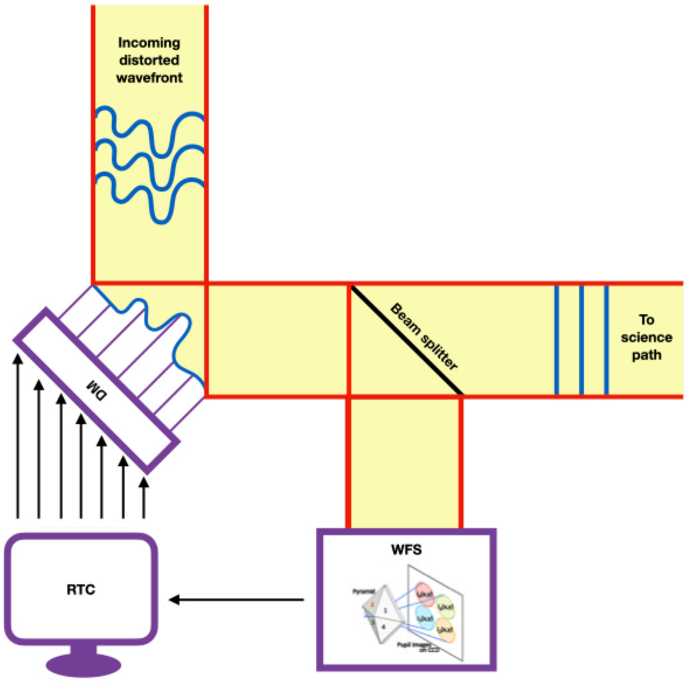

Figure 1.8: Schematic of an AO system in a closed-loop configuration. The incoming distorted phase of the electric-field is corrected by the DM. The corrected light then passes through a beam splitter where some of the light goes to the WFS where the residual wavefront error is sensed. The WFS sends the information to the RTC which calculates the commands to give to the DM.

optical system, which is limited only by the diffraction over the aperture. SR provides a measurement of the image quality and therefore how well an AO system corrects for atmospheric turbulence.

Standard AO systems typically minimise the phase variance of the wavefront instead of the SR. The post-AO phase variance is then a summation of different terms in the AO error budget. Errors from the WFS and DM are the fitting error (spatial under-sampling of the DM), aliasing error (not measuring high spatial frequencies and frequency folding of high spatial frequencies into low spatial frequencies due to WFS sampling), and measurement error (photon noise, read-out noise, etc for WFS). The system also has uncorrected atmospheric errors due to anisoplanatism, scintillation, diffractive effects, and differential refraction (for more information see Hardy, 1998). Finally, the AO system has a *temporal/servo-lag error* due to delays between camera read-out, DM response time, controller bandwidth, and the RTC computation time.

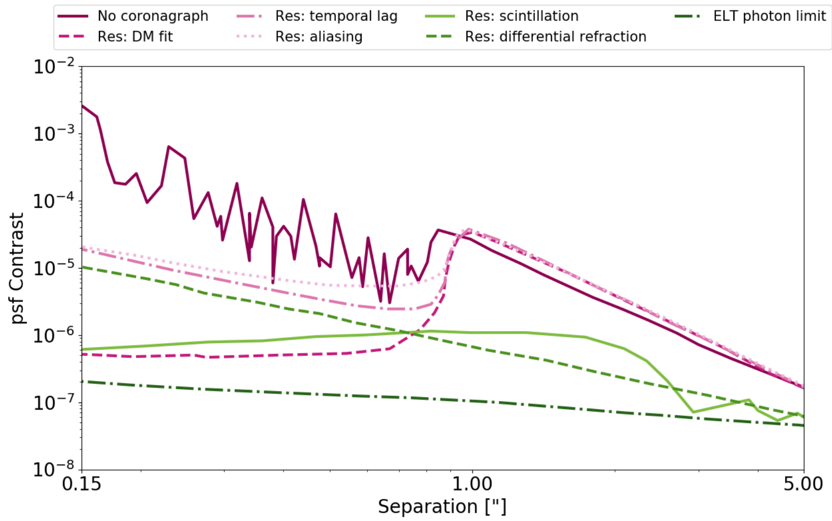

Figure 1.9: Contrast as a function of radial distance from the psf centre showing contributions of common residuals (Res.) in an XAO system based on VLT/SPHERE instrument and for reference the contrast floor for the Extremely Large Telescope (ELT). Differential refraction is a non-common path aberration. Scintillation is from amplitude errors which the XAO cannot correct. Figure taken from Pueyo (2018).

XAO's temporal error problem

Figure 1.9 shows the contribution of different error sources to the contrast as a function of radial separation for the VLT/SPHERE system (Beuzit et al., 2008). For an XAO system, the DM and WFS sampling can be increased to reduce the fitting error and aliasing error. The guide star in an XAO system is the central star (or host star that is being suppressed). The star is often bright enough that the WFS has a good SNR; since the guide star is on-axis, an XAO system does not suffer from anisoplanatism. Finally, the frame-rate of the WFS in many XAO systems is faster than 1 kHz with a delay of 2–4 WFS frames contributing to the temporal error. Note that the assumed operating frequency in Figure 1.9 is 1500 Hz – VLT/SPHERE runs at 1380 Hz and therefore the effect of the temporal error is underestimated. All of this results in the temporal error being a large source of error in an HCI system, limiting the contrast. In the following sections, we will further introduce the temporal error and its effect on an (X)AO system, including how the effect of the delay can be mitigated. **Mitigating the effect of the temporal delay is the main focus of this dissertation.**

1.3.1 AO Control and Disturbance rejection

Many AO control systems make use of very simple, but effective, control methods. Figure 1.10 is a block diagram of an AO system in a closed-loop configuration. This setup uses feedback to drive the system to the desired state. Note that an AO system

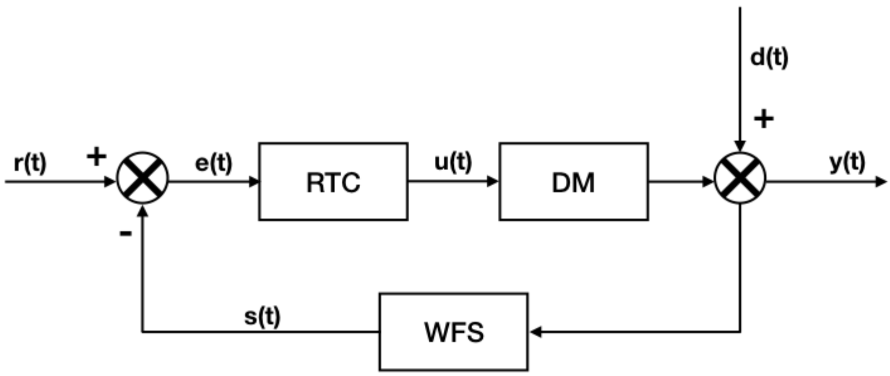

Figure 1.10: Block diagram of an AO system in closed-loop configuration. It shows the system plant as the DM, the WFS measures and feeds the RTC which calculates the control commands for the DM.

is a multi-input-multi-output system. In Figure 1.10 the system is provided a reference point ($r(t)$; either a flat wavefront or an offset to correct for NCPA). The RTC receives an error signal, $e(t)$, that informs the control law how far a recent correction was from $r(t)$. The RTC then calculates the updated commands, $u(t)$, according to the controller and sends these to the DM. The DM applies the correction, rejecting $d(t)$ (the input disturbance), and producing a corrected wavefront—$y(t)$—which is seen by the science camera and the WFS, allowing it to measure the residual input disturbance. Input disturbances are external processes that drive the system away from the desired state. In an AO system the input disturbance is a combination of atmospheric turbulence, telescope vibrations, and noise that introduce phase aberrations into the system. In this work we focus on atmospheric turbulence being the sole input disturbance.

$$u(t) = g \int_0^t e(\tau) d\tau \tag{1.1}$$

The control law used by many AO systems in closed-loop operation is an integral control law (integrator). An integrator action says that $u(t)$ is proportional to the integral of the error (in a discrete system: the sum of all previous errors) as given in Equation 1.1. The integral controller is sensitive to the magnitude and duration of the error. The gain, g, is chosen such that control bandwidth—how fast the system responds to the changing $e(t)$—is as high as possible while maintaining the stability of the system. In the case of an AO system, a g value close to unity is ideal for disturbance rejection when the plant dynamics are negligible. When the plant dynamics cannot be ignored, as in the case for a real-life AO system, g must be reduced in order to keep the system stable. Since the power spectral density (PSD) of turbulence is dominated by the low frequency components (see Section 1.3.1) and the integral controller has a high loop gain over this frequency range, reasonable performance is achieved for most conditions. An integrator properly tuned will therefore result in sustainable disturbance rejection and good correction for the system resulting in SR$= 30-50\%$ for regular AO systems or SR $> 90\%$ for XAO systems. The benefit of such a control law is that it performs reasonably well for an AO system subject to many different conditions with minimal or coarse tuning of the gain parameter. The integral controller does not, however, provide optimal control or guarantee control stability. For more in-depth background information on control for AO systems can be found in Roddier (1981) and Hardy (1998).

Describing Optical Aberrations

Ultimately, an AO controller aims to minimise the phase variance directly or indirectly. However, different formulations can be used to describe the aberrations seen by the system and change the mathematical representation of the system and controller. Within an AO system the aberrations can be described as by a zonal or modal basis. In the zonal representation, each actuator of the DM is controlled separately by the WFS signal conjugate to that by the area (zone) of the DM. For a modal representation, the aberrations are expressed as a linear combination of a spatial basis set (spanning the pupil) that best fit the WFS data. In AO, Zernike modes are often used to describe wavefront errors and are easy to understand from a user perspective (Noll, 1976). Furthermore, they are orthogonal over a circular aperture.

In the above discussion on control, we have made some important assumptions about the AO system including that the system is linear, continuous, and free of temporal delays. We, however, have also stated that the system does indeed have delays resulting in the servo-lag error (Hardy, 1998). In Figure 1.10, we can add a delay of Δt time steps such that the DM shape is a result of $u(t-\Delta t)$. The delay has an important effect for the system as the input disturbance (i.e., atmospheric turbulence) is not static but varies in time.

Atmospheric turbulence

The atmosphere can be thought of as a finite number of parallel layers of air that behave differently to one another (i.e., each with different wind speed and direction). Turbulence is caused by convection and/or shearing between the different layers. To completely understand the behaviour of turbulence the Navier-Stokes equations must be solved for the appropriate boundary conditions. In AO, however, a simplified approach is used to understand the statistical behaviour of optical turbulence.

Kolmogorov (1941) postulated that flows with high Reynolds numbers (i.e., those in which turbulence is dominant) are statistically isotropic and that the small (inner) scale of the energy cascade (the transfer of energy from large scales of motion to small scales of motion) is universal and uniquely determined by the kinematic viscosity and rate of energy dissipation. By knowing the large (outer) scale of the energy cascade, one could determine the spatial statistical behaviour of the turbulence between the inner and outer scales (the so-called inertial range). The idea is further

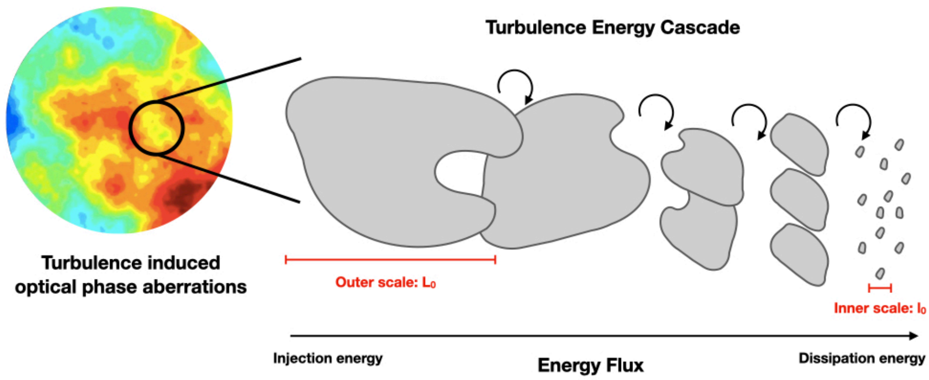

Figure 1.11: The turbulence energy cascade described by Kolmogorov (1941). In a turbulent flow energy is injected at the largest spatial scale (L_0) and cascades down into smaller and smaller scales until it dissipates at the smallest spatial scale, l_0. The spatial scales between these two limits are the main contributors to the optical phase aberrations seen above a telescope.

illustrated in Figure 1.11. Comparison of Kolmogorov's theory to experimental values has led to Kolmogorov's PSD. Currently, the von Kárman phase PSD (a modified Kolmogorov PSD) can be used to explain the spatial properties of observed optical turbulence, see Azoulay et al. (1988).

The modified von Kárman spatial PSD describing phase fluctuations due to atmosphere turbulence integrated for all heights is given by:

$$\Phi(k) = \frac{0.023}{r_0^{5/3}(k^2 + k_0^2)^{11/6}} e^{\frac{-k^2}{k_m^2}}$$
$$k_m = \frac{5.92}{l_0}$$
$$k_0 = \frac{2\pi}{L_0}$$

with l_0 and L_0 as the inner and outer scales in meters, respectively. With this equation, the spatial behavior of the phase can be determined by l_0, L_0, and r_0.

To further simplify the problem, the temporal behaviour of turbulence can be assumed to be the result of wind alone. According to Taylor's Frozen Flow hypothesis (Taylor, 1938), turbulent patches remain constant and are simply blown horizontally by the wind. In the case of a telescope aperture, temporal variations in turbulence at a given location are due to spatial variations being moved in time. Using this idea an expression of the temporal PSD is derived by Harrington and Welsh (1994), assuming the von Kárman spatial PSD. Assuming the inhomogeneities of the atmosphere remain fixed as it moves with a specific wind velocity (i.e., Frozen Flow), v, the single-sided and single-layer temporal PSD as a function of frequency, f, is given by:

$$W(f) = 0.033 C_n^2 \bar{k}^2 h v^{5/3} (f^2 + \frac{k_0^2 v^2}{4\pi^2})^{-4/3}$$

with h being the optical path length through the turbulence (e.g., for on-axis it would be the height of the layer), C_n^2 encoding the turbulence strength at that height, $\bar{k} = \frac{2\pi}{\lambda}$, and ignoring l_0. By integrating over all heights we can find a temporal PSD for the full turbulence above the telescope using $r_0 \propto (\int_0^\infty C_n^2(h)dh)^{-3/5}$

Non-stationary turbulence

The simplified description of optical phase variations due to atmospheric turbulence presented above assumes that the optical phase due to turbulence is a statistically stationary process (meaning the mean and variance do not change in time). While this assumption may be true over certain timescales or even at certain telescope locations, in reality atmospheric turbulence is a non-stationary process (Tokovinin and Travouillon, 2006) where the rate at which the mean and variance change is unknown and might differ throughout a night or from night to night. Using the above framework, a simple way of understanding what might be happening in real life is to imagine that the parameters of the von Kárman PSD vary in time. When this occurs, the optical phase fluctuations have non-stationary behaviour. Figure 1.12 illustrates

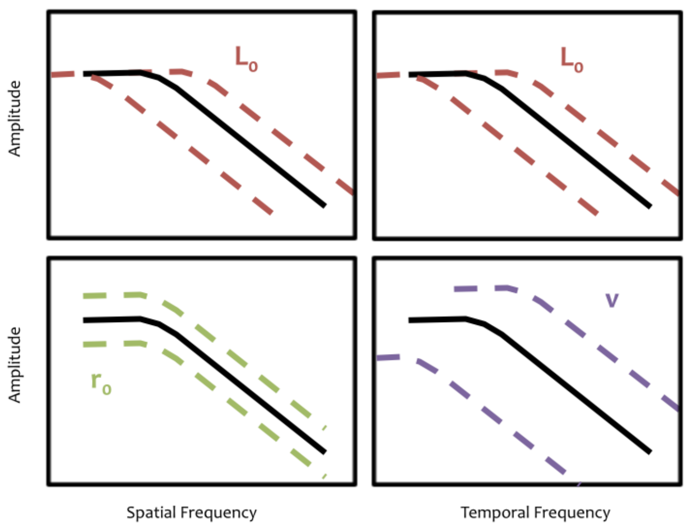

Figure 1.12: Sketch of the von Kárman PSD for spatial and temporal frequencies. The black line is a reference PSD while the dashed lines show how the PSD changes for the indicated parameters. The outer scale varies both the spatial and temporal PSD while the Fried parameter affects the spatial PSD and the wind speed affects the temporal PSD.

the effects v, r_0, and L_0 have on both the spatial and temporal PSDs. From a controller perspective, the changes in the temporal cut-off frequency are most important and this occurs when either v or L_0 change in time. L_0 also changes the spatial cut-off frequency. r_0 changes only the gain (amplitude) of the spatial PSD. The first step to understanding the impact of non-stationary turbulence on an XAO system is to determine how to model it and see the effects it has in simulation. Currently, the non-stationarity aspect of turbulence is observed through changes of the C_n^2 profile (integrating these profiles over all heights gives r_0) throughout a night as shown in Figure 1.13. These profiles, however, are estimated over a couple of minutes limiting the accuracy for which we can understand what the atmosphere is doing on shorter timescales as explained by Tokovinin and Kornilov (2007). In this dissertation we answer the question **how can we model non-stationary atmospheric turbulence phase fluctuations?**

Disturbance and the Servo-lag Error

In an HCI system one tangible manifestation of the servo-lag error is the WDH that appears as a butterfly pattern in the coronagraphic/science image (Cantalloube, Por, et al., 2018), see Figure 1.7. The WDH provides a visual example of how the servo-lag error limits the contrast at small angular separations. The WDH is the focal plane representation of the temporal error that is defined in the pupil plane. The impact of the error on the focal plane is directly related to the behavior of the turbulence. If the turbulence is evolving slower than the lag in the control system, the servo-lag has minimal impact and vice-versa. In other words, if the turbulence coherence time ($\tau = 0.314 r_0/v$) is shorter or close to the XAO lag time, the WDH appears in the

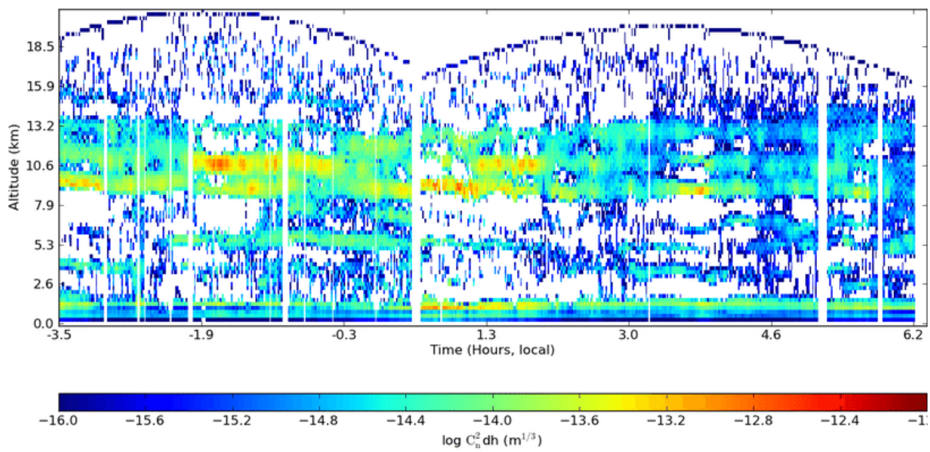

Figure 1.13: C_n^2 profiles taken by the Stereo-SCIDAR instrument on the Isaac Newton Telescope. The data, taken starting the night of 17 September 2014, shows a turbulent layer around 1 km and 3 separate layers between 9 and 13 km that all vary in strength throughout the night. Figure taken from Morris et al. (2014).

focal plane. The relation between τ, r_0, and therefore λ is one reason why AO is easier for longer wavelengths.

While an AO system minimises the phase variance, the metric that matters for an HCI system is the raw contrast. Even though the servo-lag error is relatively small and can be ignored for regular AO systems, it has a large impact on XAO systems as seen for observations (see Figure 1.7) and must therefore be addressed. One area of ongoing research is to verify how the non-corrected atmospheric turbulence affects the raw contrast and if it agrees theoretical expectations (e.g., Guyon, 2005; Cantalloube, Por, et al., 2018). This varies with a number of assumptions about the system especially the turbulence model as well as the controller behaviour. This leads to an important question, **how much contrast is lost by assuming stationary turbulence in the controller design when the turbulent conditions are in fact non-stationary?**

To improve the contrast at small angular separations, one can focus directly on minimising the effects of the servo-lag error. One simple solution is to minimise the delay in the XAO itself by running everything faster. However, hardware limits the maximum attainable speed of the DM. Further, by running the XAO faster, the system can become photon starved, even for bright targets. An alternative solution is to upgrade the XAO control system by implementing a new control algorithm. **One type of control algorithm that has been investigated in recent years is predictive control, which aims to predict the evolution of the atmosphere during the time between measurement and correction. This approach directly targets the servo-lag error and is a topic of this dissertation.**

Prediction and Control

During the time delay, the atmospheric turbulence evolves; resulting in a residual phase variance due to the difference in the current and measured wavefront phase. The first mention of prediction in AO literature was made by (Hardy, 1998). The idea of the traveling wave predictor was based on Frozen Flow and would compensate for the longer delays seen in initial AO systems. Since then, prediction has been implemented as a by-product of work in optimal control for various AO systems where the necessary SR is much lower than that required in XAO and the servo-lag error is not the dominant error term in the system. Since then, data-driven techniques have been investigated for the purpose of prediction for XAO systems.

Optimal Control One can determine the optimal control law for a dynamical system described by a set of equations. The control problem is defined by a cost function that is a function of the states (e.g., measured zonal modes that describe the phase distortion) and control variables (e.g., DM actuators' values) of the system. The control law is then determined by minimising a chosen cost function. Different cost functions result in different optimal control laws. Some of the important work done using the optimal control framework is highlighted below.

The linear-quadratic regulator (LQR) is a controller that minimises a quadratic cost function for a linear system with feedback. When the system is subject to Gaussian noise, the feedback control law becomes the linear-quadratic-Gaussian (LQG) controller making use of the Kalman filter. One challenge of LQG control is that it requires an accurate model of the plant (DM and WFS) as well as the input disturbance (turbulence). In a series of papers (see Looze (2006), Looze (2008), and Looze (2009)) the LQG controller is studied for AO systems. Many different assumptions have been explored in modelling the plant, ranging from ignoring the DM dynamics to full modelling of the DM based on laboratory measurements. For the input disturbance, LQG can do a good job rejecting telescope vibrations that are easy to accurately model (Sivo et al., 2014). However, extending the model to reject atmospheric turbulence has proven more difficult. The main trouble arises from estimating a model for atmospheric turbulence in a finite (manageable size) state-based representation that accurately represents the turbulence. As such, in the literature an auto-regressive model of order one is often used to describe atmospheric turbulence with an understanding that it can be expanded to include higher order terms if necessary (Le Roux et al., 2004). In theory, once the temporal effects are included in the controller, the Kalman filter using this atmospheric model performs prediction at each time step. To date there has been limited success on-sky using the LQG controller for full atmospheric turbulence rejection. It is also important to note that LQG optimality does not automatically ensure good robustness. The robust stability of the closed-loop system must be checked separately after the LQG controller has been designed; this requires substantial on-sky testing for verification.

By making slight changes to the cost function of the LQG controller one can form the H2 optimal controller. On-sky tests by Doelman et al. (2011) show a reduction in the temporal error for tip-tilt control. In designing this controller two different approaches for modelling the atmospheric disturbance were explored by Hinnen et al. (2007). First, using a theoretical turbulence spectrum and, second, using the open-loop WFS data (WFS directly measures the full turbulence as it is placed before the DM) to determine the disturbance. The work demonstrates the importance of proper modelling of the atmospheric disturbance to have an accurate enough model for optimal control to perform well. Once again due to the model of the system having a temporal delay, the optimal control law, by design, performs prediction as part of the control law.

Linear Data-Driven Prediction for XAO Current work on linear prediction in XAO primarily focuses on the prediction of atmospheric turbulence as a step before the controller. Therefore, the control law is unaware of the existence or influence of the prediction step. Specifically, the prediction algorithms are chosen to be data-driven, and learn online as modelling the atmosphere's behaviour to the accuracy needed for XAO systems has proven to be difficult if not impossible.

The prediction is performed by estimating the pseudo-open loop phase (full turbulence phase calculated from knowing the WFS values and the DM shape; instead of phase can use slopes, or modes instead) and applying a predictive filter before the control algorithm. This approach allows for a system architecture that can turn prediction on and off with minimal effect on the control loop. Furthermore, one can test the predictability of turbulence and not focus on the behaviour of the control loop itself. A similar structure has been implemented using the CACAO RTC (Guyon, Sevin, et al. (2018)). Empirical orthogonal functions (EOF) is a data-driven predictor that minimises the phase variance. Implemented on SCExAO (an HCI instrument at the Subaru telescope in Hawaii), Guyon, Sevin, et al. (2018) have demonstrated that EOF improves the standard deviation of the psf over a set of images. However, the improvement is less than expected from initial simulations by Guyon and Males (2017). Prediction might also perform differently at other observing sites where the turbulence behaves differently. This leads me to ask **how does prediction perform for the VLT/SPHERE in Paranal?**

Similar methods to EOF minimise the same cost function as EOF but with a different evaluation of the necessary covariance functions, including the prediction done in this work. A posteriori tests by Jensen-Clem et al. (2019), using AO telemetry, show an average factor of 2.6 improvement for contrast for separations from 0 to $10\lambda/D$. All these tests have shown that improvement expected from prediction is not seen in reality. We therefore ask the following questions: **what improvement is expected from prediction when assuming non-stationary turbulence, and how does linear data-driven prediction behave under different input disturbances?**

1.4 In this Dissertation

In the above sections, we introduce and motivate the 6 main questions addressed in this dissertation:

1. What type of astronomical objects could be the cause of these brightening events in the Kepler database?
2. How can we model non-stationary atmospheric turbulence phase fluctuations?
3. Given that turbulence is non-stationary, how much contrast is lost by assuming stationary turbulence in the controller design?
4. How does linear data-driven prediction behave under different input disturbances?
5. What improvement is expected from prediction when assuming non-stationary turbulence?
6. How does prediction perform for the VLT/SPHERE in Paranal?

In Chapter 2 of this dissertation, we take a closer look at Q1. We investigate two possible mechanisms to explain the observed light curves, namely: forward scattering from an optically thin dust cloud, and tidal interactions from a close binary star system.

The subsequent chapters transition to focus on HCI and control: from improving atmospheric turbulence modelling, seeing the effects of this on contrast and linear prediction, and finally studying how prediction performs with real atmospheric optical phase aberrations. Chapter 3 introduces a linear data-driven predictor and assumes simple cases of non-stationary turbulence (such as wind gusts and varying

r_0 based off similar data shown in Figure 1.13) to show that changes to the disturbance model can have a large effect on prediction, thereby briefly looking at Q2 and Q4. These results lead to the work presented in Chapter 4. In this chapter we form a more realistic non-stationary model of atmospheric turbulence using Thirty Meter Telescope (TMT) site testing data to form a wind model allowing for the modelling of non-stationary turbulence, addressing Q2. Using this model, we study how much contrast is lost for an ideal integrator, assuming either constant wind or varying wind speed, in order to address Q3. To investigate Q4, we utilise the non-stationary model of atmospheric-turbulence-induced phase, and apply a linear data-driven predictor in Chapter 5. We then quantify the improvement expected, answering Q5. In Chapter 6, we verify the answer to Q5, and answer Q6, while studying prediction on VLT/SPHERE testing prediction under 27 different atmospheric conditions.

In summary, the main conclusions of this dissertation are:

- **For the 8 WOI identified in the Kepler data both forward scattering and highly elliptical binary star system models can explain the observed brightening in the light curves.**
- **Under time varying turbulence due to changing wind speed, an XAO loses performance.** For a standard integral controller, sub-second wind speed fluctuations affect contrast by less than 5%, however, wind speed changes on longer timescales led to a much larger loss in contrast than predicted by the fundamental limitations. An XAO system needs to track the wind speed at rates faster than 2 minutes for the given wind statistics on Mauna Kea. A linear data-driven predictor will also lose performance due to the inability to track the varying statistics compared to the optimal implementation of the same predictor with infinite tracking capabilities.
- **For VLT/SPHERE, a linear data-driven predictor results in an improvement of performance.** For the 27 various observing conditions studied, the XAO correction is more reliable and consistent. The optical turbulence as seen by VLT/SPHERE is also time-invariant. Therefore, the temporal regressors of the predictor have a larger impact on the performance than the spatial regressors. A batch temporal-only predictor for the VLT/SPHERE is therefore recommended to reduce the servo-lag error.

1.5 Outlook

With the end of the Kepler mission and the start of the TESS era in precision photometry, more and more light curves are being obtained for a fast portion of the sky. In the last few years, new methods have also been employed for searching through databases looking for new signals and outliers. It is important to look at these objects and model the physics behind them, as done in this dissertation. These signals could indeed be an exoplanet/proto-planetary disk system in configurations previously not detected, thereby providing new insights. Finally, for the objects in Chapter 2 follow-up observations will be necessary to fully understand what is truly occurring to create the observed Kepler light curves and distinguish which model is responsible for the increase in flux.

As HCI systems are being built for the next generation of large telescopes it is necessary to fully understand the relation between atmospheric turbulence, predictive control, and contrast. To do this, it is essential for the community to first understand the main differences in the performance of linear prediction at Hawaii, Paranal, and other observatory locations. This requires a good understanding of the telescope, instrument and the full implementation of the controller, as well as the atmosphere above the telescope. At specific sites, different predictive control schemes might be better suited for a given site or telescope due to the input disturbances. More specifically, we find in Chapter 5 that how well the predictor performs is related to L_0 and the telescope diameter. Especially for the extremely large telescopes, it is important to truly know what possible values for L_0 are and how it evolves in time. Furthermore, in Chapter 6 we find evidence that input disturbances other than atmospheric turbulence (e.g., telescope vibrations) might have a large effect on the controller and therefore final contrast; this is different from originally thought and must be considered for future HCI systems. Finally, the final raw contrast is the critical performance index for HCI. Investigating the effects of prediction on contrast for different types of coronagraphs, and determining whether predictive control can be used to directly optimise the raw contrast (either over a part of the field-of-view or the entire focal plane) is an interesting research direction.

Another crucial step for AO control, especially XAO control, is to have flexible instruments and telescope facilities to allow for the testing of new control schemes to further develop them and provide the required performance. Being able to test controllers in real-life situations under a variety of conditions is invaluable. With access to these types of testing, different control schemes can more readily be explored such as data-driven optimal control or model predictive control. By looking into the topics outlined above, the control community can provide the best performance for HCI systems such that the contrast at smaller angular resolutions will allow for the imaging, and subsequent characterisation, for far away and close-in exoplanets.

References

Advanced School on Exoplanetary Science (1st : 2015 : Vietri sul Mare, Italy), Valerio Bozza, Luigi (Research scientist) Mancini, and Alessandro Sozzetti (2016). "Methods of detecting exoplanets : 1st Advanced School on Exoplanetary Science". In:

Ahlers, John P. et al. (Jan. 2020). "Gravity-darkening Analysis of the Misaligned Hot Jupiter MASCARA-4 b". In: *The Astrophysical Journal* 888.2, p. 63.

Artigau, Etienne et al. (Aug. 2018). "Direct Imaging in Reflected Light: Characterization of Older, Temperate Exoplanets With 30-m Telescopes". In: *arXiv e-prints*, arXiv:1808.09632.

Avenhaus, Henning et al. (Aug. 2018). "Disks around T Tauri Stars with SPHERE (DARTTS-S). I. SPHERE/IRDIS Polarimetric Imaging of Eight Prominent T Tauri Disks". In: *The Astrophysical Journal* 863.1, p. 44.

Azoulay, E, V Thiermann, A Jetter, A Kohnle, and Z Azar (Oct. 1988). “Optical measurement of the inner scale of turbulence”. In: *Journal of Physics D: Applied Physics* 21.10S, S41–S44.

Beuzit, J.-L. et al. (July 2008). “SPHERE: a ’Planet Finder’ instrument for the VLT”. In: *Proc.SPIE* 7014, p. 701418.

Bohn, A J et al. (Dec. 2019). “The Young Suns Exoplanet Survey: Detection of a wide-orbit planetary-mass companion to a solar-type Sco-Cen member”. In: *Monthly Notices of the Royal Astronomical Society* 492.1, pp. 431–443.

Borucki, William J. et al. (2010). “Kepler Planet-Detection Mission: Introduction and First Results”. In: *Science* 327.5968, pp. 977–980.

Bos, S. P., D. S. Doelman, J. Lozi, O. Guyon, C. U. Keller, K. L. Miller, N. Jovanovic, F. Martinache, and F. Snik (Nov. 2019). “Focal-plane wavefront sensing with the vector-Apodizing Phase Plate”. In: *Astronomy & Astrophysics* 632, A48.

Campbell, Bruce, G. A. H. Walker, and S. Yang (Aug. 1988). “A Search for Substellar Companions to Solar-type Stars”. In: *The Astrophysical Journal* 331, p. 902.

Cantalloube, F., E. H. Por, et al. (2018). “Origin of the asymmetry of the wind driven halo observed in high-contrast images”. In: *Astronomy & Astrophysics* 620, p. L10.

Cantalloube, Faustine, Ollie Farley, et al. (2020). *The wind-driven halo in high-contrast images I: analysis from the focal plane images of SPHERE*.

Charbonneau, D., T. M. Brown, D.W. Latham, and M. Mayor (Jan. 2000). “Detection of Planetary Transits Across a Sun-like Star”. In: *The Astrophysical Journall* 529.1, pp. L45–L48.

Charbonneau, D., T. M. Brown, R. W. Noyes, and R. L. Gilliland (Mar. 2002). “Detection of an Extrasolar Planet Atmosphere”. In: *The Astrophysical Journal* 568.1, pp. 377–384.

Doelman, N., R. Fraanje, and R. den Breeje (2011). “Real-sky adaptive optics experiments on optimal control of tip-tilt modes”. In: *2nd Conference on Adaptive Optics for Extremely Large Telescopes* 1.1.

Dorval, P. et al. (Mar. 2020). “MASCARA-4 b/bRing-1 b: A retrograde hot Jupiter around a bright A-type star”. In: *Astronomy & Astrophysics* 635, A60.

Goodwin, E.P. and J.C. Wyant (2006). *Field Guide to Interferometric Optical Testing*. Field Guide Series. SPIE.

Guyon, O. and J. Males (July 2017). “Adaptive Optics Predictive Control with Empirical Orthogonal Functions (EOFs)”. In: *ArXiv e-prints*.

Guyon, Olivier (Aug. 2005). “Limits of Adaptive Optics for High-Contrast Imaging”. In: *The Astrophysical Journal* 629.1, pp. 592–614.

Guyon, Olivier, Arnaud Sevin, et al. (2018). “The compute and control for adaptive optics (CACAO) real-time control software package”. In: *Adaptive Optics Systems VI*. Ed. by Laird M. Close, Laura Schreiber, and Dirk Schmidt. Vol. 10703. International Society for Optics and Photonics. SPIE, pp. 469–480.

Hardy, J. W. (1998). “Adaptive Optics for Astronomical Telescopes”. In: *Oxford University Press Jul 1998*.

Harrington, Patrick M. and Byron M. Welsh (1994). “Frequency-domain analysis of an adaptive optical system’s temporal response”. In: *Optical Engineering* 33.7, pp. 2336–2342.

Hatzes, Artie P., William D. Cochran, Michael Endl, Barbara McArthur, Diane B. Paulson, Gordon A. H. Walker, Bruce Campbell, and Stephenson Yang (Dec. 2003). "A Planetary Companion to γ Cephei A". In: *The Astrophysical Journal* 599.2, pp. 1383–1394.

Hinnen, Karel, Michel Verhaegen, and Niek Doelman (June 2007). "Exploiting the spatiotemporal correlation in adaptive optics using data-driven H2-optimal control". In: *J. Opt. Soc. Am. A* 24.6, pp. 1714–1725.

Jensen-Clem, Rebecca, Charlotte Z. Bond, Sylvain Cetre, Eden McEwen, Peter Wizinowich, Sam Ragland, Dimitri Mawet, and James Graham (2019). "Demonstrating predictive wavefront control with the Keck II near-infrared pyramid wavefront sensor". In: *Techniques and Instrumentation for Detection of Exoplanets IX*. Ed. by Stuart B. Shaklan. Vol. 11117. International Society for Optics and Photonics. SPIE, pp. 275–284.

Kolmogorov, A. (Jan. 1941). "The Local Structure of Turbulence in Incompressible Viscous Fluid for Very Large Reynolds' Numbers". In: *Akademiia Nauk SSSR Doklady* 30, pp. 301–305.

Kooten, Maaike van, Jean Pierre Veran, and Colin Bradley (2017). "Alternative pyramid wavefront sensors". In: *Journal of Astronomical Telescopes, Instruments, and Systems* 3.2, p. 029001.

Le Roux, B., R. Ragazzoni, C. Arcidiacono, J.-M. Conan, C. Kulcsar, and H.-F. Raynaud (Oct. 2004). "Kalman-filter-based optimal control law for star-oriented and layer-oriented multiconjugate adaptive optics". In: *Proc.SPIE* 5490, pp. 1336–1346.

Lesage, A.-L., J. F. P. Spronck, R. Stuik, F. Bettonvil, D. Pollaco, and I. A. G. Snellen (2014). "MASCARA: the multi-site all-sky CAameRA: concept and first results". In: *Ground-based and Airborne Telescopes V*. Ed. by Larry M. Stepp, Roberto Gilmozzi, and Helen J. Hall. Vol. 9145. International Society for Optics and Photonics. SPIE, pp. 402–409.

Looze, D. P. (July 2008). "Structure of a hybrid signal LQG controller for adaptive optics". In: *Adaptive Optics Systems*. Vol. 7015. Proceedings SPIE, p. 701536.

Looze, Douglas P. (Mar. 2006). "Minimum variance control structure for adaptive optics systems". In: *J. Opt. Soc. Am. A* 23.3, pp. 603–612.

— (Jan. 2009). "Linear-quadratic-Gaussian control for adaptive optics systems using a hybrid model". In: *J. Opt. Soc. Am. A* 26.1, pp. 1–9.

Marois, C., D. Lafreniere, R. Doyon, B. Macintosh, and D. Nadeau (Apr. 2006). "Angular Differential Imaging: A Powerful High-Contrast Imaging Technique". In: *The Astrophysical Journal* 641.1, pp. 556–564.

Marois, C., B. Macintosh, T. Barman, B. Zuckerman, I. Song, J. Patience, D. Lafreniere, and R. Doyon (2008). "Direct Imaging of Multiple Planets Orbiting the Star HR 8799". In: 322.5906, pp. 1348–1352.

Mayor, M., S. Udry, D. Naef, F. Pepe, D. Queloz, N. C. Santos, and Burnet, M. (2004). "The CORALIE survey for southern extra-solar planets*** - XII. Orbital solutions for 16 extra-solar planets discovered with CORALIE". In: *Astronomy & Astrophysics* 415.1, pp. 391–402.

Mayor, Michel and Didier Queloz (1995). "A Jupiter-mass companion to a solar-type star". In: *Nature* 378.6555, pp. 355–359.

Morris, Tim et al. (July 2014). “CANARY phase B: on-sky open-loop tomographic LGS AO results”. In: vol. 9148, p. 91481I. DOI: 10.1117/12.2056279.
Noll, Robert J. (Mar. 1976). “Zernike polynomials and atmospheric turbulence∗”. In: *J. Opt. Soc. Am.* 66.3, pp. 207–211.
Pueyo, Laurent (2018). “Direct Imaging as a Detection Technique for Exoplanets”. In: p. 10.
Ricker, George R. et al. (Jan. 2015). “Transiting Exoplanet Survey Satellite (TESS)”. In: *Journal of Astronomical Telescopes, Instruments, and Systems* 1, p. 014003.
Roddier, F. (Jan. 1981). “The effects of atmospheric turbulence in optical astronomy”. In: *Progess in Optics* 19, pp. 281–376.
Sissa, E. et al. (2018). “New disk discovered with VLT/SPHERE around the M star GSC 07396-00759”. In: *Astronomy & Astrophysics* 613, p. L6.
Sivo, Gaetano et al. (Sept. 2014). “First on-sky SCAO validation of full LQG control with vibration mitigation on the CANARY pathfinder”. In: *Opt. Express* 22.19, pp. 23565–23591.
Snellen, Ignas A. G., Remco J. de Kok, Ernst J. W. de Mooij, and Simon Albrecht (June 2010). “The orbital motion, absolute mass and high-altitude winds of exoplanet HD209458b”. In: *Nature* 465.7301, pp. 1049–1051.
Snik, Frans, Gilles Otten, Matthew Kenworthy, Matthew Miskiewicz, Michael Escuti, Christopher Packham, and Johanan Codona (Sept. 2012). “The vector-APP: a broadband apodizing phase plate that yields complementary PSFs”. In: *Modern Technologies in Space- and Ground-based Telescopes and Instrumentation II*.
Taylor, Geoffrey Ingram (1938). “Production and dissipation of vorticity in a turbulent fluid”. In: *Proceedings of the Royal Society of London. Series A - Mathematical and Physical Sciences* 164.916, pp. 15–23.
Tokovinin, A. and V. Kornilov (Oct. 2007). “Accurate seeing measurements with MASS and DIMM”. In: *Monthly Notices of the Royal Astronomical Society* 381.3, pp. 1179–1189.
Tokovinin, A. and T. Travouillon (Feb. 2006). “Model of optical turbulence profile at Cerro Pachón”. In: *Monthly Notices of the RAS* 365.4, pp. 1235–1242.
Wheeler, Adam and David Kipping (Mar. 2019). “The weird detector: flagging periodic, coherent signals of arbitrary shape in time-series photometry”. In: *Monthly Notices of the Royal Astronomical Society* 485.4, pp. 5498–5510.
Wolszczan, A. and D. A. Frail (1992). “A planetary system around the millisecond pulsar PSR1257 + 12”. In: *Nature* 355.6356, pp. 145–147.
Zurlo, A. et al. (2016). “First light of the VLT planet finder SPHERE - III. New spectrophotometry and astrometry of the HR9 exoplanetary system”. In: *Astronomy & Astrophysics* 587, A57.

Chapter 2

Brightening of Kepler light curves: from binary star systems to forward scattering dust clouds

"There is nothing like looking, if you want to find something. You certainly usually find something, if you look, but it is not always quite the something you were after ".

J.R.R. Tolkien, *The Hobbit*

Summary

Dedicated transiting surveys, such as the Kepler space telescope, have provided the astronomy community with a rich data set resulting in many new discoveries. The data from such surveys have captured many astrophysical processes that alter the flux from an emitting body. In this paper we look at eight objects of interest identified by Wheeler and Kipping (2019) with a periodic, broad increase in flux, that look distinctly different from intrinsic star variability. We consider two physical phenomena as explanations for these observed Kepler light curves; the first being the classical explanation while the second being an alternative scenario: 1. tidal interactions in a binary star system, and 2. forward scattering from an optically thin cloud with an exoplanet. We investigate the likelihood of each model by modelling and fitting to the observed data. The heartbeat system qualitatively does a good job of reproducing the shape of the observed light curves due to the tidal interaction of the two stars. We do, however, see a mismatch in flux right before or after the peak brightness. We find that six out of the eight systems require an F-type primary star with a K-type companion with large eccentricities. At the same time, we find that optically thin disks, modelled using a Henyey-Greenstein phase function are also able to generate these broad brightening events. Five of the eight observed objects can be described with this new hypothesis in the absence of RV observations. As the other three are not well-described by the disk model, we conclude that they are indeed heartbeat stars.

This chapter has been submitted to MNRAS

2.1 Introduction

With dedicated surveys and space telescopes such as Kepler (Borucki et al., 2010) and TESS (Ricker et al., 2015), thousands of exoplanet candidates have been found due to the high precision photometry achieved by these missions—tens of parts per million reported by Christiansen et al. (2012) for Kepler. The Kepler mission is a rich data source with light curves from hundreds of thousands of objects. We know that many physical processes can cause variations in a light curve and by closely studying them we might be able to better understand what is happening around a star. Motivated by finding signals in Kepler data not necessarily due to exoplanets, and to probe other astrophysical processes, recent work by Wheeler and Kipping (2019) has demonstrated a new automatic flagging algorithm that can extract periodic signals that were previously only detected through power-spectrum analysis and visual inspection. Their newly identified objects show mainly brightening of the measured light curves. In this work we focus on eight of these objects and look at two different processes that could result in the increase in flux seen in the data over short periods of order 20 days.

In the Kepler data set more than one hundred heartbeat systems have been identified and studied to date with both light curve and radial-velocity data (Welsh et al., 2011; Thompson et al., 2012; Shporer et al., 2016; Beck, P. G. et al., 2014). Exciting and dynamic systems, they show a photometric signal even when there is no eclipse. The observed photometric signal is due to tidal distortion, heating, Doppler beaming, and other effects. In this paper we first consider the increase in flux (De Cat et al., 2000; Fuller, 2017) due to the tidal interaction of heartbeat systems; a well accepted explanation for the observed brightening in the light curves.

From the NASA Exoplanet Archive we also know of multiple exoplanets with orbital periods on the order of 20 days – similar to the periods of the objects we consider in this paper. In some cases, such as Brogi et al. (2012) and Lamers et al. (1997), there is a slight increase in light before or after the transit event hidden among the star's own intrinsic variability– further complicating the light curve analysis, and indicating certain phenomena are potentially being detected for the first time. We also expect a high number of grazing events of exoplanets in the Kepler data as any system orientation is equally likely compared to an observer. Observations of PDS70 have revealed the presence of circumplanetary disks around both PDS70-b (Christiaens et al., 2019) and PDS70-c (Isella et al., 2019). Andrews et al. (2018) shows there are many proto-planetary disks with many geometries. Finally, Ansdell et al. (2016) detects a protoplanetary disk around ten young late-K and M dwarf stars. We, therefore, consider an alternative model where forwards scattering from a cloud of dust results in a brightening in the light curve. The cloud of dust could be an exoplanet enshrouded by a disk of dust with a system geometry. Or alternatively, it could be a protoplanetary disk with gaps and specific geometry such that the observed brightening is produced due to the inclination of the system.

The rest of the paper is structured as follows; in Section 2.2, we describe the eight objects seen in the Kepler data and explain the data reduction performed. We then consider brightening due to tidal interaction of a binary star system, in Section 2.3. The results from fitting to this model are presented in Section 2.3.2. We then investigate forward scattering from an optically thin disk in Section 2.4 and show the results from fitting to such a model in Section 2.4.2. We discuss and compare the results from both models in Section 2.5. Lastly, we summarize our results and conclusions in Section 2.6.

2.2 Objects of Interest: Kepler data reduction & analysis

We look at the previously unknown periodic signals detected by the non-parametric detection algorithm of Wheeler and Kipping (2019). Of these 18 previously unreported periodic objects, we look at the eight objects detected with high confidence. Table 2.1 contains the Kepler identification numbers, the Kepler magnitudes, and the periods determined in this work as well as the number of available Kepler quarters for which data was taken for the given object. Using the python package LightKurve (Lightkurve Collaboration et al., 2018), we process the Kepler data. We make use of the pre-search data conditioning SAP flux (PDCSAP) generated by the Kepler Data Processing Pipeline which has removed long term trends using co-trending basis vectors (Smith et al., 2012). Note that we do not need to filter specifically for the long-cadence exposure time since the orbital periods of our objects are sufficiently long enough—on the order of tens of days. We combine the Kepler data for all quarters available by stitching them together after normalizing them. Then we remove all nan values and any outliers that are 5σ above the mean. Finding the periodogram of the data, we determine the period by finding the maximum power for a frequency that is greater than 12 hours (in order to avoid any intrinsic stellar variations) and fold the data on the identified periods, generating light curves as a function of orbital

Table 2.1: Summary of the Kepler systems used in this work, including their Kepler magnitudes (K_p), orbital periods ($P_{\rm orb}$) determined in this work, and the number of Kepler quarters available for each target. The amplitude and errors are the relative flux as defined by Wheeler and Kipping (2019) and provide an estimation of the confidence of the signal.

KIC ID	K_p [mag]	P_{orb} [days]	Amp [ppt]	Amp error [ppt]	# quarters
7837214	13.95	7.49	0.99	0.04	17
11397541	9.98	13.25	0.96	0.02	18
6862114	8.01	27.68	0.62	0.03	18
4371947	12.28	19.72	0.36	0.02	15
8694536	12.33	35.95	0.28	0.01	18
7870350	12.26	23.142	0.35	0.01	18
10737327	12.12	22.78	0.22	0.02	17
11498661	14.18	42.09	0.35	0.03	18

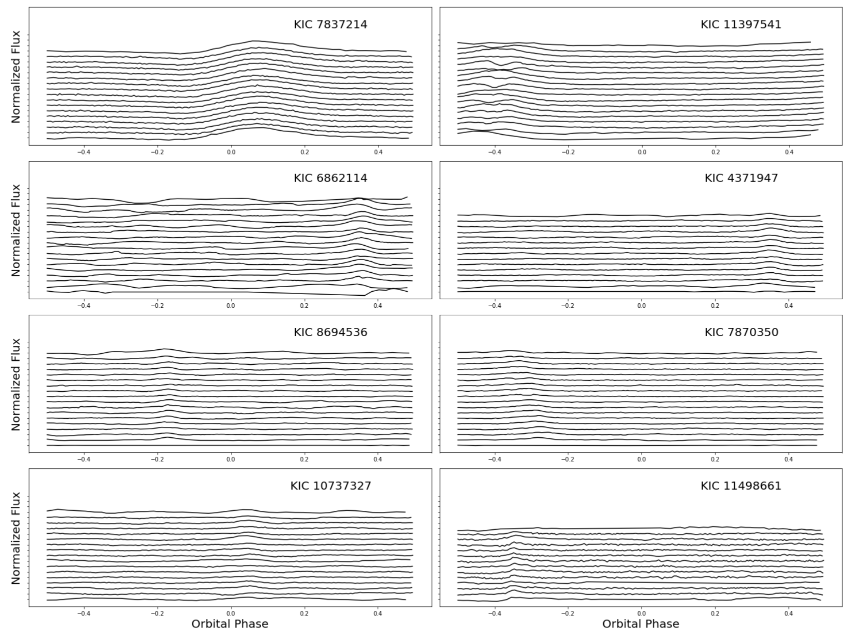

Figure 2.1: Stacked line plot showing all the light curves—flux as a function of orbital phase—for all available quarters for each of our OI. Each of the curves has been offset in flux by 0.00075. The brightening in flux can be seen in each quarter individually.

phase. The light curves are then binned by a factor of 5 in the orbital phase using the mean value. To have confidence in folded light curves, we repeated the above steps three additional times by randomly selecting three Kepler quarters each time. Doing so, we retrieve the same light curve shape and period. The periods we identify also agree with the periods found by Wheeler and Kipping (2019). For reference, the individual light curves of our systems are shown in Figure 2.1 with the individual behaviour of the periodic signal from all the Kepler quarters. The folded light curves from combining all the available quarters are shown in Figure 2.2. In all the light curves, we see a brightening over a large portion of the orbital phase. In the next sections we consider two different explanations for the observed brightening.

2.3 Brightening due to tidal effects in binary star system

As expressed by Wheeler and Kipping (2019), the increase in flux seen in the light curves can be explained by a heartbeat star. Light curves for heartbeat stars in Kepler data can be found in Thompson et al. (2012), Beck, P. G. et al. (2014), and Shporer et al. (2016); they have very similar light curve features to the ones in this work. The systems in this paper, however, are not yet identified in the Kepler binary star system

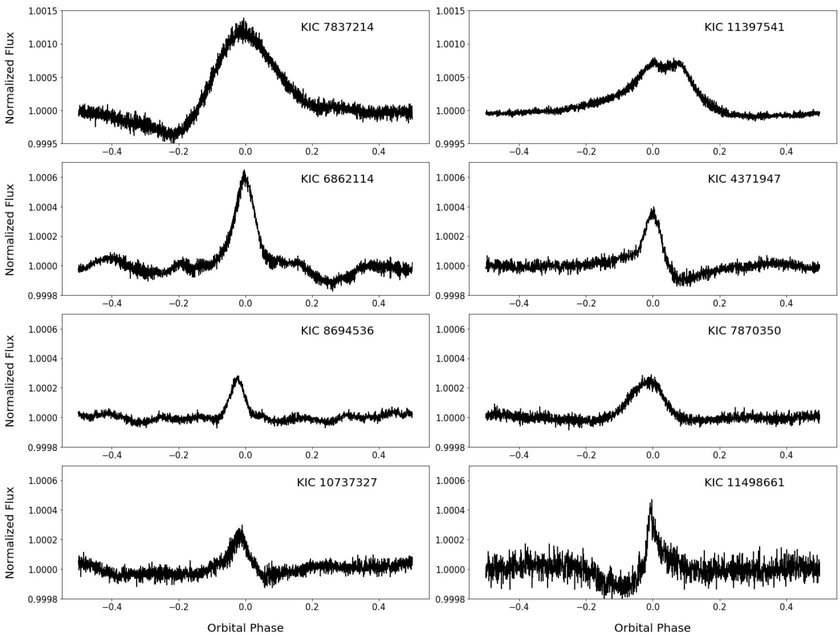

Figure 2.2: Folded Kepler light curves for the 8 systems showing normalized flux as a function of orbital phase. We stacked all the available Kepler quarters together and did not remove any low-frequency light-curve variations that might be associated with intrinsic stellar variability. This is done to indicate the signal-to-noise ratio of the observed brightening.

catalogue Kirk et al. (2016).

A heartbeat star is a binary star system with a large eccentricity ($e \geqslant 0.3$) and short orbital periods (typically less than 1 year; Fuller, 2017). The shape of the light curves are dominated by tidal forces Kumar et al. (1995), produce pulsations, Doppler beaming, and reflections. Their light curves show a strong "heartbeat-like" profile, hence the name. In this section we explore binary star systems as an explanation for our 8 systems.

2.3.1 Binary star system model

We model a binary stellar system with interacting tidal forces, making use of the PHOEBE 2.0 python package from Jones et al. (2019). PHOEBE 2.0 is an eclipsing binary modelling code that is a complete rewrite of the original PHOEBE legacy suite written by A. Prša and Zwitter (2005). We use the code to generate our forward model. Prša (2011) provides an overview of the geometry used within Phoebe 2.0. In our model the longitude of the ascending node is arbitrarily fixed to zero. The eccentricity of the two stars is taken to be the same. The computational load to generate a light curve with PHOEBE 2.0 is very high due to the requirements to run the model, including 1. non-circular orbits, 2. a Roche model to allow deformation of the star and therefore tidal effects, 3. limb darkening, 4. and the Kepler bandpass information. We, however, do not allow the two bodies to come close enough to be considered a contact binary system. Secondly, we do not include Doppler beaming which is difficult to accurately estimate, please see Phoebe documentation for more information. Therefore, we perform a brute-force curve fit (instead of a Bayesian approach, as in Section 2.4.1, that is otherwise too computationally intensive and expensive). Using Scipy's 'curve_fit' function, we determine a fit to the data. The effective temperature is taken from the Kepler catalogue Brown et al. (2011) which is derived from the observations and then we assume this value to be the primary's effective temperature. In the cases where no temperature is provided by Kepler, or when the Kepler value is right at the transition of stellar types, we take the value from Gaia Gaia Collaboration, Prusti, et al. (2016) and Gaia Collaboration, Brown, et al. (2018). From the effective temperature and therefore the stellar type assuming the star is main sequence, we constrain the mass and radius of the primary star, providing the fitting routine with standard start values for a given stellar type. We then assume the secondary star is of the same stellar type, restricting the mass, radius, and temperature. If no good fit is found, the secondary star is instead assumed to be much smaller than the primary. We do this in order to minimize the effect of binary contamination. Contamination of the effective temperature from the Kepler catalogue results from the assumption that the object is a single star when it is instead an unresolved binary. The effective temperature for Kepler is valid for binary systems where the two stars are the same stellar type or the secondary is much smaller than the primary (see Pinsonneault et al., 2012). This method of fitting does not guarantee a global minimum. With tidal forces included, the main contributors to the shape of the light curve are the eccentricity, the inclination of the system, and the argument of periastron; e, i, and ω, respectively. By varying these parameters we can reproduce almost all the features seen in the various Kepler light curves. The best fit parameters are shown in Table 2.2. We note that the ability to model of the light curves in Phoebe is limited without due to the large parameter space and parameter degenercies that is unaided by the lack of data in the form of spectroscopic values and radial velocity data. A complete overview of the PHOEBE model is given in Jones et al. (2019).

2.3.2 Results

The best-fit curves are shown in Figure 2.3. The overall shapes of the light curves are well reproduced with the binary model. Six out of the eight systems are best modelled by an F-type primary star and a K-type secondary. One system contains a G-type primary and a K-type secondary while another system requires both stars to be K-type. In some cases, there is missing flux before or after the peak itself as the curve is asymmetric such as KIC 7837214, KIC 11397514, KIC 4371947, KIC 10737327, and KIC 11498661. The asymmetry of the curves also leads to a slight overestimation of the width of the peak as seen in KIC 8694536, KIC 4371947, and KIC 10737327. The e for all but one of the systems is larger than 0.3 indicating that these could be heartbeat systems. The fitted i of all the systems are all less than 40°.

Table 2.2: Results from the curve fitting routine of the binary star system forward model using Phoebe 2.0. The masses, radii, temperatures, and stellar types are given for both the primary and secondary stars indicated by $_1$ and $_2$, respectively. The primary's effective temperature (T_1) is estimated from either the Kepler or the Gaia catalogues. The eccentricity, e, and inclination, i, are assumed to be the same for both stars.

KIC ID	$M_1[M_\odot]$	$R_1[R_\odot]$	T_1 [K]	Stellar type$_1$	$M_2[M_\odot]$	$R_2[R_\odot]$	T_2 [K]	Stellar type$_2$	e	$i[°]$	$w[°]$
7837214	0.90	1.14	5774	G	0.50	0.90	4202	K	0.35	20	-170
11397541	1.10	1.20	6068	F	0.50	0.93	4460	K	0.50	25	86
6862114	1.10	1.30	7114	F	0.63	0.92	5173	K	0.62	10	50
4371947	1.10	1.20	6830	F	0.50	0.80	3975	K	0.44	37	170
8694536	1.10	1.20	6214	F	0.50	0.80	4000	K	0.55	15	170
7870350	1.10	1.30	6656	F	0.50	0.75	4000	K	0.37	34	0
10737327	1.10	1.30	6259	F	0.50	0.75	3930	K	0.35	37	35
11498661	0.75	0.95	5078	K	0.50	0.71	3917	K	0.68	35	0

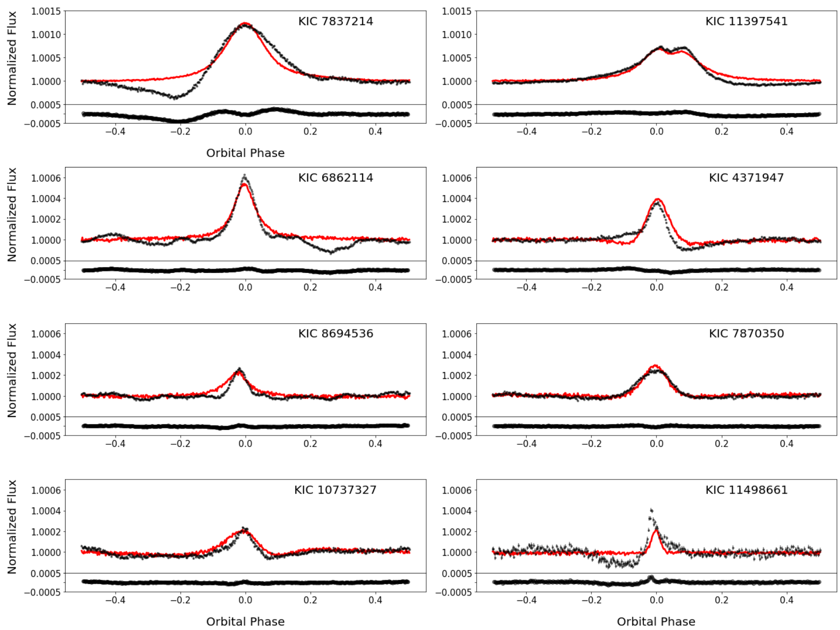

Figure 2.3: The resulting fits, in red, determined from standard curve fitting routine of a binary star system. Black in the top panel shows the Kepler data binned by a factor of 10 along with error bars. Note that the top subplots for objects KIC 7837214 and KIC 11397541 have a different y-scale than the other systems. The bottom panels of each subplot show the residual and is determined simply by taking the difference between the data and the model.

2.3.3 Analysis

Qualitatively, the binary system forward model does a good job reproducing the features (peak height, duration of brightening, and presence of an asymmetry) seen in the Kepler data. However, there is still over- and under- estimation of flux. The main reason arises from the fitting function itself—we are unable to easily perform a search of the entire parameter space while at the same time there is a degeneracy between the masses and the i of the system. Within a given stellar type, small changes in the masses and radii have little effect on the light curve. The dominant changes to the shape of the brightening come from varying i, e, and w. The asymmetric dip immediately before or after the peak brightness is where we see the greatest underestimation of flux in our model. This is most-likely due to missing physics in the binary model itself. We, however, have not removed any intrinsic stellar variations in the initial data reduction. The data used here have been binned, removing some variations, making the light curves appear relatively flat but at the same time remaining stellar variations could contribute by a small amount to the observed asymmetries. Both KIC 6862114 and KIC 8694536, however, show signs of sinusoidal fluctuations on the order of $10^{-}4$ in flux which become more obvious when looking at the unbinned data. These signals are similar to the tidally excited oscillations previously observed in Kepler heartbeat systems. However, this has been primarily for A-type stars that are much more massive (Guo et al., 2020) than the fitted masses in this work. The large eccentricity ($e > 0.5$) of both these systems might increase the strength of any tidally excited oscillations, resulting in the observed variations. Finally, as mentioned above the physics happening within these systems is extreme and complex; light curves for close eclipsing binary systems often appear to have an asymmetry that is not fully understood. This is known as the O'Connell effect (O'Connell, 1951). We might be seeing this in elliptical binary systems with the smallest periastron distances.

2.4 Forward scattering from optically thin cloud

The brightening of these light curves are also similar to what is observed in the Beta Pictoris light curve. The brightening seen there was explained using the scattering of a dust cloud and alternatively a comet tail by Lamers et al. (1997). In Section 2.1, we point out the abundance of disks at all different stages of an exoplanet's evolution and many different configurations of disks at different distances from the host star are possible. Since our objects have short orbital periods and are close-in, we expect that any gas would be blown away by stellar winds. Estimates of the equilibrium exoplanet temperature indicate that any exoplanets would be cool enough (less than 2000 K) to prevent sublimation of silicates, allowing for the existence of a dusty disk (see Appendix 2.B). Finally, in Brogi et al., 2012, there is evidence of dust around the close-in exoplanet KIC 12557548 b that the authors attribute to disintegration. We, therefore, form a simple forward scattering model of a dust cloud and fit our model to the data.

In Figure 2.4, we show a cartoon of possible system geometries resulting in the observed light curves. We consider an inclined disk of dust that enshrouds a compact object such as a planet or protoplanet. Depending on the inclination of the disk, the forward scattering occurs either before or after the inferior conjunction of the hidden body. We model the occulter as a grey dust cloud with a radial distribution consistent with the two-dimensional Gaussian distribution which can represent many physical distributions easily (e.g., grazing effects and large inclination, a gaseous exoplanet transit versus a rocky planet, or even something not due to a planet at all) and allow for a good fit of the forward scattering. By using a Gaussian in our model, we can emphasize the forward scattering and not the potential occultation (to explain the asymmetry seen in the light curves) that in itself is not sufficient to cause the brightening (and which should be a minor effect).

2.4.1 Simplified Model

Assuming the increase in brightness is due to an optically thin disk passing in front of the host star, we can write the flux of the light curve, normalized to the star's flux, as follows:

$$\frac{f(\Theta)}{f_*} = 1 + \frac{f_{sca}(\Theta)}{f_*} + \frac{f_{occ}(\frac{\Theta}{2\pi})}{f_*} \tag{2.1}$$

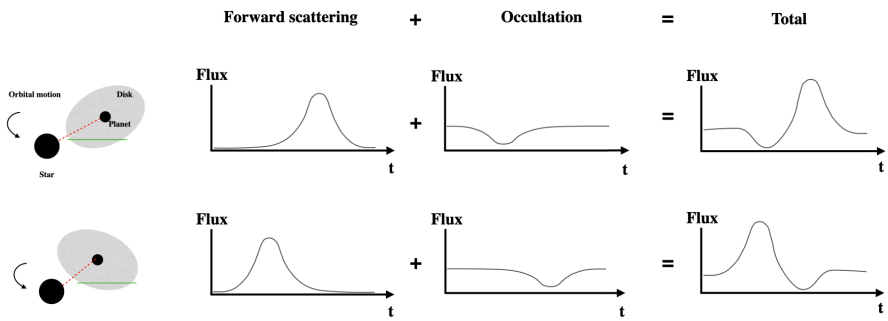

Figure 2.4: Diagram of the forward scattering and eclipse by a disk around a substellar companion orbiting the primary star. A star is orbited by a non-transiting substellar companion that is shrouded by a disk of dust. The long axis of the projected disk is tilted with respect to the orbital path of the companion, such that the brightening due to forward scattering of dust causes a peak in the observed flux that is offset in time with respect to the midpoint of the eclipse caused by the transit of the star behind the chord (green line) of the disk.

where f_* is the flux from the star and $f(\Theta)$ is the brightness variation of the system as a function of the scattering angle Θ. Taking the forward scattering flux, $f_{sca}(\Theta)$, to be from an optically thin disk, we can then write it as a function of the scattering phase function, $P(\Theta)$, and the effective scattering surface for an optically thin disk Σ_{sca}^{thin}.

$$\frac{f_{sca}(\Theta)}{f_*} = \frac{\Sigma_{sca}^{thin} P(\Theta)}{d^2} \tag{2.2}$$

with d being the distance from the star to the object. We take $P(\Theta)$ to be the Henyey-Greenstein phase function.

$$P(\Theta) = \frac{1}{4\pi} \frac{1-g^2}{(1+g^2+2g cos(\Theta))^{3/2}} \tag{2.3}$$

Due to the geometry of the system, the scattering angle can be directly related to the orbital phase, ϕ, via $\Theta = 2\pi\phi$. The Henyey-Greenstein parameter, g, can range from -1 to 1 with values between 0 and 1 resulting in forward scattering. For completeness, we also include an occultation component in our model that might occur if there is an optical thick/grey component of the disk in the system. We fit the occultation to a Gaussian function shown in Equation 2.4 with an amplitude A, mean phase offset (ϕ_0), and a standard deviation σ.

$$\frac{f_{occ}(\phi)}{f_*} = A * \exp\left(\frac{(\phi-\phi_0)^2}{2\sigma^2}\right) \tag{2.4}$$

Using Equation 2.1 as our forward model, we use a Bayesian approach to fit our model to the data using a Markov Chain Monte Carlo (MCMC) method. We make use of the python package emcee written by Foreman-Mackey et al. (2013), which is an implementation of an affine invariant MCMC ensemble sampler from Goodman and Weare (2010). We first estimate the distance of the object by assuming a circular orbit (see Table 2.3). We assume flat priors, and run 250 walkers with 1×10^5 steps all starting from different initial values. To remove contamination from the burn-in effect, we discard the first quarter. The best fit parameters are determined from the posterior distributions.

2.4.2 Results

We report the best fit values and their uncertainties in Table 2.3 and show the results of the best fit from the MCMC fitting method in Figure 2.5. From the residuals shown in the figure, we see that the simplified model is in good agreement with the data. The g values all lie between 0.4 and 0.9, as expected for forward scattering. For six of the systems, the Gaussian component results in an A on the order of 10^{-4} and σ between 0.03 and 0.10. The mean phase offset is the difference in phase from the zero-point of the orbital phase. For KIC 6862114 and KIC 8694536 the values of $A \sim 10^{-10}$, meaning that the Gaussian component is not needed to fit the data and the values are reported as zeros.

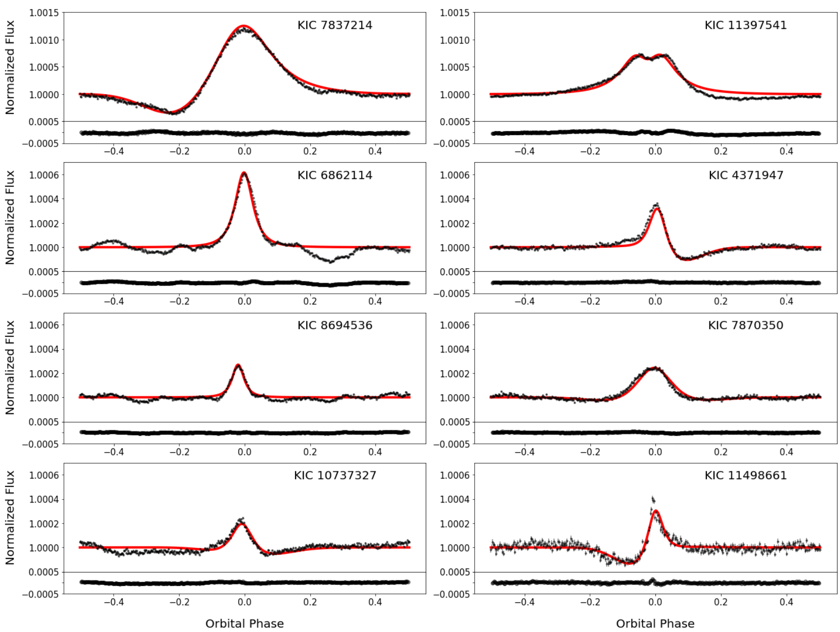

Figure 2.5: The resulting fits, in red, determined from the posterior distribution of the MCMC fit. Black in the top panel shows the Kepler data binned by a factor of 10 along with error bars. Note that the top plots for objects KIC 7837214 and KIC 11397541 have a different y-scale than the other systems. The bottom panels of each subplot show the residual, which is determined by simply taking the difference between the data and the model.

Table 2.3: The different model parameters as determined by MCMC fit. The distance, d, is determined from assuming a circular orbit and given as input into the forward model. The fitted parameter is the 50th percentile of the samples in the marginalized distributions, while the uncertainties are determined from the 16th and 84th. If $A < 10^{-10}$, we simply report it as zero, and the contribution from the Gaussian is negligible.

KIC ID	d [AU]	$a_{thin}[\mathrm{R}_s^2]$	g	ϕ_0	σ	A
7837214	0.073	$0.925^{+0.024}_{-0.026}$	$0.434^{+0.005}_{-0.005}$	$-0.199^{+0.004}_{-0.004}$	$0.097^{+0.003}_{-0.003}$	$5.263\text{E-}4^{+1.317\text{E-}5}_{-1.436\text{E-}5}$
11397541	0.112	$1.066^{+0.023}_{-0.024}$	$0.577^{+0.001}_{-0.001}$	$0.031^{+0.001}_{-0.001}$	$0.025^{+0.000}_{-0.000}$	$4.657\text{E-}4^{+5.495\text{E-}5}_{-5.769\text{E-}5}$
6862114	0.195	$1.263^{+0.047}_{-0.048}$	$0.773^{+0.005}_{-0.005}$	0.	0.	0.
4371947	0.161	$0.533^{+0.145}_{-0.191}$	$0.771^{+0.024}_{-0.021}$	$0.061^{+0.015}_{-0.019}$	$0.069^{+0.011}_{-0.007}$	$1.527\text{E-}4^{+2.34\text{E-}5}_{-3.614\text{E-}5}$
8694536	0.218	$0.234^{+0.023}_{-0.025}$	$0.842^{+0.010}_{-0.009}$	0.	0.	0.
7870350	0.170	$1.853^{+0.536}_{-0.818}$	$0.551^{+0.039}_{-0.038}$	$-0.019^{+0.008}_{-0.008}$	$0.129^{+0.008}_{-0.013}$	$1.594\text{E-}4^{+5.598\text{E-}5}_{-8.240\text{E-}5}$
10737327	0.161	$0.215^{+0.065}_{-0.091}$	$0.721^{+0.036}_{-0.035}$	$0.004^{+0.01}_{-0.016}$	$0.095^{+0.011}_{-0.011}$	$1.130\text{E-}4^{+2.909\text{E-}5}_{-3.967\text{E-}5}$
11498661	0.212	$0.215^{+0.032}_{-0.039}$	$0.790^{+0.017}_{-0.016}$	$-0.047^{+0.002}_{-0.004}$	$0.066^{+0.005}_{-0.005}$	$1.817\text{E-}4^{+1.629\text{E-}5}_{-1.894\text{E-}5}$

2.4.3 Analysis

In this section we discuss what the light curves and best fit parameters mean for a physical system. Although we suggest the system as seen in Figure 2.4, our simple model could indeed represent many other geometries, including the solid body being indeed a third body to the star and dust cloud or disk. From the light curves in Figure 2.2 we see that the brightening of the light curve due to the forward scattering of the thin disk spans $20-60\%$ of the orbital phase. The brightening is due to the scattering properties of the dust and the viewing angle of the observer. The scattering properties are represented by the g value of the Henyey-Greenstein function. For our g values, we find smaller values for smaller distances as expected from Lamers et al. (1997) and Brogi et al. (2012), with the g values increasing for larger distances. The g value can also be used as a tracer for the type of dust causing the forward scattering. The effective scattering surface area required for the observed brightening is not significantly large and the radius of the required optically thin disk for a given surface area is smaller than the Hill Sphere radius of the system (see Appendix 2.A for more details).

For the occultation due to our Gaussian term, we look at the σ values reported in Table 2.3. The duration of dip due to the grey dust should span no more than 1/6-th the orbital phase. Using the σ in Table 2.3, we find the full-width-half-maximum (FWHM; an estimation of the dip duration) for KIC 787214, KIC 7870350, and KIC 10737327 all are much larger than 1/6-th the orbital phase. Assuming we have an exoplanet at the center of the disk, the exoplanet's mass necessary to have such a large Hill sphere radius such that the dust can span such a large portion of the orbit would result in an exoplanet of approximately 16 M_J. We estimate this value by taking the Hill sphere radius to be 1/6-th the orbit; assuming the host star to be one solar mass, we solve for the secondary mass, m (i.e., $0.17 = (\frac{m}{3*1\mathrm{M_J}})^{1/3}$). Such a large exoplanet (or brown dwarf) would change the observed light curve at such short orbital periods. Specifically, the transit depth would be approximately 1% and not the observed 0.1-0.3%. Therefore objects with FWHM larger must either be modelled by a second Henyey-Greenstein phase function with a g value less than 0, or be heartbeat binary stars. KIC 4371947 and KIC 11498661 have FWHMs just under 1/6-th the orbital phase while the FWHM of the other systems are much smaller.

2.5 Discussion and comparison of the two models

In Section 2.3, we apply an eccentric binary star-system model and present results of fitting it to the data. All the systems require an $e > 0.3$. This, in combination with the short orbital periods, indicates the observed light curves can be explained by current heartbeat system models. However, Figure 2.3 shows that although the binary model does a good job of reproducing the overall shape of the light curves, there is still a flux mismatch in many cases— most notably, KIC 783714, KIC 4371947 KIC 8694536, and KIC 11498661. Due to the degeneracy of the masses and the inclination, the curve fitting algorithm does not find a solution that matches the observed curves.

In combination with the difficulties in modelling close binaries and certain physical processes (such as flow of material between the two objects at closest approach and Doppler beaming) missing from the model itself, the flux discrepancy is in itself not sufficient to rule out these being true binary systems.

While the simple heartbeat model is a good fit for eight of the systems, we consider a model that includes forward scattering from an optically thin disk of dust surrounding a non-transiting exoplanet that is orbiting the host star in Section 2.4. A circumsecondary disk that is tilted with respect to the path of the planet's orbit will produce a forward scattering peak well approximated by a Gaussian profile, but that is then offset in time with respect to the transit of the star behind a chord across the dust disk (see Figure 2.4). Our scattering model provides a good fit to the data, see Figure 2.5, and provides a qualitatively better explanation for some objects than the binary system. From Table 2.3, we note that the uncertainties (the 18th and 84th percentiles) reveal that a_{thin} is not well constrained by the data for KIC 4371947 and KIC 7870350. There is a degeneracy between the scattering surface area and the amplitude of the Gaussian component. Despite these limitations, the simplified model shows that with forward scattering, we can obtain the amplitude and duration of the brightening seen in all of our light curves.

The Gaussian component σ is too large, indicating that a 16 M_J exoplanet would be needed to allow for the dust to span such a large portion of the orbit, for three of the systems: KIC 787214, KIC 7870350, and KIC 10737327. Given the features of the light curves, we see no evidence for the existence of such a massive exoplanet. While it is possible to create more complex dust models that we could fit to the date, we expect these objects to indeed be heartbeat stars. The remaining five could be described by either model. For KIC 6862114 and KIC 8694536, the brightening is symmetric and does not require any occultation, indicating that inclination of the system would have to be large such that the exoplanet would not pass in front of the star. For the other three systems, the model provides physically realistic values for both a companion and the disk.

Radial velocity measurements would further enable the type of system to be identified, as well as provide mass constraints for the systems. For KIC 787214, KIC 7870350, and KIC 10737327, for which the disk model is not able to describe the system, radial velocity measurements would confirm them as heartbeat systems. Assuming an eccentric binary system, the binary mass function can be written as in Equation 2.5.

$$f = \frac{M_2^3 sin^3 i}{(M_1 + M_2)^2} = \frac{P_{orb} K^3}{2\pi G}(1 - e^2)^{3/2} \tag{2.5}$$

K is the semi-amplitude of radial velocity curve and is related to the velocity of the largest object and the geometry of the system. Rearranging Equation 2.5 for K, we estimate the peak of the radial velocity signal with the values in Table 2.2 to be $6 - 21$km/s. In the case of the optically thin cloud, we would expect a very low peak velocity. Therefore, radial velocity data would be sufficient to distinguish which physical model is responsible for observed light curves. For the five objects that could be optically thin disks we would also expect a polarization signal. Due to the closeness of the expected disk to the host star, any polarized light from the disk itself would not be angularly resolved with an instrument such as VLT/SPHERE's (Beuzit et al., 2019) polarization subsystem ZIMPOL (Schmid et al., 2018). Since the star itself is unpolarized, any polarized light could be attributed to the disk. With such data of the system in combination with radiative transfer models, it is possible to put constraints on the dust mass.

2.6 Conclusion

In this paper we investigate eight systems identified in the Kepler data. We find that most of the light curves can be explained by a heartbeat binary star system with an F-type primary and a K-type companion. We do, however, see a discrepancy of flux for the asymmetric part of the light curves. While this could be due to physics not included in the heartbeat models, we also investigate whether the light curves can be explained by a simple forward scattering model composed of an optically thin disk around an exoplanet. We determine that five out of the eight observed light curves could be described in this manner. Further investigation of KIC 11397541, KIC 6862114, KIC 4371947, KIC 8694536, and KIC 11498661 using radial velocity and polarization measurements will therefore be needed to determine if they are heartbeat systems or dust clouds around an exoplanet. Follow-up radial velocity observations of KIC 787214, KIC 7870350, and KIC 10737327 could further be used to confirm them as heartbeat systems.

2.A Effective scattering area and disk size estimation

In Section 2.4, the forward scattering of an optically thin disk is fit to the observed Kepler data. One parameter estimated by the fit is the projected effective scattering area, Σ_{sca}^{thin}. From this we can estimate the radius of a thin circular disk with the same effective area using the following equation:

$$\Sigma_{scat}^{thin} = \int_0^r (1 - e^{-\tau_{sca}(p)})(\pi p) dp \tag{2.6}$$

where $\tau(p)$ is the optical depth along the line-of-sight through the cloud. Assuming an average optical depth over the entire optically thin disk, the equation becomes

$$\Sigma_{sca}^{thin} = (1 - e^{-\tau_{sca}})\pi r^2 \tag{2.7}$$

In Table 2.4, we report the radii for two different values of τ. We estimate the Hill Sphere radius for a $1M_J$ exoplanet in a circular orbit around an $1M_\odot$ star with the periods reported in Table 2.1. For reference, the Hill Sphere radius of the hot Jupiter HD 209458 b is 0.003 AU with an orbital period of 3.5 days and a mass of $0.71M_J$. In all cases of $\tau = 0.5$, the radii are smaller than the estimated Hill Sphere radii, while for $\tau = 0.1$ most are too large. However, these values do indicate that projected surface scattering areas found are realistic values.

2.B Equilibrium Temperature

In our optically thin model we assume the presence of a dusty disk with an exoplanet. Close into the host star, gas has most-likely been blown away by stellar winds. For dust to exist, however, the grains must be below their sublimation temperature. Sublimation temperature of dust differs depending on the dust composition. For example, carbon has a high sublimation temperature of 2000 K (Kobayashi et al., 2011) while silicates sublimates at 1500K (Kama, M. et al., 2009). We expect our dust disk to be formed from silicates. We therefore, estimate the temperature of the dusty gains by determining the equilibrium temperature of an exoplanet orbiting at that The equilibrium temperature, T_{eq} of an exoplanet orbiting around its host star is given by

$$T_{eq} = T(1-\alpha)^{0.25}(r/2a)^{0.5} \tag{2.8}$$

with T being the stellar temperature, r being the stellar radii, and α as the exoplanet's albedo. We then take the stellar temperature from Table 2.2 and estimate r from the stellar type. Therefore, assuming a black body ($\alpha = 0$), the upper limits for thee T_{eq} for our systems ranges from 500 K to 1100 K. These values are well below the sublimation temperature for silicate.

Table 2.4: Estimation of r_{sca}^{thin} for two different values of τ: 0.5 and 0.1. An estimation of the Hill Sphere radius is made from a $1M_J$ exoplanet in a circular orbit around a $1M_\odot$ star.

KIC ID	$a_{thin}[R_s^2]$	$r_{sca}^{thin}[AU] : \tau = 0.5$	$r_{sca}^{thin}[AU] : \tau = 0.1$	Hill Sphere radius [AU]
7837214	0.925	0.004	0.014	0.005
11397541	1.066	0.004	0.016	0.008
6862114	1.263	0.005	0.019	0.013
4371947	0.533	0.003	0.008	0.011
8694536	0.234	0.002	0.004	0.014
7870350	1.853	0.006	0.028	0.012
10737327	0.215	0.002	0.003	0.011
11498661	0.215	0.002	0.003	0.017

References

A. Prša, A. and T. Zwitter (July 2005). "A Computational Guide to Physics of Eclipsing Binaries. I. Demonstrations and Perspectives". In: *The Astrophysical Journal* 628.1, pp. 426–438.

Andrews, Sean M. et al. (Dec. 2018). "The Disk Substructures at High Angular Resolution Project (DSHARP). I. Motivation, Sample, Calibration, and Overview". In: *The Astrophysical Journal* 869.2, p. L41.

Ansdell, M. et al. (Jan. 2016). "YOUNG "DIPPER" STARS IN UPPER SCO AND OPH OBSERVED BY K2". In: *The Astrophysical Journal* 816.2, p. 69.

Beck, P. G. et al. (2014). "Pulsating red giant stars in eccentric binary systems discovered from Kepler space-based photometry - A sample study and the analysis of KIC6817". In: *A&A* 564, A36. DOI: 10.1051/0004-6361/201322477. URL: https://doi.org/10.1051/0004-6361/201322477.

Beuzit, J.-L. et al. (Sept. 2019). "SPHERE: the exoplanet imager for the Very Large Telescope". In: *Astronomy & Astrophysics*.

Borucki, William J. et al. (2010). "Kepler Planet-Detection Mission: Introduction and First Results". In: *Science* 327.5968, pp. 977–980.

Brogi, M., C. U. Keller, M. de Juan Ovelar, M. A. Kenworthy, R. J. de Kok, M. Min, and I. A. G. Snellen (Sept. 2012). "Evidence for the disintegration of KIC 12557548 b". In: *Astronomy and Astrophysics* 545, L5, p. L5. DOI: 10.1051/0004-6361/201219762. arXiv: 1208.2988 [astro-ph.EP].

Brown, Timothy M., David W. Latham, Mark E. Everett, and Gilbert A. Esquerdo (Oct. 2011). "Kepler Input Catalog: Photometric Calibration and Stellar Classification". In: *The Astronomical Journal* 142.4, 112, p. 112. DOI: 10.1088/0004-6256/142/4/112. arXiv: 1102.0342 [astro-ph.SR].

Christiaens, Valentin, Faustine Cantalloube, Simon Casassus, Daniel J. Price, Olivier Absil, Christophe Pinte, Julien Girard, and Matias Montesinos (June 2019). "Evidence for a Circumplanetary Disk around Protoplanet PDS 70 b". In: *The Astrophysical Journal* 877.2, p. L33.

Christiansen, Jessie L. et al. (Dec. 2012). "The Derivation, Properties, and Value of Kepler's Combined Differential Photometric Precision". In: *Publications of the ASP* 124.922, p. 1279.

De Cat, P., C. Aerts, J. De Ridder, K. Kolenberg, G. Meeus, and L. Decin (Mar. 2000). "A study of bright southern slowly pulsating B stars. I. Determination of the orbital parameters and of the main frequency of the spectroscopic binaries". In: *Astronomy and Astrophysics* 355, pp. 1015–1030.

Foreman-Mackey, Daniel, David W. Hogg, Dustin Lang, and Jonathan Goodman (Mar. 2013). "emcee: The MCMC Hammer". In: *Publications of the Astronomical Society of the Pacific* 125.925, pp. 306–312.

Fuller, Jim (Sept. 2017). "Heartbeat stars, tidally excited oscillations and resonance locking". In: *Monthly Notices of the Royal Astronomical Society* 472.2, pp. 1538–1564. ISSN: 1365-2966. DOI: 10.1093/mnras/stx2135. URL: http://dx.doi.org/10.1093/mnras/stx2135.

Gaia Collaboration, A. G. A. Brown, et al. (Aug. 2018). “Gaia Data Release 2. Summary of the contents and survey properties”. In: *Astronomy and Astrophysics* 616, A1, A1. DOI: 10.1051/0004-6361/201833051. arXiv: 1804.09365 [astro-ph.GA].

Gaia Collaboration, T. Prusti, et al. (Nov. 2016). “The Gaia mission”. In: *Astronomy and Astrophysics* 595, A1, A1. DOI: 10.1051/0004-6361/201629272. arXiv: 1609.04153 [astro-ph.IM].

Goodman, Jonathan and Jonathan Weare (2010). “Ensemble samplers with affine invariance”. In: *Commun. Appl. Math. Comput. Sci.* 5.1, pp. 65–80.

Guo, Zhao, Avi Shporer, Kelly Hambleton, and Howard Isaacson (Jan. 2020). “Tidally Excited Oscillations in Heartbeat Binary Stars: Pulsation Phases and Mode Identification”. In: *The Astrophysical Journal* 888.2, p. 95. DOI: 10.3847/1538-4357/ab58c2. URL: https://doi.org/10.3847%2F1538-4357%2Fab58c2.

Isella, Andrea, Myriam Benisty, Richard Teague, Jaehan Bae, Miriam Keppler, Stefano Facchini, and Laura Pérez (July 2019). “Detection of Continuum Submillimeter Emission Associated with Candidate Protoplanets”. In: *The Astrophysical Journal* 879.2, p. L25.

Jones, David, Kyle E. Conroy, Martin Horvat, Joseph Giammarco, Angela Kochoska, Herbert Pablo, Alex J. Brown, Paulina Sowicka, and Andrej Prsa (Dec. 2019). “Physics of Eclipsing Binaries. IV. The impact of interstellar extinction on the light curves of eclipsing binaries”. In: *arXiv e-prints*, arXiv:1912.09474.

Kama, M., Min, M., and Dominik, C. (2009). “The inner rim structures of protoplanetary discs”. In: *Astronomy and Astrophysic* 506.3, pp. 1199–1213. DOI: 10.1051/0004-6361/200912068. URL: https://doi.org/10.1051/0004-6361/200912068.

Kirk, Brian et al. (Mar. 2016). “Kepler Eclipsing Binary Stars. VII. The Catalog of Eclipsing Binaries Found in the Entire Kepler Data Set”. In: *The Astronomical Journal* 151.3, 68, p. 68. DOI: 10.3847/0004-6256/151/3/68. arXiv: 1512.08830 [astro-ph.SR].

Kobayashi, Hiroshi, Hiroshi Kimura, Sei-ichiro Watanabe, Tetsuo Yamamoto, and Sebastian Müller (Oct. 2011). “Sublimation temperature of circumstellar dust particles and its importance for dust ring formation”. In: *Earth, Planets and Space* 63.10, pp. 1067–1075. ISSN: 1880-5981. DOI: 10.5047/eps.2011.03.012. URL: http://dx.doi.org/10.5047/eps.2011.03.012.

Kumar, Pawan, Chi On Ao, and Eliot J. Quataert (Aug. 1995). “Tidal Excitation of Modes in Binary Systems with Applications to Binary Pulsars”. In: *The Astrophysical Journal* 449, p. 294. DOI: 10.1086/176055. arXiv: astro-ph/9503053 [astro-ph].

Lamers, H. J. G. L. M., A. Lecavelier Des Etangs, and A. Vidal-Madjar (Dec. 1997). “Beta Pictoris light variations. II. Scattering by a dust cloud”. In: *Astronomy & Astrophysics* 328, pp. 321–330.

Lightkurve Collaboration et al. (Dec. 2018). *Lightkurve: Kepler and TESS time series analysis in Python*. Astrophysics Source Code Library.

O’Connell, D. J. K. (Aug. 1951). “The so-called periastron effect in close eclipsing binaries ; New variable stars (fifth list)”. In: *Publications of the Riverview College Observatory* 2.6, pp. 85–100.

Pinsonneault, Marc H., Deokkeun An, Joanna Molenda-Żakowicz, William J. Chaplin, Travis S. Metcalfe, and Hans Bruntt (Mar. 2012). "A REVISED EFFECTIVE TEMPERATURE SCALE FOR THE KEPLER INPUT CATALOG". In: *The Astrophysical Journal Supplement Series* 199.2, p. 30. DOI: 10.1088/0067-0049/199/2/30. URL: https://doi.org/10.1088%2F0067-0049%2F199%2F2%2F30.

Prša, A. (Sept. 2011). "PHOEBE Scientific Reference". In: *villanova university, college of arts and sciences, dept. of astronomy and astrophysics*.

Ricker, George R. et al. (Jan. 2015). "Transiting Exoplanet Survey Satellite (TESS)". In: *Journal of Astronomical Telescopes, Instruments, and Systems* 1, p. 014003.

Schmid, H. M. et al. (Nov. 2018). "SPHERE/ZIMPOL high resolution polarimetric imager. I. System overview, PSF parameters, coronagraphy, and polarimetry". In: *Astronomy & Astrophysics* 619, A9.

Shporer, Avi, Jim Fuller, Howard Isaacson, Kelly Hambleton, Susan E. Thompson, Andrej Prša, Donald W. Kurtz, Andrew W. Howard, and Ryan M. O'Leary (Sept. 2016). "RADIAL VELOCITY MONITORING OFKEPLERHEARTBEAT STARS". In: *The Astrophysical Journal* 829.1, p. 34.

Smith, Jeffrey C. et al. (Sept. 2012). "Kepler Presearch Data Conditioning II - A Bayesian Approach to Systematic Error Correction". In: *Publications of the Astronomical Society of the Pacific* 124.919, p. 1000. DOI: 10.1086/667697. arXiv: 1203.1383 [astro-ph.IM].

Thompson, Susan E. et al. (July 2012). "A Class of Eccentric Binaries with Dynamic Tidal Distortions Discovered with Kepler". In: *The Astrophysical Journal* 753.1, 86, p. 86. DOI: 10.1088/0004-637X/753/1/86. arXiv: 1203.6115 [astro-ph.SR].

Welsh, William F. et al. (Nov. 2011). "KOI-54: The Kepler discovery of tidally excited pulsations and brightenings in a highly eccentric binary". English (US). In: *Astrophysical Journal, Supplement Series* 197.1. ISSN: 0067-0049. DOI: 10.1088/0067-0049/197/1/4.

Wheeler, Adam and David Kipping (Mar. 2019). "The weird detector: flagging periodic, coherent signals of arbitrary shape in time-series photometry". In: *Monthly Notices of the Royal Astronomical Society* 485.4, pp. 5498–5510.

Chapter 3

Performance of AO predictive control in the presence of non-stationary turbulence

> “Go back?" he thought. "No good at all! Go sideways? Impossible! Go forward? Only thing to do!”
>
> J.R.R. Tolkien, *The Hobbit*

Summary

The performance of current high-contrast imaging systems is limited at small angular separations, preventing the direct imaging of Earth-size exoplanets close to their host stars. One primary cause of this limitation is the performance of the extreme adaptive optics (AO) system, which is dominated by the servo-lag error at small angular separations. Prediction of the turbulence induced optical phase can be used to help reduce this servo-lag error. Most AO systems today make use of an integral control law, resulting in a phase correction that is proportional to the current measured wavefront. This approach does not take into account the evolution of the wavefront phase fluctuations between measurement and correction. To account for the changes during the servo-lag, we focus on the implementation of different predictive control strategies that estimate how the wavefront phase fluctuations evolve over a time horizon equal to the servo-lag. Furthermore, the statistical properties of the turbulence phase are non-stationary and might have a significant impact on the performance of AO systems for high-contrast imaging systems. We therefore include non-stationary turbulence in our analysis. First, we model the non-stationary properties of the atmosphere using a von Kárman covariance function which can incorporate variations in time of the Fried parameter, outer scale, and wind velocity. We then vary the Fried parameter using an ARIMA model and simulate increases in wind speed using both ramp and step-like jumps in wind speed. Using this new disturbance model of turbulence, the performance of three different predictors – based on a steady state, recursive, and adaptive linear-minimum-mean-square-estimator (LMMSE) – is de-

This chapter is published as: Maaike van Kooten et al. (2017). “Performance of AO predictive control in the presence of non-stationary turbulence”. In: Instituto de Astrofisica de Canarias

termined under non-stationary conditions. We present the results of our simulations and compare our predictors with the common integrator. We show that, under our varying wind conditions, the root-mean-square wavefront error can increase by a factor of two for both the integrator and our predictors. From these tests, we conclude that a more in-depth study into non-stationary modelling is needed for atmospheric turbulence.

3.1 Introduction

Since the first direct images of an exoplanet by Marois et al. (2008), high-contrast imaging (HCI) has been a very active field. Capable of providing insight into planet formation, characterizing exoplanets' atmospheres, and searching for signs of habitability, HCI spatially separates the planet's photons from the ones emitted by the host star. With multiple dedicated instruments such as SPHERE (Beuzit et al., 2008) on the VLT, GPI (Macintosh et al., 2014) on Gemini South, and SCExAO (Jovanovic et al., 2015) on Subaru, many new techniques, better coronagraphs, and low noise detectors have been developed. These efforts have resulted in contrast levels of $10^{-4} - 10^{-5}$ at 0.5"-1" separation (see Kasper, 2012, for more details) in the near infrared as shown in Figure 3.1.

To answer the fundamental questions of: is the earth unique? is our solar system unique? and how did we form? we, however, need to aim for contrast levels of $10^{-7} - 10^{-9}$ at separations of 0.05" - 1" (for visible wavelengths) to find cold jupiters, neptunes, and rocky exoplanets. Currently, the limiting factor is the correction achieved by the adaptive optics (AO) systems within the HCI systems. Specif-

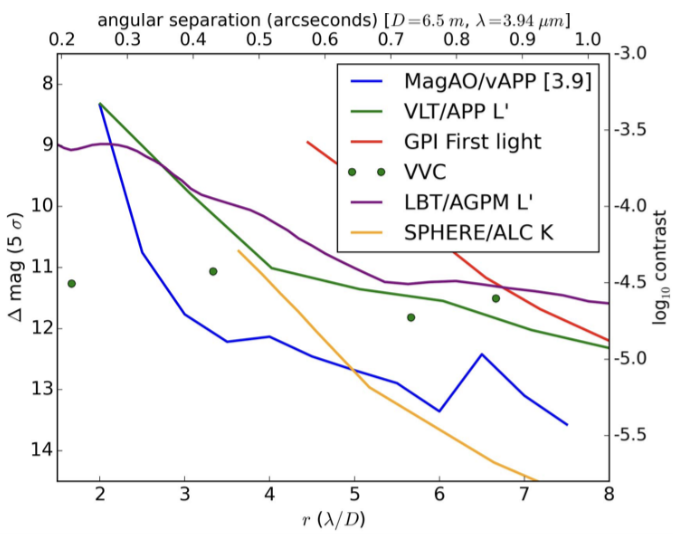

Figure 3.1: Current and future high contrast imaging capabilities from Otten et al. (2017) for various instruments and coronagraphs.

ically, the chromatic index and servo-lag error prevent us from observing at small separations as shown in Figure 3.2. Note that the fitting error can be reduced by increasing the number of actuators for the deformable mirror (DM). We focus on minimizing the servo-lag error. One approach is to run our AO system faster, requiring high speed DMs, fast wavefront sensors, and bright guide stars. Another approach is to focus on the evolution of wavefront phase fluctuations during the delay and correct for it using predictive control methods.

3.1.1 Predictive control in adaptive optics

As early as the 1970s (see Hardy, 1998), predictive control has been proposed to mitigate the effect of inevitable time delays in AO systems. To date, linear prediction has been very successful for tip-tilt compensation, especially when the source of the vibrations are well characterized, using linear quadratic Gaussian control (LQG; Kalman filter as the predictor; see Petit, Conan, Kulcsár, Raynaud, and Fusco, 2008; Doelman, Fraanje, and Breeje, 2011; Poyneer et al., 2016). Paschall and Anderson (1993), Le Roux et al. (2004), and Looze (2009) have all worked on the LQG controller for full atmospheric disturbance. Different varieties of the Kalman filter predictor have been implemented by Gray et al. (2014) and Massioni et al. (2011), and allow for filtering in real-time. For LGQ control, Petit, Conan, Kulcsár, and Raynaud (2009) have done laboratory testing while Correia et al. (2015) have performed on-sky tests. The data-driven H_2 optimal control implemented by Hinnen et al. (2007)

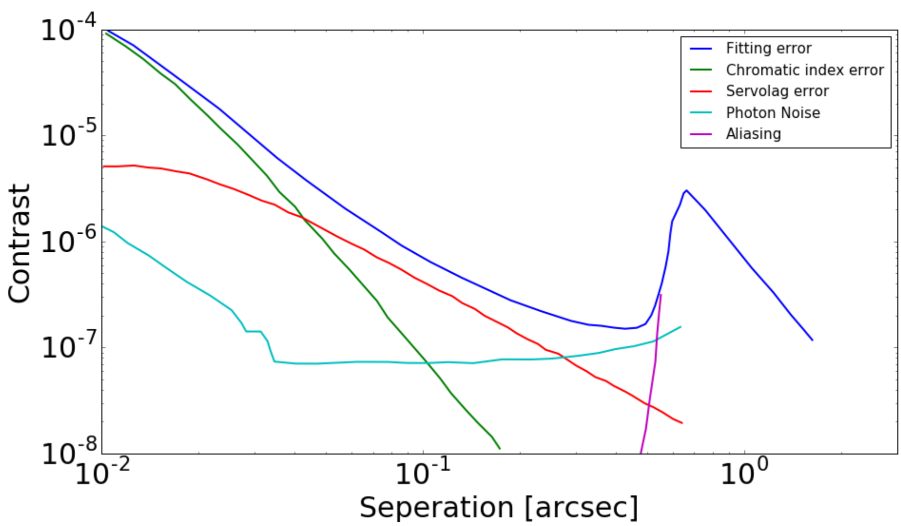

Figure 3.2: An example of an adaptive optics error budget showing that the servo-lag error is a major limitation of achievable contrast from Kasper (2012) for small angular separations. The fitting error can be reduced by increasing actuator density, and chromatic index error is reduced by sensing close to the science imaging wavelength.

was also tested on-sky and Doelman, Hinnen, et al. (2004) report a reduction in the temporal error. Finally, adaptive predictors have been proposed by Doelman, Fraanje, Houtzager, et al. (2009) to track the time-varying behavior of atmospheric turbulence.

Similar to any control problem, the characteristics of the (XAO) system, disturbance, and the time scales all influence the choice of the controller. Due to the variations of the mean and variance of phase aberrations, atmospheric turbulence induced phase fluctuations are non-stationary. If we account for this behavior, we will be able to find an improved predictive controller.

In this paper, we focus on understanding the input disturbance—atmospheric turbulence—of an AO system on short time scales. We look at how the disturbance model affects the performance of an AO system using basic prediction methods. The predictors are described in Section 3.2. The statistical behavior and the non-stationarities of turbulence are described in Section 3.3. We present, in Section 3.4, the results of our AO simulations with our new turbulence model and we discuss the impact of the results on predictor design. Finally, we outline our on-going and future work in Section 3.5.

3.2 Prediction filter design

We implement a linear finite order predictor. We denote a single phase point within a phase screen as y_i. Assuming that the future predicted value of a given phase point, $\hat{y}_i$ at the discrete time index $t+1$, is a linear combination of previous phase values, $\vec{w(t)}$ – a P x 1 column vector containing a collection of previous true phase values, we define the following, where P is the number of prior phase points:

$$\hat{y}_i(t+1) = \vec{A}_i \cdot \vec{w}(t) \tag{3.1}$$

$$\vec{w}(t) = \begin{pmatrix} y_0(t) & y_1(t) & y_2(t) & \dots & y_P(t) \end{pmatrix}^T \tag{3.2}$$

The prediction vector, $\vec{A}$, is then determined by minimizing the linear-minimum-mean-square-error cost function:

$$min_{\vec{A}_i} < ||y_i(t) - \vec{A}_i \vec{w}(t)||^2 > \tag{3.3}$$

The strength of this method is that the algorithm immediately extracts any spatio–temporal information from the data provided.

We implement our linear-minimum-mean-square estimator (LMMSE) in three different ways. A batch-method LMMSE is performed by storing measurements and determining the filter once enough measurements have been taken (after Q time steps). During this period, the LMMSE cannot be used and is considered offline.

Solving batch-wise, we first define

$$\vec{W} = \begin{pmatrix} \vec{w}(t) & \vec{w}(t-1) & \vec{w}(t-2) & \dots & \vec{w}(t-Q) \end{pmatrix} \tag{3.4}$$

and

$$\vec{Y} = \begin{pmatrix} y_i(t+1) & y_i(t) & y_i(t-1) & \dots & y_i(t-(Q+1)) \end{pmatrix}^T \tag{3.5}$$

By substituting $\vec{W}$ and $\vec{Y}$ for $\vec{w}$ and $\vec{y}$ in Equation 3.3, respectively, we find the prediction vector to be:

$$\vec{A}_i = \vec{W}^+ \vec{Y} \tag{3.6}$$

Here a pseudo inverse (denoted by $^+$) is performed to find the prediction vector. We can also rewrite this equation such that the prediction vector is the product of the inverse auto-covariance matrix and the cross-covariance vector.

$$\vec{A}_i = \mathbf{C}^+_{\vec{w}\vec{w}} \vec{C}_{\vec{w}\hat{y}} \tag{3.7}$$

The batch prediction vector is found, it is fixed for the rest of the simulation. By making use of the matrix inversion lemma, we can also form a recursive solution in which the covariance matrices are updated at each time step (Equations 3.8 and 3.9), removing the need for a pseudo inverse calculation (greatly reducing the computational load).

$$\mathbf{C}^{-1}_{\vec{w}\vec{w}}(t) = \mathbf{C}^{-1}_{\vec{w}\vec{w}}(t-1) - \frac{\mathbf{C}^{-1}_{\vec{w}\vec{w}}(t-1)\vec{w}(t-1)\vec{w}^T(t-1)\mathbf{C}^{-1}_{\vec{w}\vec{w}}(t-1)}{1+\vec{w}^T(t-1)\mathbf{C}^{-1}_{\vec{w}\vec{w}}(t-1)\vec{w}(t-1)} \tag{3.8}$$

$$\vec{C}_{\vec{w}\hat{y}}(t) = \vec{C}_{\vec{w}\hat{y}}(t-1) + \hat{y}(t-1)\vec{w}^T(t-1) \tag{3.9}$$

The recursive solution begins online immediately with the initial covariance being set to diagonal matrices with large values (as done with recursive least squares methods). The solution is quick to converge (within tens of iterations). The memory of the recursive solution is not limited and therefore all previous measurements affect the solution. We also use a regularization parameter to stabilize the recursion. Finally, we introduce an exponential forgetting factor to the recursive method, creating a simple adaptive method as our third LMMSE.

The LMMSE is convenient in that it allows us to choose the amount of input data used for prediction. To start, we assume the phase screen is simply blowing across the pupil (i.e., the phase fluctuations on the upper half of the pupil were measured—at some point in time—on the lower half of the pupil). This is known as the Taylor's Frozen Flow hypothesis. Hence, knowing how far (for example, units of subapertures) the phase screen is shifted, we limit the number of previous phase screens to one. We further limit it such that prediction at a given phase point only uses neighboring phase points (within a radius of 5 grid points) in the prediction

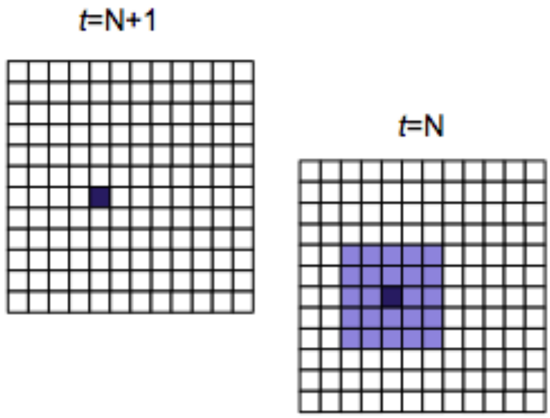

Figure 3.3: The phase points at t=N to use to predict the point at t=N+1.

algorithm (see Figure 3.3). This allows us to reduce the computation time as well as study how the LMMSE behaves for different amounts of input information.

3.3 Non-stationary turbulence model

The spatial behavior of atmospheric turbulence induced phase is often described by a power spectral density (PSD) function in which the Fried parameter (r_0), and outer scale (L_0) can be used to describe the spatial phase variations. We consider a spatial PSD and then derive the temporal PSD by applying Taylor's Frozen Flow hypothesis which involves knowing the wind speed, v, and direction (see Section 3.3.3). Many simulations use this prescription to model the input disturbance into the AO control loop. In this situation, any time-shift corresponds to a pure shift of the phase screen due to wind (for a single layer). However, we know that this Frozen Flow approach ignores the time varying behavior of the atmosphere. Therefore, we aim to understand how the atmospheric parameters vary, as a result of the non-stationary behavior of turbulence, and what impact the variations have on the system.

We make use of the von Kárman turbulence model by implementing an infinite phase screen algorithm developed by Assémat et al. (2006) that allows for the new rows of atmosphere to be generated online. Their use of a von Kárman covariance function to generate the phase allows for v and r_0 to be changed at each time step of the simulation. In Figure 3.4 we show the temporal PSD for three different cases: the reference case, the case where v is increased/decreased by 15 m/s, and the case when L_0 is increased/decreased by 30 m. Wind speed has a large effect on the PSD shape — if the shape of the PSD were to change like this in real life, we would have non-stationary turbulence. We do not, however, focus on L_0 as little information is known on its fluctuations and its affect on the temporal PSD is much less than that of changing v. To properly vary these parameters we need models that describe how the v and r_0 change in time.

3.3.1 Fried parameter variations

The Fried parameter is a measure of the strength of turbulence, with large numbers corresponding to weak turbulence and small values corresponding to strong turbulence. By definition, it is the path integral of the C_n^2 profile, and is therefore directly related to changes in the temperature fluctuations in the atmosphere. Available stereo-scidar measurements are unable to provide r_0 sampled at frequencies greater than 1 Hz. Using wavefront sensor data, however, Doelman and Osborn (2016) determined a fractional ARIMA model to describe the evolution of r_0 at La Palma on the time interval of 100 seconds. We adopt this model, creating a time series by assuming the r_0 remains constant over these 100 seconds. We feed this series into our atmospheric phase generator. We also look at a constantly decreasing r_0, representative of how seeing might improve over the course of a night.

3.3.2 Wind variations

Although much work has been done on the variation of v over long time scales, including the van der Hoven (1957) PSD and time evolving PSD for applications in civil engineering by Deodatis et al. (2014), we were unable to find an appropriate model useful for our purposes. Moreover, the slope of the PSD changes significantly depending on the altitude and geometry of the location. Also, the behavior of wind

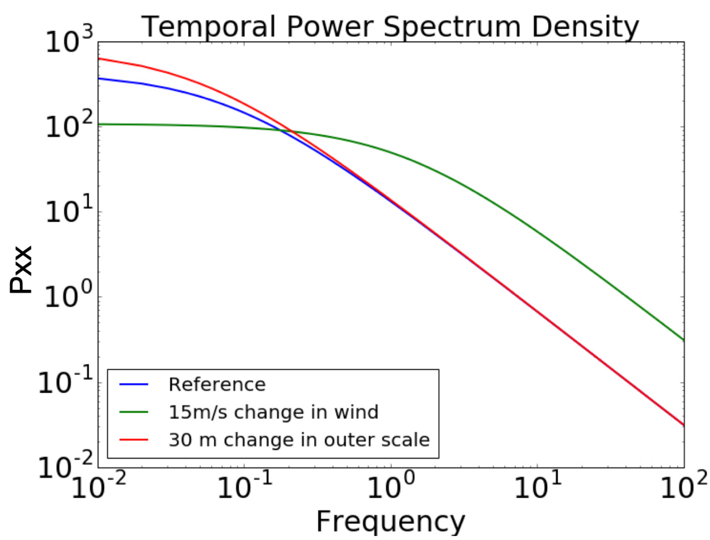

Figure 3.4: Temporal von Kárman PSD for three different cases: a reference PSD, a change in wind speed by 15 m/s, and finally a change in 30 metres for L_0.

varies from day time to night time — many wind PSDs are for day time only. Observations of wind (minute time scales) in flat agricultural areas (at the CESAR observatory in the Netherlands) show very different variations (in amplitude and in mean wind speed) from data at Mauna Kea or Paranal with the same sampling. There are also added effects such as dome geometry and the telescope movement that contribute to the relative v seen by the AO system that are not described by these PSDs and data. Finally, the variation in wind direction also needs to be considered.

Due to the lack of data and wind models that accurately describe the wind at an observatory, we assume a worst case scenario — wind gusts combined with turbulent induced fluctuations. We use the Kaimal PSD (Pablo et al., 2004) to generate the small wind fluctuations caused by turbulence and assume the atmosphere is stationary for one second (see Deodatis et al., 2014). We then change the mean wind speed using a probability density function determined by MacMynowski et al. (2006) and generate another time series of one second. In the end, we have a time series that resembles wind gusts with some fast fluctuations on top. Although this does not accurately represent the true v fluctuations, we are subjecting the predictor to small variations and large variations in one time step as well as using v that are commonly seen at observatories.

3.3.3 Effect on prediction and control

To understand how v, L_0, and r_0 affect the disturbance model and the ability of the system to reject the disturbance, we look at the spatial and temporal von Kárman PSDs. We define the spatial PSD, for a single point and a single layer, in Equation 3.10 (neglecting the inner scale).

$$\Phi(k) = 0.0229 r_0^{-5/3} (k^2 + 4\pi^2 {L_0}^2)^{-11/6} \tag{3.10}$$

For discussion purposes, we write the single-sided temporal PSD (Harrington and Welsh, 1994) (Equation 3.11), substituting in $C_n^2 dh \propto r_0^{-5/3}$ to give:

$$\Phi(f) \propto \left(\frac{v}{r_0}\right)^{5/3} \left(f^2 + \frac{v^2}{L_0^2}\right)^{-4/3} \tag{3.11}$$

Note, Equation 3.11 is slightly different from the temporal PSD used in our simulations, although we too use Frozen Flow to evolve our phase screens.

Equations 3.10 and 3.11 show that when r_0 varies, both the spatial and temporal gains are changed. L_0 also affects the spatial PSD gain, as well as the cut-off frequency of the temporal PSD. Variations in v change the gain and cut-off frequency of the temporal PSD (i.e, Figure 3.4). An ideal predictor should be able to account for the variations in the cut-off frequency that are due to the changing disturbance's statistics. Time-invariant predictors are based on stationary disturbance statistics. Therefore, knowledge of the dynamical behavior of v and L_0 might be beneficial to achieve the AO system best reject the turbulence phase fluctuations, as well as understand the penalties of using a stationarity based predictor under non-stationary conditions.

3.4 Simulations

We test the three different LMMSE predictors outlined in Section 3.2 along with a perfect integrator (zero-order predictor/no prediction) analogue in an open-loop configuration. To do this, we take the most recent open-loop measurement as the best estimate for the current phase aberrations; the gain is 1 as we do not have to worry about any response of the AO system. We simulate, in Python, an 11-by-11 Shack-Hartmann wavefront sensor (SHWFS), adding measurement noise to the phase disturbance. We then feed the resulting phase screen (representing the atmosphere at time t) into our predictors and apply the predicted correction (predicted wavefront to time $t+1$) to a deformable mirror with 97 actuators (DM97). We track the residuals to determine the performance of the predictors. We do this for various input disturbances including:

1. stationary turbulence,
2. non-stationary turbulence with varying r_0 (two different cases),
3. and on-stationary turbulence with varying v.

The exact configurations of the input parameters for each case are summarized in Table 3.1. We run our AO loop at 500 Hz for 5 seconds, then average the root-mean-square (rms) error over 50 runs, regenerating the phase screens with the same PSD. We set $L_0 = 30\ m$.

3.4.1 Results and Discussion

Stationary turbulence

We initially test the stationary turbulence model with the atmospheric parameters in Table 3.1 (Case 1). From Figure 3.5, we can see that the LMMSE predictor performs better than the integrator (no prediction) as expected, with the LMMSE having a rms of 0.41 radians (rad) and the integrator having an rms of 0.54 rad. This validates the added value of prediction. The exact difference in performance is dependent on the wind speed, the spatial resolution, and the length of the delay. We see that as the v

Table 3.1: Summary of input parameters for different simulations.

Case	Simulation	r_0 [cm]	v [m/s]
1	Stationary turbulence	13	7
2	Non-stationary turbulence: r_0 1	13.001–13.004	7
3	Non-stationary turbulence: r_0 2	5–25	7
4	Non-stationary turbulence: v	13	4–7

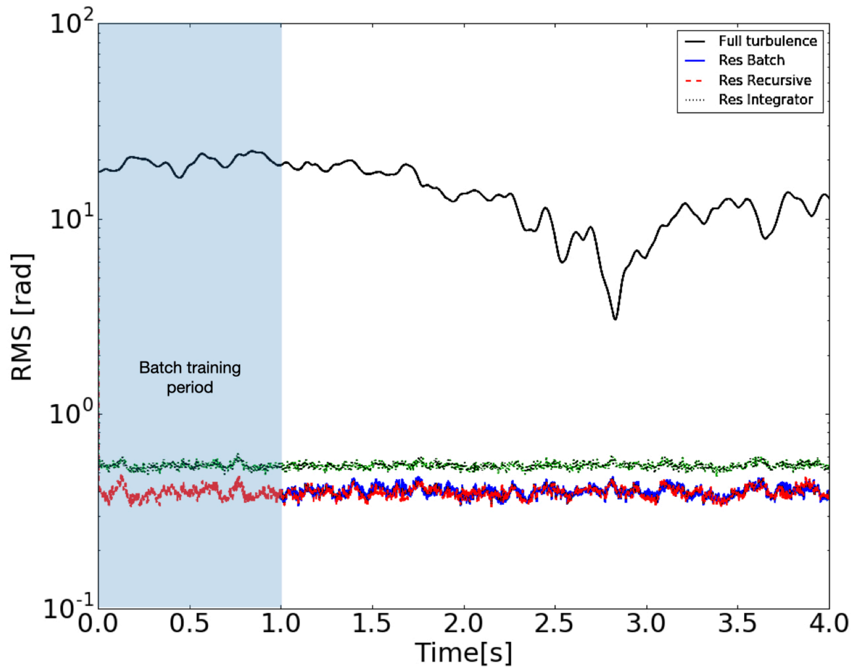

Figure 3.5: Case 1: Residuals (res) of the LMMSE predictors and the integrator compared to the full uncorrected wavefront error for stationary conditions with constant Fried parameter and wind speed. The first second is the batch training period. The recursive predictor takes tens of iterations to converge which is not visible in the plot.

reduces, the integrator and LMMSE become closer in performance (not shown). The batch and recursive LMMSE also have the same value when the batch predictor is turned on, which indicates our LMMSEs are behaving properly. Finally, as we move further away from the batch training period, the recursive solution becomes slightly better than the batch (not shown). As the recursive estimator continues to run it obtains a more accurate estimate of the covariance matrices.

Using the stationary turbulence, we looked at the prediction vector found by the LMMSE. When we limit the radius of points given to the algorithm to 2 grid points, the prediction vector easily finds the perfect predictor giving the full weighting to the correct point upstream — as expected from the Frozen Flow principle. When using more grid points for prediction, the prediction algorithm has more trouble in finding the optimal solution due to the increase of redundancy in the regressor data. Due, in part, to strong spatial correlation of phase between surrounding points. Therefore, the LMMSE is unable to distinguish an upstream phase point and finds an average solution. An increase of measurement noise is expected to alleviate this issue. Overall, this demonstrates the importance of selecting the regressor grid in relation to the amount of data required to converge.

Non-stationary turbulence

We then vary r_0 for cases 2 and 3 in Table 3.1. Figure 3.6 shows that as r_0 varies only slightly (0.03% over 5 seconds) on such short time scales the mean performance of the predictors does not change, as expected. However, such small variations in r_0 likely cannot be seen due to the injected measurement noise and the pixel scaling. Therefore, we also simulated large artificial ramps for r_0 as in case 3. In Figure 3.7, we show the results of changing r_0 by 20 centimeters, from $D/r_0 \sim 5$ to $D/r_0 \sim 1$, over a few seconds. We see a dramatic decrease in the rms for the LMMSE; the decrease is a factor of two larger than the integrator. We then study the behavior of the prediction vector in time. We plot the evolution of the prediction coefficient (one value in the prediction vector) for a few different phase points in Figure 3.8. We see that the prediction coefficients remain constant in time with slight fluctuations. Therefore, the recursive LMMSE solution is not affected by the change in r_0. The decrease in rms followed by the increase in rms seen in Figure 3.7 is due to the overall decrease in variance of the phase screen as the coherence length increases, making the phase screens more uniform. Ultimately, the Fried parameter simulations show that the regular fluctuations of r_0 do not change the performance, and that, on time scales of a few seconds, when we vary r_0 slowly the disturbance rejection remains unchanged.

We vary v according to section 3.3.2 and present the results for our case 4. In Figure 3.9, we see that wind jumps of 1 m/s can degrade the performance of the integrator and the batch and recursive LMMSE. The batch method, as expected, does not update the predictor solution once set and therefore does not see the changing statistics. The recursive LMMSE is also unable to track the step in wind speed, even though the predictor is updated at each time step. In Figure 3.9, the rms wavefront error for all the predictors increases by a factor of two, at the second wind jump.

The tracking speed of the recursive approach is dependent on how long the pre-

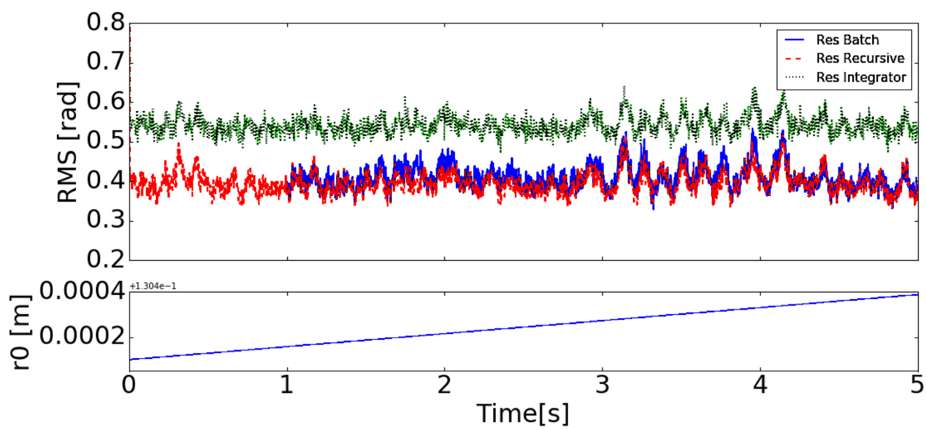

Figure 3.6: Case 2: r_0 varying according to an fractional ARIMA model Doelman and Osborn (2016).

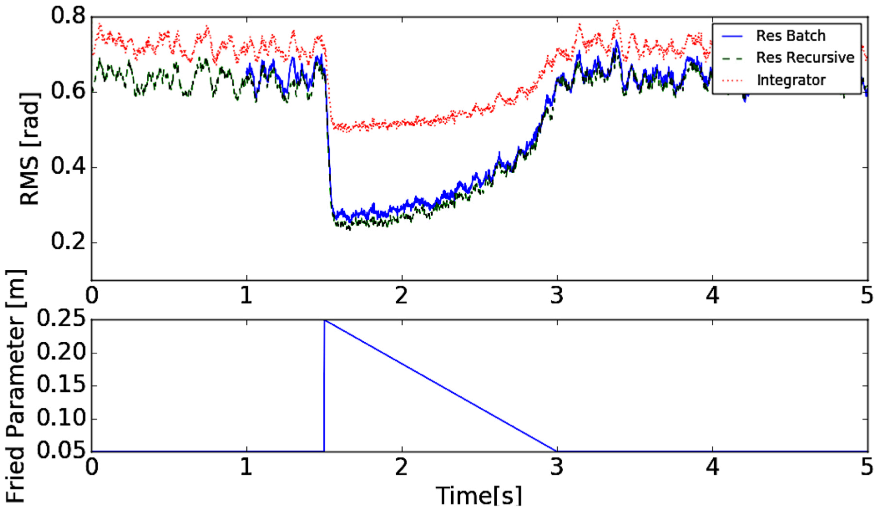

Figure 3.7: Case 3: r_0 exaggerated as a ramp feature.

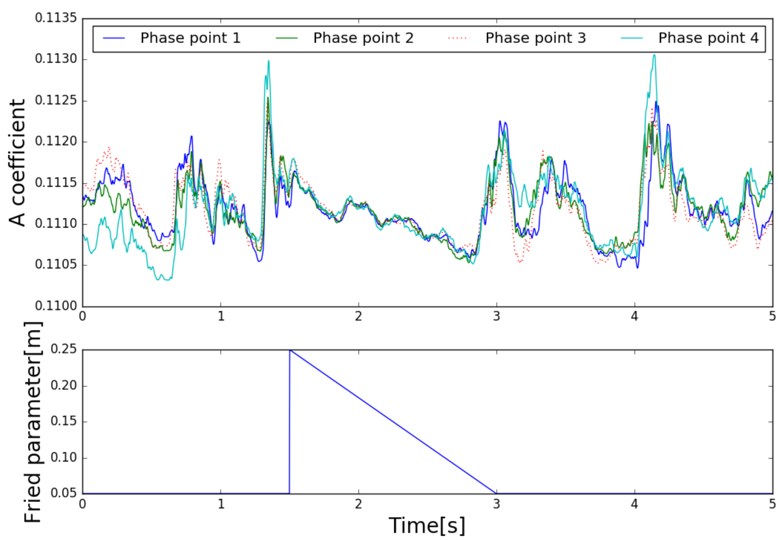

Figure 3.8: The evolution of a prediction coefficient for 4 different phase points as the r_0 varies.

diction has been running; it has 'unlimited' memory and variations in the statistics are averaged into the estimator. Inserting an exponential forgetting factor in the covariance estimation of the recursive LMMSE, we form an adaptive LMMSE. We can see a very slight difference in the performance between the pure recursive and the forgetting factor recursive method (we tested forgetting factor values from 0.99-0.90 with no notable differences; values smaller than this cause numerical instabilities). However, we need more tests to quantify the added value of exponential forgetting.

3.5 Conclusions

We show that a predictor's ability to remove residual phase errors due to the inherent time delay in an AO system depends on the statistical behavior of the wavefront disturbance. We focus on understanding how the non-stationary behavior atmospheric turbulence, specifically with respect to v and r_0, might affect our predictors. We have described a method that can be used to model these non-stationarities and that the change in r_0 can be modelled following Doelman and Osborn (2016). We show that using this model, the variations in r_0 over short time scales do not change the performance of the integrator and LMMSE predictors. Inserting wind gusts into the simulation, we see that the integrator and the LMMSE predictors are less efficient at rejecting the atmospheric turbulence resulting in a factor of two increase in the rms wavefront error. Determining a realistic model of wind speed fluctuations is a crucial next step in testing and developing predictive control algorithms as it can have a large effect on the AO performance.

We are currently focusing on developing a dynamical model to represent how wind might behave above an observatory. This will be used to further test our LMMSE predictor. With this model we will also study how contrast might be affected in simulation when comparing stationary and non-stationary atmospheric induced phase fluctuations.

References

Assémat, François, Richard W. Wilson, and Eric Gendron (Feb. 2006). "Method for simulating infinitely long and non stationary phase screens with optimized memory storage". In: *Opt. Express* 14.3, pp. 988–999.

Beuzit, Jean-Luc et al. (2008). "SPHERE: a planet finder instrument for the VLT". In: *Proc.SPIE* 7014, pp. 7014 - 7014 –12.

Correia, C. M., K. Jackson, J.-P. Véran, D. Andersen, O. Lardière, and C. Bradley (June 2015). "Spatio-angular minimum-variance tomographic controller for multi-object adaptive-optics systems". In: *OSA* 54, p. 5281.

Deodatis, G., B.R. Ellingwood, and D.M. Frangopol (2014). *Safety, Reliability, Risk and Life-Cycle Performance of Structures and Infrastructures*. CRC Press.

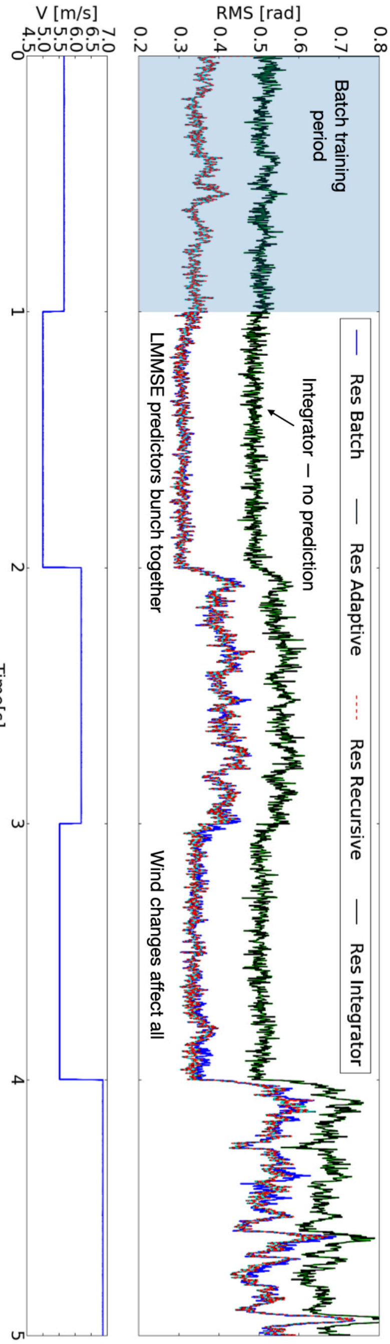

Figure 3.9: Performance of the predictors for varying wind parameters.

Doelman, N., R. Fraanje, and R. den Breeje (2011). "Real-sky adaptive optics experiments on optimal control of tip-tilt modes". In: *2nd Conference on Adaptive Optics for Extremely Large Telescopes* 1.1.

Doelman, Niek J., Karel J. G. Hinnen, Freek J. G. Stoffelen, and Michel H.G. Verhaegen (2004). "Optimal control strategy to reduce the temporal wavefront error in AO systems". In: *Proc.SPIE* 5490, pp. 5490 - 5490 –12.

Doelman, Niek, Rufus Fraanje, Ivo Houtzager, and Michel Verhaegen (2009). "Adaptive and Real-time Optimal Control for Adaptive Optics Systems". In: *European Journal of Control* 15.3, pp. 480–488.

Doelman, Niek and James Osborn (2016). "Modelling and prediction of non-stationary optical turbulence behaviour". In: *Proc.SPIE* 9909, pp. 9909 - 9909 –8.

Gray, M., C. Petit, S. Rodionov, M. Bocquet, L. Bertino, M. Ferrari, and T. Fusco (Aug. 2014). "Local ensemble transform Kalman filter, a fast non-stationary control law for adaptive optics on ELTs: theoretical aspects and first simulation results". In: *Optics Express* 22, p. 20894.

Hardy, J. W. (1998). "Adaptive Optics for Astronomical Telescopes". In: *Oxford University Press Jul 1998*.

Harrington, Patrick M. and Byron M. Welsh (1994). "Frequency-domain analysis of an adaptive optical system's temporal response". In: *Optical Engineering* 33.7, pp. 2336–2342.

Hinnen, Karel, Michel Verhaegen, and Niek Doelman (June 2007). "Exploiting the spatiotemporal correlation in adaptive optics using data-driven H2-optimal control". In: *J. Opt. Soc. Am. A* 24.6, pp. 1714–1725.

Jovanovic, N. et al. (Sept. 2015). "The Subaru Coronagraphic Extreme Adaptive Optics System: Enabling High-Contrast Imaging on Solar-System Scales". In: *Publications of the Astronomical Society of the Pacific* 127, p. 890.

Kasper, Markus (2012). "Adaptive optics for high contrast imaging". In: *Proc.SPIE* 8447, pp. 8447 - 8447 –10.

Kooten, Maaike van, Niek Doelman, and Matthew Kenworthy (2017). "Performance of AO predictive control in the presence of non-stationary turbulence". In: Instituto de Astrofisica de Canarias.

Le Roux, B., R. Ragazzoni, C. Arcidiacono, J.-M. Conan, C. Kulcsar, and H.-F. Raynaud (Oct. 2004). "Kalman-filter-based optimal control law for star-oriented and layer-oriented multiconjugate adaptive optics". In: *Proc.SPIE* 5490, pp. 1336–1346.

Looze, Douglas P. (Jan. 2009). "Linear-quadratic-Gaussian control for adaptive optics systems using a hybrid model". In: *J. Opt. Soc. Am. A* 26.1, pp. 1–9.

Macintosh, Bruce et al. (2014). "First light of the Gemini Planet Imager". In: 111.35, pp. 12661–12666.

MacMynowski, Douglas G., Carl Blaurock, George Z. Angeli, and Konstantinos Vogiatzis (2006). "Modeling wind-buffeting of the Thirty Meter Telescope". In: *Proc.SPIE* 6271, pp. 6271 - 6271 –12.

Marois, C., B. Macintosh, T. Barman, B. Zuckerman, I. Song, J. Patience, D. Lafreniere, and R. Doyon (2008). "Direct Imaging of Multiple Planets Orbiting the Star HR 8799". In: 322.5906, pp. 1348–1352.

Massioni, P., C. Kulcsár, H.-F. Raynaud, and J.-M. Conan (Nov. 2011). "Fast computation of an optimal controller for large-scale adaptive optics". In: *Journal of the Optical Society of America A* 28, p. 2298.

Otten, G. P. P. L. et al. (Jan. 2017). "On-sky Performance Analysis of the Vector Apodizing Phase Plate Coronagraph on MagAO/Clio2". In: *The Astrophysical Journal* 834, p. 175.

Pablo, Juan, Pérez Beaupuits, Angel Otárola, Fredrik T. Rantakyrö, Roberto C. Rivera, Simon J, E. Radford, and Larsaake Nyman (2004). "ANALYSIS OF WIND DATA GATHERED AT CHAJNANTOR". In: *ALMA Memo* 497.

Paschall, R. N. and D. J. Anderson (Nov. 1993). "Linear quadratic Gaussian control of a deformable mirror adaptive optics system with time-delayed measurements". In: *OSA* 32, pp. 6347–6358.

Petit, C., J.-M. Conan, C. Kulcsár, and H.-F. Raynaud (May 2009). "Linear quadratic Gaussian control for adaptive optics and multiconjugate adaptive optics: experimental and numerical analysis". In: *Journal of the Optical Society of America A* 26, p. 1307.

Petit, C., J.-M. Conan, C. Kulcsár, H.-F. Raynaud, and T. Fusco (2008). "First laboratory validation of vibration filtering with LQG control law for Adaptive Optics". In: *Optics Express* 16, p. 87.

Poyneer, L. A. et al. (Jan. 2016). "Performance of the Gemini Planet Imager's adaptive optics system". In: *OSA* 55, p. 323.

van der Hoven, I. (Apr. 1957). "Power Spectrum of Horizontal Wind Speed in the Frequency Range from 0.0007 to 900 Cycles Per Hour." In: *Journal of Atmospheric Sciences* 14, pp. 160–164.

Chapter 4

Implications for contrast as a result of the wind vector and non-stationary turbulence

> "It's the job that's never started as takes longest to finish"
>
> J.R.R., *The Fellowship of the Ring*

Summary

In an adaptive optics (AO) system, finite time delays contribute a relatively large amount to the overall wavefront error. The temporal error, due to time delays, adds to the speckle halo which is visible in the science plane of a high-contrast imaging (HCI) instrument. The halo limits the achievable contrast near the inner working angle, preventing HCI from probing regions where we expect Earth-like planets. Our research focuses on understanding the non-stationary behavior of atmospheric turbulence and its effects on the temporal error and the contrast.

The wind vector greatly influences the turbulence-induced wavefront phase error. In the framework of the von Karman power spectral density (PSD) of wavefront phase, the wind speed changes the cut-off frequency as well as the gain of the temporal PSD. We aim to understand the behavior of the wind vector on sub-second timescales using data from the Thirty Meter Telescope site testing campaign at Mauna Kea. The nocturnal measurements we study are from 287 nights throughout the years of 2006-2008, taken at a height of 7 m with a maximum sampling rate of 60 Hz. We present an estimated PSD from the observed data to describe the wind speed located at Area E (northern plateau) on Mauna Kea. We compare the estimated PSD to the Kaimal PSD—a parameterised wind model for the lower atmospheric boundary layer. Studying the estimated PSD, we fit a fractionally integrated auto-regressive–moving-average model to the data. With this model we can create an artificial wind speed time series to be fed into phase screen simulations to generate realistic wind-varying phase screens. We examine how the contrast, achieved by

This chapter is published as: Maaike van Kooten et al. (2018). "Implications for contrast as a result of the wind vector and non-stationary turbulence". In: *Adaptive Optics Systems VI*. vol. 10703. International Society for Optics and Photonics, p. 107032C

the AO system, changes when subject to non-stationary turbulence induced by wind fluctuations for an integrator controller.

4.1 Introduction

In ground-based high-contrast imaging (HCI), current contrast levels — especially close into the host star — are limited by the performance of the adaptive optics (AO) system (Kasper, 2012). Specifically, by the finite time delay in the control loop, leading to the servo-lag error, that results in the so-called wind-driven halo seen by instruments such as SPHERE (Milli et al., 2017). Even after post-processing techniques such as angular differential imaging (ADI), the wind driven halo is still present as described by Milli et al. (2017). Efforts to improve control techniques to minimize the servo-lag error, and thereby the wind-driven halo, are on-going (Paschall and Anderson, 1993; Le Roux et al., 2004; Looze, 2009; Gray et al., 2014; Massioni et al., 2011; Correia et al., 2015; Doelman, Fraanje, et al., 2009; Hinnen et al., 2007).

In designing new controllers, the question arises as to how accurately input disturbances need to be modeled. Many AO simulation tools rely on performing a discrete Fourier transform (DFT) of a power spectral density (PSD) which gives the covariance function of the phase distortion due to atmospheric turbulence. For a temporally evolving atmosphere, a large phase screen (the length of which is the telescope diameter multiplied by the number of iterations to step through) is typically generated once and then shifted at a fixed rate simulating Taylor's Frozen Flow Hypothesis (i.e, the wind blowing the turbulence across the telescope aperture). The principle can be used to generate a multi-layered atmosphere that is fitted to fixed C_n^2 and wind vector profiles. These methods provide a good basis for many AO systems and allow for relatively quick simulations that are representative of the atmosphere. However, depending on the temporal behavior of atmospheric parameters such as the outer scale, Fried parameter, and the wind vector, which we know evolve on timescales of minutes (or less; Ziad (2016)), these methods might not be adequate to simulate the performance for the next generation of large telescopes, especially for optimal performance or very high contrasts.

In this paper, we focus solely on the behavior of the wind vector and how it affects current adaptive optics systems. Within the context of HCI, we aim to understand how varying wind speed contributes to the wind-driven halo and therefore the contrast. The main objective of this paper is to answer the following question: to what extent do instantaneous wind fluctuations affect contrast? To answer this overarching question, we discuss the following questions:

1. How does wind vary during an observation?
2. How do wind fluctuations influence the contrast?

By answering these research questions, we can determine whether more efforts are needed to characterize wind at high temporal frequencies as well as use this information to dictate what control schemes could be used in place of an integrator to minimize the wind-driven halo.

4.1.1 Servo-lag error and wavefront sensor integration

To answer the question of how wind fluctuations affect the AO system, we can look at how wind speed affects the AO system by relying on the Frozen Flow hypothesis. In Hardy (1998), the servo-lag error is expressed as $\alpha^2_{servo} = (\frac{T_{control}}{\tau_0})^{5/3}$, with $T_{control}$ being the closed-loop control time and τ_0 being the time constant (which depends on the wind speed). Note that a large amount of the control time is the wavefront sensor (WFS) integration time. Therefore, as the wind speed increases we can keep our servo-lag error constant by decreasing the WFS integration time. However, the WFS integration time also determines the signal-to-noise ratio of the WFS and therefore the measurement error. The optimal integration time must be found by minimizing the summed error term of the servo-lag error and the measurement error.

4.1.2 Outline

The first part of the paper focuses on understanding how the wind varies on sub-second timescales and how to model these fluctuations. In Section 4.2 we present the behavior of the observed wind vector. In Section 4.3 we estimate the wind speed PSD, compare it to PSDs from literature, and determine a corresponding stochastic model of the wind speed. The second part of the paper focuses on wind fluctuations and contrast. In Section 4.4, we look at the effects of varying wind on the contrast.

4.2 Observed Wind Vector Data

4.2.1 Overview of data

The data used in this work are from the Thirty Meter Telescope (TMT) site testing campaign at Mauna Kea, Hawaii taken between 2006 and 2008 by Schock et al. (2009). The data consist of raw sonic anemometer wind speed values taken at 7 m height, with a maximum sampling rate of 60 Hz. The wind speed is measured in three directions with a range of ± 60 m/s for the horizontal wind directions u_x, and u_y. A total of 287 nights (after the removal of flagged data, nights that were only a few minutes, as well as nights with points outside the measurement range) with at least one hour of data remaining for analysis are used in this work. See Table 4.1 for the exact nights used for this work.

4.2.2 Wind statistics

Nightly

We take the u_x and u_y wind speed measurements to determine the horizontal wind speed and wind direction. Looking at each night in the data set, we see two different trends for the wind speed: constant mean and variance (nearly stationary) and slowly changing mean wind speed (Figure 4.1). For nearly stationary nights, the variance of the wind speed is large. For other cases, the overall change in wind speed can be

Table 4.1: Data from the site testing group at TMT for Hawaii (Schock et al., 2009) having at least one hour of valid wind data.

Year	Month	Day	Total Nights
2006	July	18-27	10
	August	10-12	3
	October	23-31	7
	November	1,3-11,13,15-29	25
	December	1-13	13
2007	May	11-28,30-31	20
	June	1-8,10,12-30	28
	July	1-19,21-31	30
	August	1,3-13,16-31	28
	September	1-17,18-30	29
	October	1-2,4-6,8-14,17-20,24,26,28-31	21
	November	2-3,5-6,9-20,22,24,27	17
2008	March	22-24,29-31	6
	April	1-6,10-17,21-24,26-28	21
	May	1,3-5,7-21,23-31	27
	June	1	1

large for a night. The variance of the wind speed is, however, small for short time frames.

We also observe two different trends in wind direction: very constant wind direction or random fluctuations. These random fluctuations occur for slower wind speeds, though are still pronounced even when wind speeds less than 1 m/s are filtered out (therefore it is not a consequence of reduced certainty at low wind speeds). From Mahrt (2011), we expect these wind direction fluctuations at lower wind speeds during the night, although what causes them is not fully understood within the field of atmospheric boundary layer science. The large fluctuations seen at slow wind speeds only occur a few nights out of the data set and are not representative of behavior of the wind vector.

Long term statistics

Figure 4.2 shows a histogram (for the entire data set) of mean wind speed per night. Further analysis shows that the mean wind speed does not vary much on a month to month basis. The entire data set has a mean wind speed of 6.55 m/s. This mean value is in good agreement with the value of 5.70 m/s published by Schock et al. (2009), with differences in the inclusion/exclusion of data leading to our value.

The wind direction is more variable on monthly timescales. Although the dominant direction for higher wind speeds is from the east, on a monthly basis we see other wind directions that dominate at lower wind speeds (Figure 4.4).

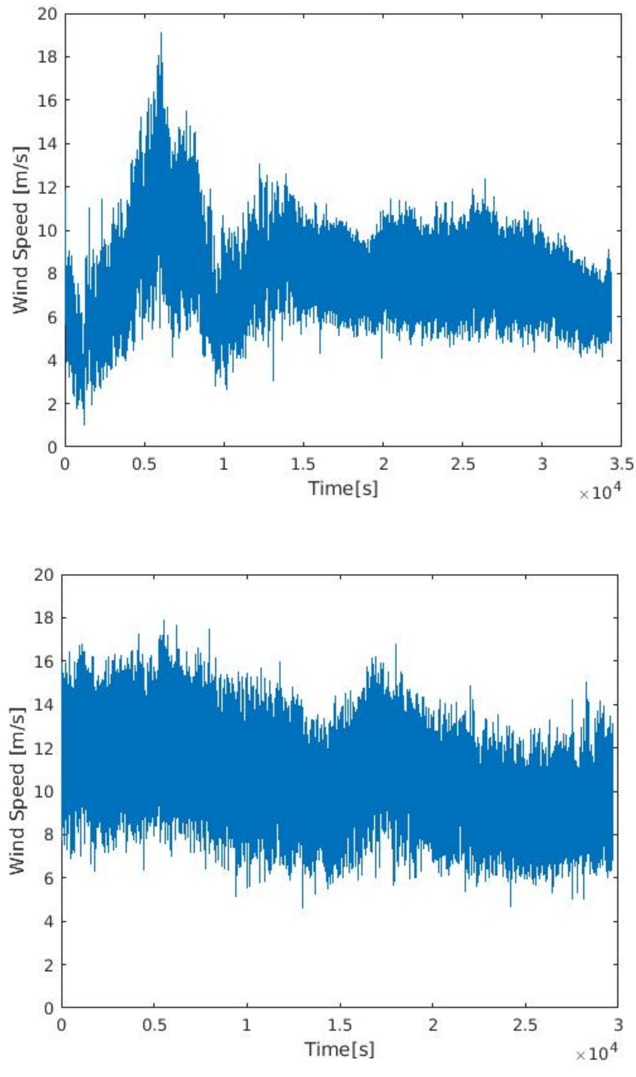

Figure 4.1: Wind speed for the entire nights of 11-07-2007 (top) and 31-03-2008 (bottom).

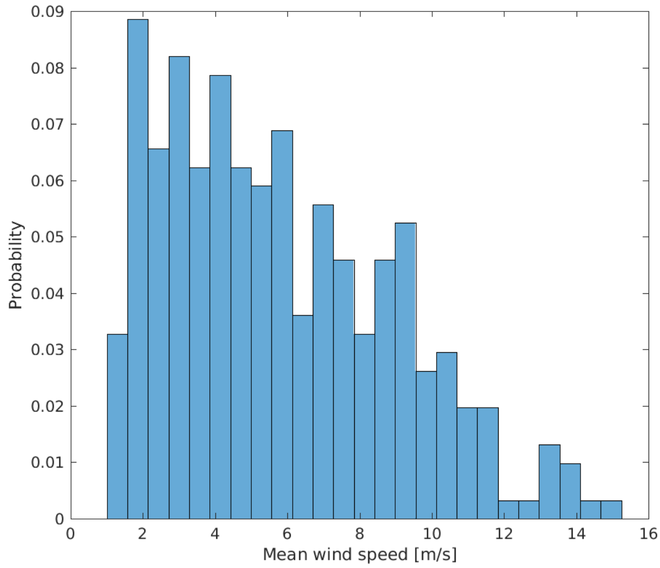

Figure 4.2: Histogram of mean wind speed per night for the entire data set.

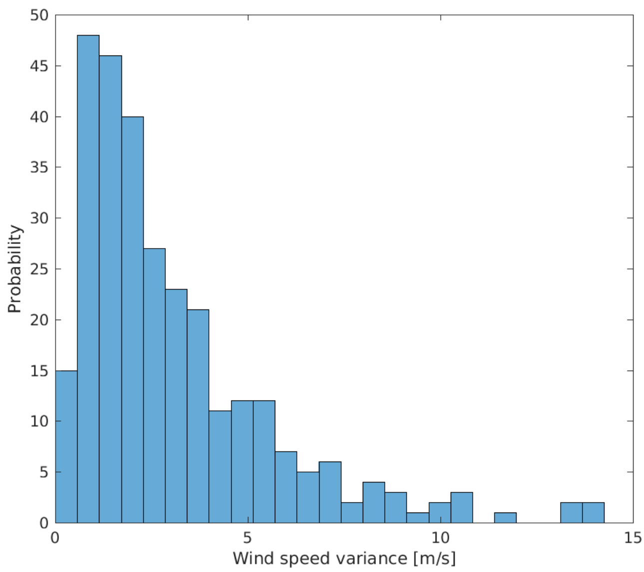

Figure 4.3: Histogram of the nightly wind speed variance over the entire data set.

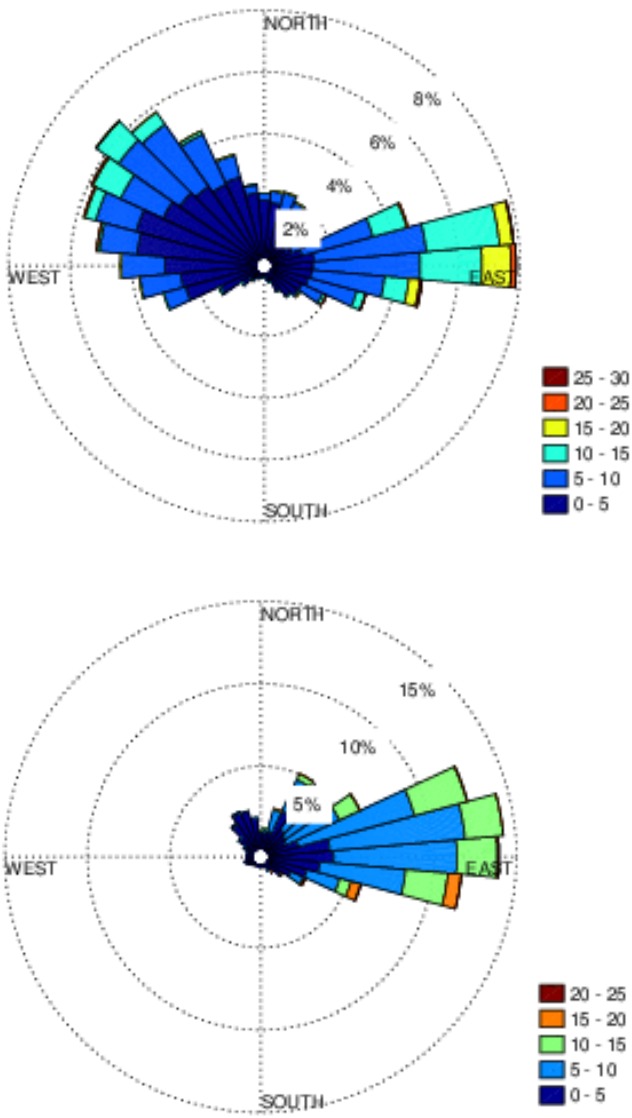

Figure 4.4: Wind direction during the months of 12-2006 (top) and 07-2007 (bottom). The colors indicate the wind speed in m/s

We make no further attempt to distinguish any long-term behavior or seasonal behavior of the wind vector due to the relatively limited size of our data set on such timescales.

4.3 Estimation of Wind Speed Power Spectral Density

We estimate the PSD of the wind speed using the three years of data summarised in Table 4.1. First, we estimate the PSD for each night by splitting the data into a time series of 3000 points. The time series are detrended and the mean is subtracted. We then estimate the PSD using the Lomb-Scargle periodogram method, which allows for non-uniformly sampled data. All estimated PSDs are then averaged together for one given night. We then average the PSDs of all nights to generate our final PSD (Figure 4.5). We limit our PSD estimation to frequencies less than 10 Hz to avoid the peak at 20 Hz due to artifacts from the instrument itself.

In logarithmic space, the PSD shown in Figure 4.5 falls-off approximately linearly after the cut-off frequency of 0.03 Hz. There is also a slight inflection at higher frequencies (above 2 Hz). The shape is consistent with energy/turbulent production at low frequencies injecting power which peaks and then falls off in the inertial subrange, eventually dissipating at higher frequencies (Pablo et al., 2004). We fit a power law to the inertial subrange, finding a slope of -1.53.

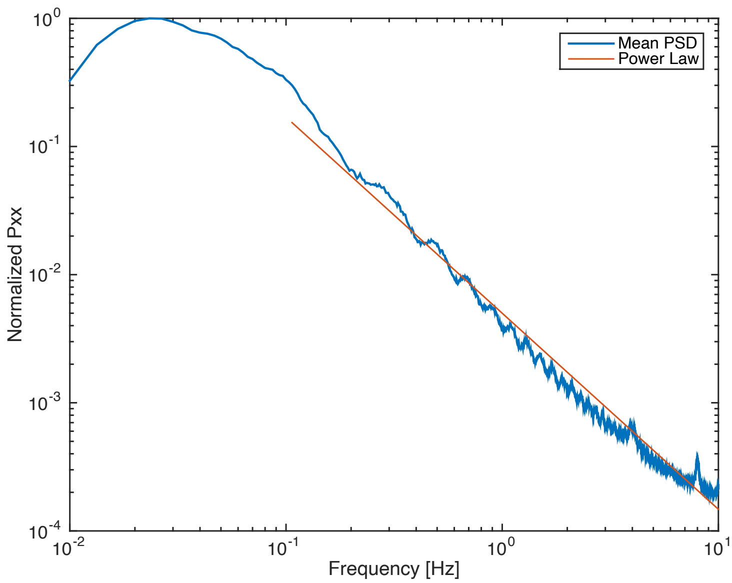

Figure 4.5: Estimated wind speed PSD for the 287 nights of data.

4.3.1 Comparison to other wind speed PSD models

Models in the literature for the PSD of wind speed are based on the following form:

$$nS(n)/\mu_f^2 = \frac{a}{(1+bf)^c} \tag{4.1}$$

with a, b, and c being real-valued coefficients, n being normalized frequency and $S(n)$ being the PSD.

It has been shown that for minute to second timescales the slope of the wind speed PSD is dependent on geographical features (Hiriart et al., 2001). Therefore we compare our normalized PSD to three variations, the Davenport, a modified Kaimal, and best-fit by Pablo et al. (2004) (we will refer to this model as A&A from now on). In Figure 4.6 we see that the overall shape and slope of the different distributions are similar to our estimated PSD. It is important to note that the Davenport, Kaimal, and A&A curves depend on the friction velocity, μ_f, due to the amount of shearing that occurs in the boundary layer (atmospheric boundary layer is defined as the first few hundred meters depending on location and time). This is not necessarily applicable to the wind measurements taken at Mauna Kea at an altitude of 4 km .

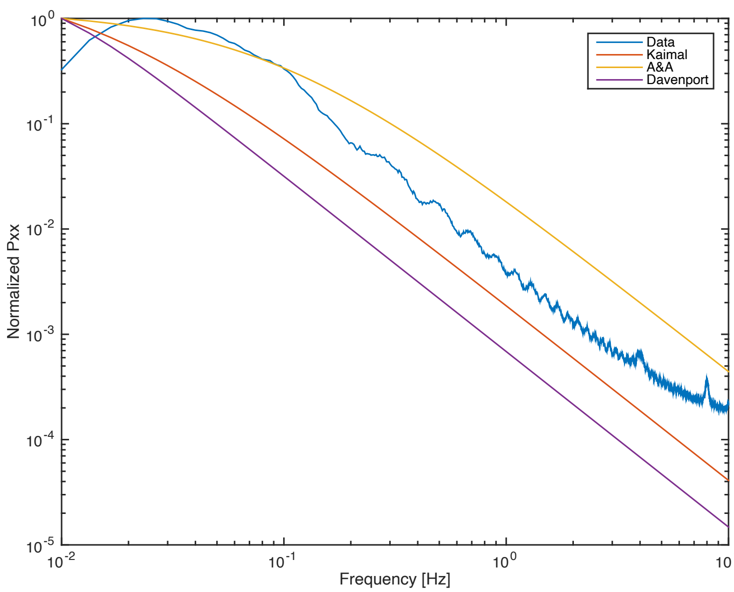

Figure 4.6: Estimated PSD compared to the Davenport, modified Kaimal, and A&A best-fit (Hiriart et al., 2001).

4.3.2 Stochastic Model for wind speed

One of the goals of this paper is to determine a dynamic model to allow for the modeling of realistic wind variations for a variety of simulation lengths. We therefore focus on matching a model to the observed PSD for the full frequency range between 0.002 Hz and 10 Hz. To match the behavior described above, as well as ensure the model does not have a large number of coefficients, we look toward fitting an auto regressive fractionally integrated moving average stochastic model (i.e., an ARFIMA) as done by Doelman and Osborn (2016) for the Fried parameter. Noticing that our PSD differs at low frequencies, we expand the model to capture the cut-off, we further use a low order auto regressive tempered fractionally integrated moving average stochastic model (an ARTFIMA) as described by Sabzikar et al. (2015).

The PSD of an ARTFIMA(p,λ,f,q) is given by

$$\Phi(k) = \frac{|\Theta(e^{-ik})|^2}{|\Phi(e^{-ik})|^2} |(1 - e^{-\lambda - ik})|^{-2d} \tag{4.2}$$

with $\Theta(z) = 1 + \theta_1 z + ... + \theta_q z^q$ and $\Phi(z) = 1 - \phi_1 z - ... - \phi_p z^p$ being the MA and AR parts of the model, respectively and k is the spatial frequency.

We find a lower order ARTFIMA(0,λ,f,0), Equation 4.3, to be a good fit to our data (R-squared = 0.999) for frequencies higher than 0.05 Hz, as shown in Figure 4.7. Using this model, together with the histogram of wind speed variance per night (Figure 4.3), and the histogram of mean wind speed per night (Figure 4.2), we can simulate a variety of realistic wind conditions.

$$\Phi(k) = |(1 - e^{0.02 - ik})|^{-2(0.91)} \tag{4.3}$$

Ongoing research is being conducted to further improve the fit and capture the correct behavior of the estimated PSD at the low frequencies, and not just the slope for higher frequencies.

4.3.3 Implementation

Using the stochastic model above along with the histogram of the nightly wind speed variances, we have presented a framework to allow for the modeling of wind speed fluctuations at the ground layer. By combining this model with turbulent phase generation environments such as the infinitely long and non-stationary phase screen method by Assémat et al. (2006) or the autoregressive method by Srinath et al. (2015), we can generate non-stationary phase screens. Furthermore, we can expand our non-stationary turbulence model to include Fried parameter fluctuations as found by Doelman and Osborn (2016) and test a variety of AO configurations.

Although we briefly investigate the behavior of wind direction fluctuations in Section 4.2, we do not attempt to model or determine the PSD of the wind direction fluctuations as the focus of the remainder of this paper is on contrast and wind speed in the framework of an AO system using an integral controller. We assume that the

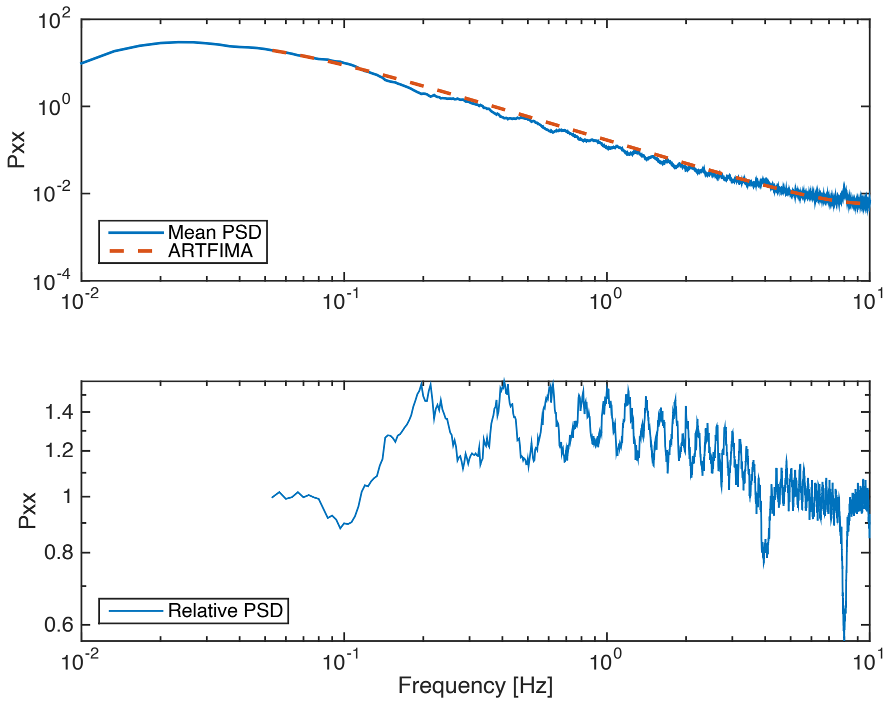

Figure 4.7: Top panel shows the ARTFIMA fit to the estimated PSD. The relative PSD (the estimated PSD multiplied by the inverse of the fitted PSD) showing the error between the fitted ARTFIMA model and the estimated PSD from the data is shown in the bottom panel.

wind direction would not be a large factor in the behavior of the system due to the small nature of the wind fluctuations.

4.4 Implication of wind speed PSD on contrast

4.4.1 Simulation environment

To investigate the influence of variable wind speed on the contrast of an HCI system, we first simulate the residual wavefront error from an AO system and then propagate the phase error through a perfect coronagraph after which we can calculate the raw contrast (Jensen-Clem et al., 2018) from the coronagraphic point-spread-function (psf) using:

$$C_{raw} = \frac{mean[R(x,y)]}{max[PSF_{star}(x,y)]} \tag{4.4}$$

with R(x,y) being the intensity in a region of interest. We focus on the behavior of a classical AO system assuming a single deformable mirror and a Shack-Hartmann WFS using a 4-quadrant detector centroiding algorithm. The controller is an integrator in which the current phase detected by the WFS is taken as the best representation of the wavefront to be corrected. Instead of performing an end-to-end simulation, as we only want residual wavefront errors for a variety of wind speeds, we use the analytical based AO toolbox, PAOLA, written in IDL (Jolissaint et al., 2006). The code uses a PSD-based approach in which the whole system is modeled together using an analytical expression for the residual phase PSD. The code allows for the user to define a deformable mirror (idealized, laboratory measured transfer function, or user defined). It also allows for the implementation of many pupil geometries. Finally, it allows for a ground layer natural guide star AO mode, which is used for this work.

Our WFS is sensing in the R-band and the natural guide star magnitude $m_r = 10$. The computational time is set to 7.5 ms; in this way to ensure the servo-lag error is the largest contributor to the residual wavefront error (overall latency including the WFS integration time). The deformable mirror was chosen such that the actuator grid samples the Fried parameter 4 times, guaranteeing a low fitting error. See Table 4.2 for list of input parameters in our simulation. Table 4.3 shows the residual root-mean-square (RMS) wavefront error where we can clearly see that the servo-lag and WFS noise are the largest contributions to the error budget.

We take the residual PSD found by PAOLA and create a phase screen which is propagated through a perfect coronagraph. We then propagate the wavefront to an image plane and determine the coronagraphic psf. We do this for many realizations and sum all the coronagraphic images to generate a long-term exposure image. We calculate the raw contrast according to Equation 4.4, the coronagraphic image is divided by the maximum of the summed non-coronagraphic images (determined by including the phase aberrations to take into account the Strehl ratio of the AO system). We average the contrast over an 8 x 8 λ/D region of interest. We find for a perfectly flat wavefront (no aberrations) our coronagraph has a contrast of 10^{-24}, showing that our coronagraph is indeed perfect given our numerical accuracy.

Table 4.2: PAOLA input parameters for natural guide star ground layer adaptive optics.

Parameter	Value
Telescope Diameter	8 m
Fried parameter @ 500nm	0.144 m
Outer Scale	30 m
Wavelength band WFS NGS	R
Control system time lag	7.5 ms
WFS integration time	3-4 ms

To simulate a long-term exposure during a period with a given time series of wind fluctuations, we first take our wind fluctuations and generate a histogram to determine the probability of each of the wind speeds. We determine the optimized gain and WFS integration time (an iterative analytic process done by PAOLA to minimize the measurement error and servo-lag error) for a given reference AO system with a specific reference wind speed. We then determine the residual PSD for each of the wind speeds in our histogram using the WFS integration time and gain determined for the reference wind speed. Finally, we take all the residual PSDs and generate many random phase screens and perform a weighted sum of images of which we can determine the raw contrast.

4.4.2 Simulations

We focus on the wind behavior of two nights, 11 July 2007 and 31 March 2008 (Figure 4.1). Taking the first 10 minutes of the time series, we find an average wind speed of 8.03 m/s and 12.25 m/s for the two nights, respectively. We use this information to calibrate our AO system, and thereby fix the controller gain and WFS integration time.

Table 4.3: Error budget for the mean wind speed of entire dataset 6.55 m/s

Error source	RMS of residual wavefront
Fitting	28.180 nm
Aliasing	2.676 nm
Servo-lag	68.454 nm
WFS noise	59.426 nm
Total	94.967 nm

For each of the nights we take two different 2.5 second segments of the wind speed fluctuations: one with a mean wind speed close to the beginning of the night, and one with a mean wind speed much larger. Examples are shown in Figure 4.8. We run the AO system for each wind speed in the time series with the reference AO

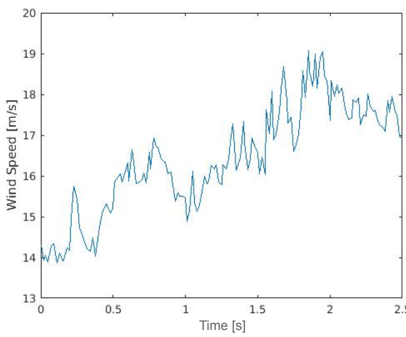

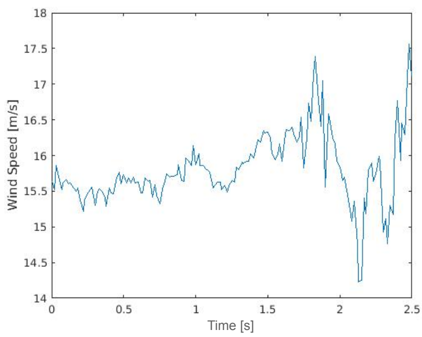

Figure 4.8: Wind speed during the nights of 2.5 seconds taken from 11-07-2007 (left) and 31-03-2008 (right).

setup and find the short-term exposure. We stack all the short term exposures to form a the long term exposure. This generates a science image that was taken with a fix AO gain while the wind speed was fluctuating as in Figure 4.8. We determine the contrast from long term exposure and compare it to the reference contrast found for the beginning of the night in when we assume the wind had not been fluctuating. Figures 4.9 and 4.10 show the results. We then repeat the simulations but set-up the AO system parameters to be optimal for the mean wind speed of the entire data set, 6.55m/s. Finally, we reference the high wind speed simulations to their mean wind speed values.

4.4.3 Simulation results

The results of the simulations are summarized in Figure 4.11. The dashed black dashed line indicates the idealized dependence on $v^{2/3}$ from Guyon (2005) for the case where the servo-lag error consists only of the WFS integration time, and the controller has a unity gain. The black dots indicate the limit of our simulation by optimizing our AO system for both v_1 and v_2 (the reference wind speed and the changed wind speed, respectively). An analytical expression for this can be derived from Jolissaint et al. (2006) wavefront error expressions. Comparing the simulation limited values to the theoretical scaling, we see that the closer we optimize our AO system to the current mean wind speed (v_2/v_1 is close to 1), the closer the contrast is to the theoretical maximum (best) performance. Even when the system is optimized for a slightly higher wind speed than observed ($v_2 < v_1$), the contrast is not significantly impacted. However, when we are far away from our actual on-sky wind speed ($v_2/v_1 > 1.5$), we lose contrast dramatically; much faster than the idealized 2/3 power scaling.

The blue square points in Figure 4.11 are for simulations that have a constant (static) wind speed. The red triangles are the results from simulations with variable wind speed fluctuating about a mean speed (v_2) as shown in Figure 4.1. Overall, there is little difference between the static and fluctuating wind results. The results of both the static and varying wind simulations show contrast differences of no more than 5%, leading to the conclusion that the small fluctuations have no impact on the contrast within our simulation environment.

In order to achieve the best contrast possible for an integral controller, our AO system should be operating in the regime where the wind speed used for tuning the system is equal to the current on-sky wind speed, and therefore the wind speed needs to be tracked throughout the night, and the system re-tuned as needed. The improvement in contrast from tracking the wind speed is illustrated by the pentagons in Figure 4.11, which shows the improvement in contrast for specific 2.5 second period (test segment), on the night of 2007 as shown in Figure 4.1. We calibrated the AO system for different wind speeds. First, we tune the AO system to the overall mean wind from the three years of site testing data (6.55 m/s) and then run the AO system on the test segment, the resulting contrast is shown by point 1 in Figure 4.11. Then, the mean from the first ten minutes (point 2) of the night is used to tune the

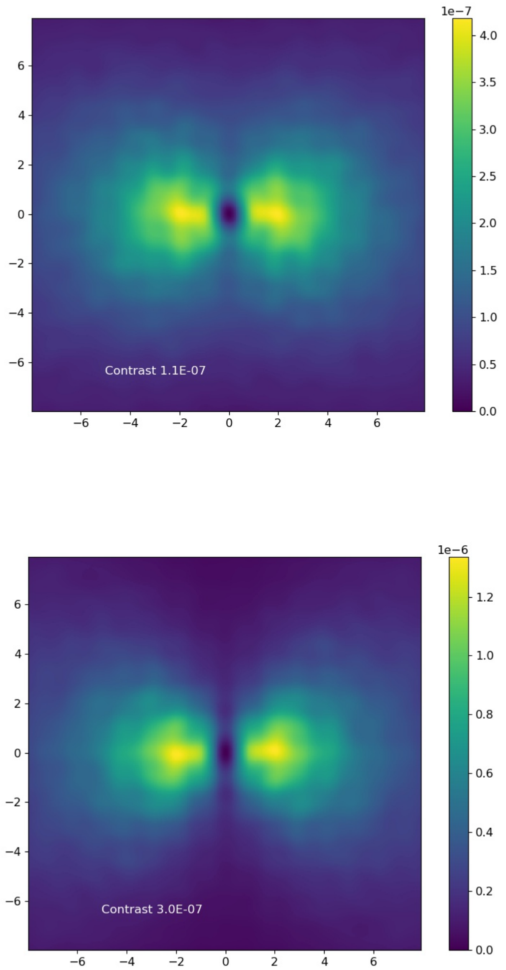

Figure 4.9: Coronagraphic images for reference wind speed of 8.03 m/s (top) and random wind fluctuations around a mean wind speed of 16.43 m/s (bottom) corresponding to the time series on the top of Figure 4.1

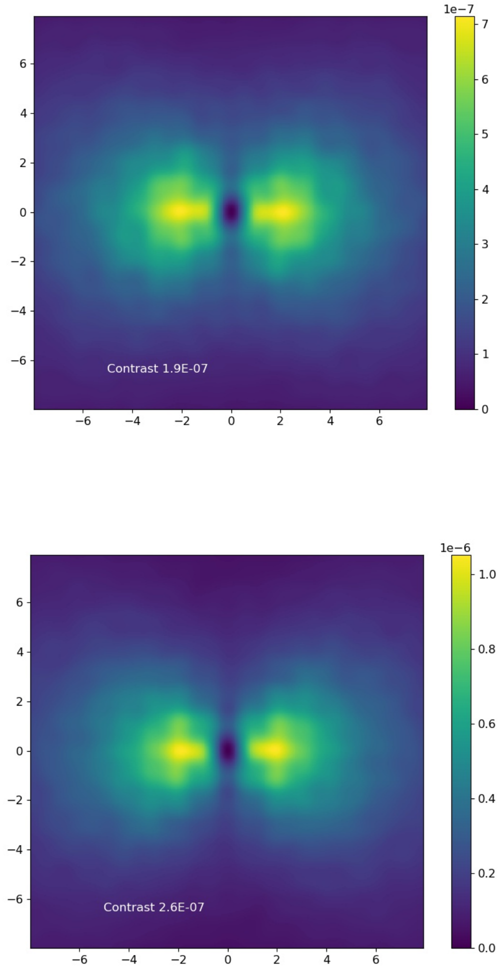

Figure 4.10: Coronagraphic images for reference wind speed of 12.25 m/s (top) and random wind fluctuations around a mean wind speed of 15.80 m/s (bottom) corresponding to the time series on the bottom of Figure 4.1.

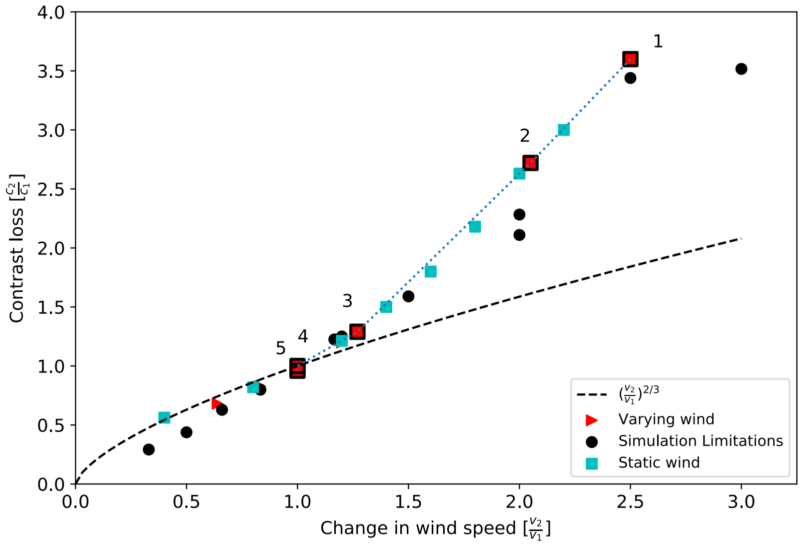

Figure 4.11: Contrast loss as a function of change in wind speed. The black dashed line indicates the theoretical limit. Various simulation runs are shown by the markers. The blue dashed line connects the outlined red points from 1 to 5 which indicate the improvement in performance when the reference wind velocity used to tune the AO system becomes closer to the mean wind speed of the 2.5 second time series from the night in 2007.

AO. Next, the AO was tuned to the 2 minute mean (point 3) before the test segment. Finally, the AO system is tuned to the mean of the wind speed 2 seconds before the test segment (point 4). Point 5 shows when the instantaneous wind speed is tracked. As the mean wind speed used to tune the AO system gets closer to the actual on-sky wind speed, the contrast for the controller is optimized.

4.5 Conclusions

Using data from the TMT site testing campaign, we find a PSD function to describe the wind speed fluctuations at Mauna Kea at 7 m. We model the fluctuations with an ARTFIMA(0,-0.02,0.90,0) model.

We study the effects of wind speed on the contrast. We find that sub-second wind speed fluctuations affect the contrast by less than 5% and would therefore not significantly reduce the contrast for current HCI. However, changes in wind speed on longer timescales do have a significant impact on the contrast, particularly when the wind becomes faster than what was expected given the AO controller gain and WFS integration time. We show that running an integral controller optimized for a different wind speed than observed at the time of correction leads to a much larger loss in contrast than predicted by the fundamental limitations. To prevent this large loss in contrast, the AO system needs to track the wind speed at rates faster than 2 minutes for the given wind statistics on Mauna Kea.

References

Assémat, François, Richard W. Wilson, and Eric Gendron (Feb. 2006). "Method for simulating infinitely long and non stationary phase screens with optimized memory storage". In: *Opt. Express* 14.3, pp. 988–999.

Correia, C. M., K. Jackson, J.-P. Véran, D. Andersen, O. Lardière, and C. Bradley (June 2015). "Spatio-angular minimum-variance tomographic controller for multi-object adaptive-optics systems". In: *OSA* 54, p. 5281.

Doelman, Niek, Rufus Fraanje, Ivo Houtzager, and Michel Verhaegen (2009). "Adaptive and Real-time Optimal Control for Adaptive Optics Systems". In: *European Journal of Control* 15.3, pp. 480–488.

Doelman, Niek and James Osborn (2016). "Modelling and prediction of non-stationary optical turbulence behaviour". In: *Proc.SPIE* 9909, pp. 9909 - 9909 –8.

Gray, M., C. Petit, S. Rodionov, M. Bocquet, L. Bertino, M. Ferrari, and T. Fusco (Aug. 2014). "Local ensemble transform Kalman filter, a fast non-stationary control law for adaptive optics on ELTs: theoretical aspects and first simulation results". In: *Optics Express* 22, p. 20894.

Guyon, Olivier (Aug. 2005). "Limits of Adaptive Optics for High-Contrast Imaging". In: *The Astrophysical Journal* 629.1, pp. 592–614.

Hardy, J. W. (1998). "Adaptive Optics for Astronomical Telescopes". In: *Oxford University Press Jul 1998*.

Hinnen, Karel, Michel Verhaegen, and Niek Doelman (June 2007). "Exploiting the spatiotemporal correlation in adaptive optics using data-driven H2-optimal control". In: *J. Opt. Soc. Am. A* 24.6, pp. 1714–1725.

Hiriart, D., J.L. Ochoa, and García, B. (Oct. 2001). "Wind Power Spectrum measured at the San Pedro Martir Sierra". In: *American Astronomical Society* 37, pp. 213–220.

Jensen-Clem, R. et al. (Jan. 2018). "A New Standard for Assessing the Performance of High Contrast Imaging Systems". In: *Astronomical Journal* 155, p. 19.

Jolissaint, Laurent, Jean-Pierre Véran, and Rodolphe Conan (Feb. 2006). "Analytical modeling of adaptive optics: foundations of the phase spatial power spectrum approach". In: *J. Opt. Soc. Am. A* 23.2, pp. 382–394.

Kasper, Markus (2012). "Adaptive optics for high contrast imaging". In: *Proc.SPIE* 8447, pp. 8447 - 8447 –10.

Kooten, Maaike van, Niek Doelman, and Matthew Kenworthy (2018). "Implications for contrast as a result of the wind vector and non-stationary turbulence". In: *Adaptive Optics Systems VI*. Vol. 10703. International Society for Optics and Photonics, p. 107032C.

Le Roux, B., R. Ragazzoni, C. Arcidiacono, J.-M. Conan, C. Kulcsar, and H.-F. Raynaud (Oct. 2004). “Kalman-filter-based optimal control law for star-oriented and layer-oriented multiconjugate adaptive optics”. In: *Proc.SPIE* 5490, pp. 1336–1346.

Looze, Douglas P. (Jan. 2009). “Linear-quadratic-Gaussian control for adaptive optics systems using a hybrid model”. In: *J. Opt. Soc. Am. A* 26.1, pp. 1–9.

Mahrt, Larry (2011). “Surface Wind Direction Variability”. In: *Journal of Applied Meteorology and Climatology* 50.1, pp. 144–152.

Massioni, P., C. Kulcsár, H.-F. Raynaud, and J.-M. Conan (Nov. 2011). “Fast computation of an optimal controller for large-scale adaptive optics”. In: *Journal of the Optical Society of America A* 28, p. 2298.

Milli, J. et al. (Sept. 2017). “Performance of the extreme-AO instrument VLT/SPHERE and dependence on the atmospheric conditions”. In: *AO4ELT5*.

Pablo, Juan, Pérez Beaupuits, Angel Otárola, Fredrik T. Rantakyrö, Roberto C. Rivera, Simon J, E. Radford, and Larsaake Nyman (2004). “ANALYSIS OF WIND DATA GATHERED AT CHAJNANTOR”. In: *ALMA Memo* 497.

Paschall, R. N. and D. J. Anderson (Nov. 1993). “Linear quadratic Gaussian control of a deformable mirror adaptive optics system with time-delayed measurements”. In: *OSA* 32, pp. 6347–6358.

Sabzikar, Farzad, Mark M. Meerschaert, and Jinghua Chen (2015). “Tempered fractional calculus”. In: *Journal of Computational Physics* 293, pp. 14–28.

Schock, M. et al. (2009). “Thirty Meter Telescope Site Testing I: Overview”. In: *Publications of the Astronomical Society of the Pacific* 121.878, p. 384.

Srinath, S., L. A. Poyneer, A. R. Rudy, and S. M. Ammons (Dec. 2015). “Computationally efficient autoregressive method for generating phase screens with frozen flow and turbulence in optical simulations”. In: *Optics Express* 23, p. 33335.

Ziad, Aziz (2016). “Review of the outer scale of the atmospheric turbulence”. In: *Proc.SPIE* 9909, pp. 9909 - 9909 –12.

Chapter 5

Impact of time-variant turbulence behavior on prediction for adaptive optics systems

> "However it may prove, one must tread the path that need chooses!"
>
> J.R.R. Tolkien, *The Fellowship of the Ring*

Summary

For high contrast imaging systems, the time delay is one of the major limiting factors for the performance of the extreme adaptive optics (AO) sub-system and, in turn, the final contrast. The time delay is due to the finite time needed to measure the incoming disturbance and then apply the correction. By predicting the behavior of the atmospheric disturbance over the time delay we can in principle achieve a better AO performance. Atmospheric turbulence parameters which determine the wavefront phase fluctuations have time varying behavior. We present a stochastic model for wind speed and model time varying atmospheric turbulence effects using varying wind speed. We test a low-order, data-driven predictor, the linear minimum mean square error predictor, for a near-infrared AO system under varying conditions. Our results show varying wind has a significant impact on the performance of our predictor, preventing it from reaching optimal performance.

5.1 Introduction

Since the first direct image of an exoplanet by Chauvin et al. (2004), high contrast imaging (HCI) has been rapidly advancing. Capable of providing insight into planet formation, characterizing an exoplanet's atmosphere, and searching for signs of habitability, HCI spatially separates the planet's photons from the ones emitted by the host star. With multiple dedicated instruments such as SPHERE on the VLT (Beuzit et al., 2008), GPI on Gemini South (Macintosh et al., 2014), and SCExAO on Subaru (Jovanovic et al., 2015) many new observing techniques, better coronagraphs,

This chapter has been published as: Maaike van Kooten et al. (May 2019). "Impact of time-variant turbulence behavior on prediction for adaptive optics systems". In: *J. Opt. Soc. Am. A* 36.5, pp. 731–740.

and low noise detectors have been developed and tested. These efforts have resulted in processed contrast levels of $10^{-4} - 10^{-5}$ at 0.5” — 1” separation in the near infrared (Otten et al., 2017). To find cold jupiters, neptunes, and rocky planets, we need improve the contrast levels for HCI systems; aiming for $10^{-7} - 10^{-9}$ at separations of 0.05” — 1” at visible wavelengths.

Currently, one of the most significant limiting factors of a HCI system is the performance of the adaptive optics (AO) sub-systems (Kasper, 2012). Specifically, the time delay (which leads to the servo-lag error) prevents us from observing at small separations as a halo of speckles builds up close to the host star during a science exposure (Milli et al., 2017). In order to improve the performance of the HCI system, see Kasper (2012), the servo-lag error needs to be reduced. One approach to do this is to run the AO system faster, requiring higher speed deformable mirrors, fast wavefront sensors, and bright guide stars, thereby reducing the length of the lag. Alternatively, one can focus on understanding how the phase evolves during the delay and subsequently account for the dynamic behavior during the servo-lag. This is done through predictive control methods, where recent and/or nearby wavefront sensor measurements are used to predict the disturbance over the time lag. (Hardy, 1998)

5.1.1 Predictive control in adaptive optics

Predictive control to mitigate the effect of time delays in AO systems has been worked on for many years (Hardy, 1998). Prediction is not only promising for HCI but also for many different AO applications including improving performance for flux-limited laser guide stars and increasing sky coverage with natural guide stars (Jackson et al., 2015). Linear prediction has been very successful for tip-tilt compensation, especially when induced by structural vibrations as done by Petit et al. (2008), using Linear Quadratic Gaussian control (LQG). Work on the LQG controller for full atmospheric disturbance compensation has also been done by Le Roux et al. (2004). Different predictors, closely related to the Kalman filter, have allowed for filtering in real time and are now being used in laboratory testing as well as in on-sky testing (Paschall and Anderson, 1993; Le Roux et al., 2004; Looze, 2009; Gray et al., 2014; Massioni et al., 2011; Correia et al., 2015). The closely related data-driven H2 optimal controller (Doelman, Fraanje, Houtzager, et al., 2009; Hinnen et al., 2007; Doelman, Fraanje, and Breeje, 2011) was also tested on-sky, for tip/tilt, showing a reduction in the temporal error. More recently, Guyon and Males (2017) show theoretically that Empirical Orthogonal Functions can improve the contrast of a HCI system by a couple orders of magnitude through prediction. Many of these approaches are based on the assumption that atmospheric turbulence induced wavefront phase fluctuations are a stationary stochastic process. However, in nature, turbulence is a time variant process with the mean phase value and variance changing in time. Adaptive predictors have been proposed by van Kooten et al. (2017) to track the time-varying behavior of statistics of atmospheric turbulence. Although some predictors might be robust against non-stationarities, none have been rigorously tested under time-varying conditions. Therefore, in this work, we look at basic data-driven prediction and test different implementations under time varying conditions.

5.1.2 Atmospheric Non-stationarity

Predictive controllers inherently depend on knowledge of turbulence parameters, as well as the dynamical behavior of the AO system. We know the relevant turbulence parameters such as coherence length, outerscale, and wind speed vary, resulting in variations of the mean and variance of phase aberrations. Atmospheric turbulence induced phase fluctuations are essentially time variant. If we account for this behavior in simulation, we will be able to determine the behavior of a predictor under time varying conditions.

5.1.3 Simulating atmospheric phase

The most recent algorithms for generating atmospheric phase disturbance in simulation, by Assémat et al. (2006), have been proposed to minimize computation time as well as include the effects of boiling (Srinath et al., 2015). They also have flexible architectures that allow for the wind speed, outerscale and Fried parameter to vary at each time step. However, they do not propose how these parameters should vary in time. Without information on how these parameters vary, we are unable to test new control techniques in a simulation environment that reflects all the behavior of the disturbance seen on-sky and instead can only test them under the average behavior.

5.1.4 Outline

In this paper, we focus on understanding the atmospheric wavefront phase fluctuations of an AO system on short time scales and how the disturbance's time-varying behavior affects a data-driven prediction algorithm. In Section 5.2, we look at the dynamical behavior of relevant turbulence parameters—including the wind vector, outerscale, and the Fried parameter—used to describe atmospheric wavefront phase fluctuations. We then present our simulation environment in Section 5.3 and introduce a data-driven prediction algorithm in Section 5.3.2. We present our results for varying wind in Section 5.4 and discuss their impact in Section 5.5. Our future work is proposed in Section 5.6.

5.2 Describing wavefront phase fluctuations

In AO the atmospheric wavefront phase fluctuations are often described as a stationary process with a given variance represented by a spatial covariance function. By assuming Taylor's Frozen Flow hypothesis, we can extend this spatial covariance function to a temporal covariance function through relation with a constant wind speed. Within this framework we can test many different seeing conditions.

Extending the above to time variant wavefront phase fluctuations, we vary the wind speed (v), the Fried parameter (r_0), and outerscale (L_0).

5.2.1 Atmospheric Covariance function

We can describe the spatial covariance of atmospheric phase fluctuaton, α, by von Karman model (Conan, 2000) as in Equation 5.1.

$$C_\alpha(r) = \left(\frac{L_0}{r_0}\right)^{5/3} \frac{\Gamma(11/6)}{2^{5/6}\pi^{8/3}} \left(\frac{24\Gamma(6/5)}{5}\right)^{5/6} \left(\frac{2\pi r}{L_0}\right)^{5/6} K_{5/6}(2\pi r/L_0) \tag{5.1}$$

where $\Gamma(x)$ is the gamma function and $K_u(x)$ is the modified Bessel function of order u.

Using the Frozen Flow hypothesis, we can describe a spatial separation, r, as a shift over a short period of time, t, due to v. The temporal covariance follows when this is applied to Equation 5.1.

The wind speed then influences the temporal covariance function. The spatial and temporal covariances are both influenced by L_0 and r_0. We therefore turn our attention to understanding how these three parameters change in time. First we present a model for the wind vector, then we briefly discuss the behavior of the r_0 and L_0 as they are understood in the above covariance functions.

Wind Vector

Taking wind data from the Thirty Metre Telescope (TMT) site testing campaign at Mauna Kea by Schock et al. (2009), we look at the temporal behavior of the wind speed. The data is from a sonic anemometer at a height of 7 metres above the summit of Mauna Kea, with a variable sampling frequency between 10-60 Hertz. We look at the wind speed and direction fluctuations over a period of three years (2006-2008). From this data set we are able to define a stochastic model that describes the averaged power spectral density (PSD) from night time wind speed data for the ground layer. For each night we look at wind speeds faster than 1 m/s. We observe substantial fluctuations in wind speed (greater than 1 m/s) and wind direction (tens of degrees) at frequencies of 1 Hertz or greater. We observe 3 types of wind behavior from our analysis that represent a large portion of the data (Figure 5.2). In general, over the course of the night either the wind direction or the wind speed can be the dominate source for the fluctuating wind vector. We do not observe nights where both change by large amounts at the same time. Besides these two cases we also have nights where the mean wind speed and wind direction as well as their variances stay the same throughout the night. We consider this to be a realistic Frozen Flow case. These 3 wind behaviors observed is summarized in Table 5.1. We chose to ignore wind direction the remainder of this work due to large fluctuations in direction for slow wind speeds (van Kooten et al., 2018).

To estimate a wind speed PSD we split the night into shorter time segments of 10 minutes. We estimate the PSD using the Lomb-Scargle approach for each segment after de-trending and then take the average to determine the overall PSD for that night. We do this for all nights available, determining an average PSD for the

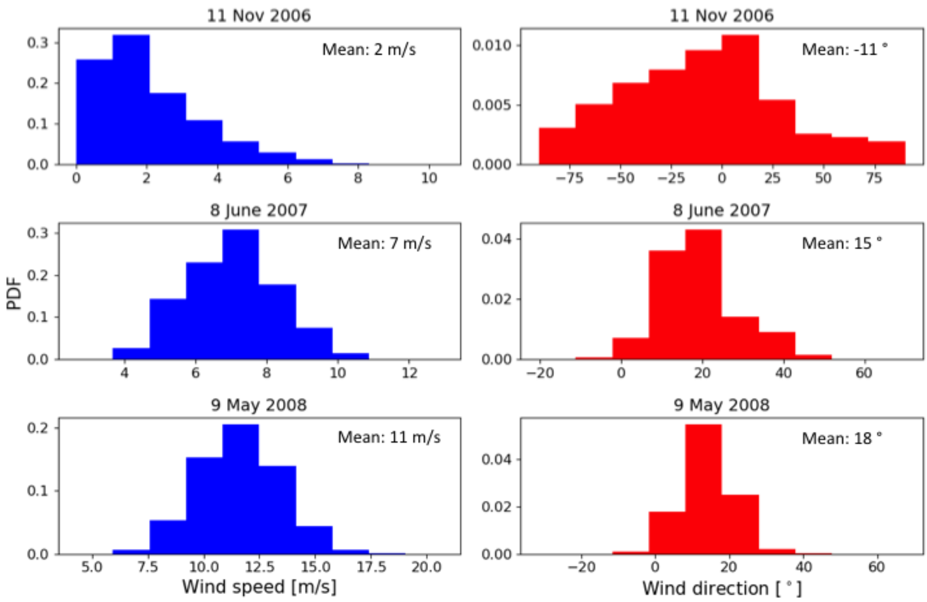

Figure 5.1: Histograms of wind direction and wind speed for three different nights that correspond to the cases in Table 5.1.

Classification	Wind Speed	Wind direction	Example nights
Varying wind direction	Slow (<5 m/s)	Large variance ($\pm 100^{\circ}$)	2006.11.22
Realistic Frozen Flow	Fast (>8 m/s) with medium variance	Small variance	2008.05.09
Varying wind speed	Large variance (0-20 m/s)	Small variance	2007.06.15

Table 5.1: Three classifications of wind vector behavior seen in our data.

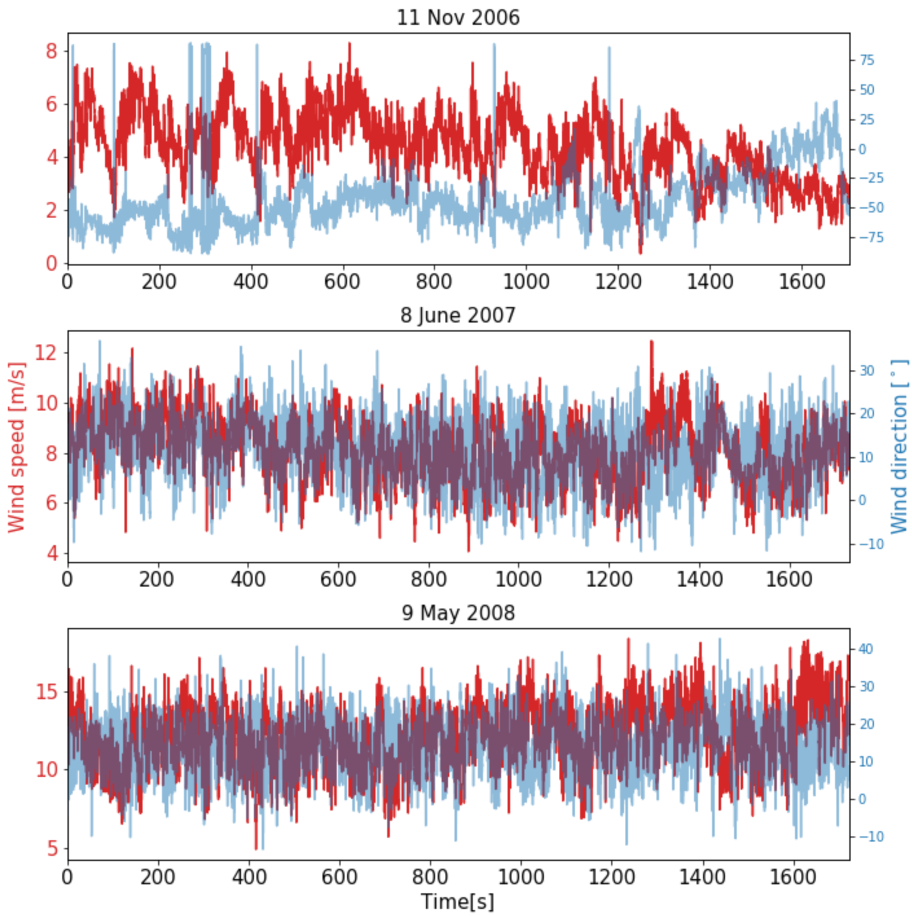

Figure 5.2: Raw time series for three different nights showing the classification in Table 5.1. The data is first filtered using a Butterworth filter to remove a measurement artifact at 20 Hertz due to the sonic anamometer electronics before feeding into our simulations.

wind speed during the period of observations, Figure 5.3. A more in-depth study of the wind statistics and how we estimated the wind's power spectral density is in van Kooten et al. (2018). Here we extend the stochastic model we previously found to capture the roll-off at low frequencies by extending the order of the model proposed to include a tempering component. The resulting stochastic model is a tempered fractionally integrated autoregressive moving average model (ARTFIMA) (Meerschaert and Sabzikar, 2013). Equation 5.2 shows the power spectral density for our model.

$$\Phi(k) = |\frac{(1-1.0047e^{-ik})}{(1-0.999e^{-ik})}|^2|(1-e^{-0.016-ik})|^{-2(0.91)} \tag{5.2}$$

with the angular frequency $k = 2\pi\, f/f_s$ with f the frequency ranging from 0.002 Hz to 10 Hz and f_s=20 Hz.

We present this model for ground layer wind speed on Mauna Kea for the TMT site locationto be used to generate time variant turbulence simulations via varying wind. This model provides a good fit to the individual nightly PSD as well as the averaged PSD, as the overall shape of the PSD remains constant. The gain of the nightly PSD does vary by one order of magnitude throughout the data set.

Fried Parameter

The Fried parameter (r_0) is considered the main turbulence parameter in astronomy that directly influences the achievable imaging resolution. In reality, r_0 varies in time with the turbulence in the atmosphere.

A dynamic r_0 model from Doelman, Fraanje, Houtzager, et al. (2009) was determined from 18 nights of data from La Palma. The model was estimated from data with sampling times ranging from 80 to 120 seconds. This model, therefore, does not include how r_0 behaviors at sub-second timescales and we do not know how it varies on AO timescales, as no other data is available. Therefore, we do not include varying r_0 in our simulations.

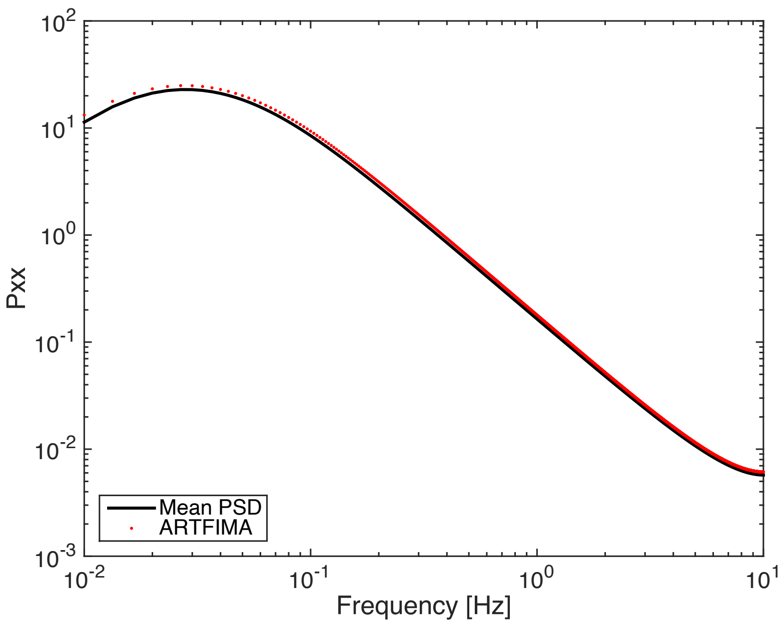

Figure 5.3: Fit of the ARTFIMA model. The black line shows the averaged PSD determined from the data while the red shows the PSD from the ARTFIMA model.

Outerscale

Many efforts have focused on accurately determining L_0 of turbulence with estimations ranging from 5-300 metres (Ziad, 2016). From observational campaigns, average values, probability density functions (PDF), and even a time series over the course of a night have been reported. However, the insights only apply to longer timescales, meaning we do not have sufficient knowledge to model the behavior of L_0 for AO control loop timescales.

5.3 Methods

5.3.1 Turbulence simulation

We use the method developed by Assémat et al. (2006) to generate phase screens with von Karman statistics. It has been included in the HCI Python package, HCIPy being developed at Leiden Observatory by Por et al. (2018). At each time step, the phase screen is updated by the algorithm, allowing for infinite phase screen generation as well as continuous updating of the wind vector (speed and direction), r_0, and L_0. This framework allows for non-stationarity behavior to be simulated in an efficient way.

We chose our AO system configuration to be representative of an Extremely Large Telescope (ELT) scale system for HCI based on the planned METIS system for the ELT (Brandl et al., 2016). We model a single layer atmosphere. See Table 5.2 for configuration details. We assume a idealized wavefront sensor where we measure the averaged phase value over the subaperture at a given instantance in time. The total additional noise not due to the servo-lag error has a variance 50 times smaller than the full wavefront phase variance. These choices allow us to focus on the effects of the delay and how a predictor performs.

For the remainder of this work we assume a constant Fried parameter of 13 centimetres at 500 nanometres. For stationary wind cases we use a constant wind speed of 12 m/s unless indicated otherwise. Finally, we assume a constant L_0 of 24 metres unless indicated otherwise.

In our simulations, we predictor using the open-loop phase and estimate the error at each time step for our predictor. We can also choose to predict in closed-loop residual phase. However, in reality, our closed-loop predictor will also depend

Table 5.2: Simulation parameters for our AO system including the sub-aperture (S.A.) size.

λ_{WFS}	D [m]	N_{WFS}	S.A. size [m]	r_0 [m]	Frame delay	Loop speed
2.2 μ m	39	74^2	0.5	0.77	2 samples = 2 ms	1 kHz

on the response of the controller itself and therefore we will need to be account for in the predictor itself.

Wind

Since we have real wind time series available, we use this in our simulations. From the site testing data from TMT, we classify the behavior of the wind vector into three classes as shown in Table 5.1. Six 5 second sections (separated by at least 10 minutes in time) for each case are chosen for three days that are representative cases of our classification. The data are linearly interpolated to the AO loop speed allowing the wind speed to be updated at each time step in the simulation.

5.3.2 Data-driven prediction

In Section 5.2 the time-varying behavior of v, r_0, and L_0 are described and well as the difficulties in developing a time variant model for atmospheric turbulence. Currently, we only have a model for ground layer v which is site dependent. We, therefore, turn to data-driven methods which use on-sky data to determine the predictor; specifically the linear minimum mean square error (LMMSE) predictor. In this section, we present the framework for the LMMSE predictor and in Section 5.3.5 we place our work in relation to some of the other prediction methods for AO.

We denote the phase at a single point i of a phase screen at time t, $y_i(t)$, and $u(\vec{t})$ a P×1 column vector containing a collection of P phase values on a discrete spatial grid at time t (therefore P is the spatial order). We then assume that the future value of a given phase point, $\hat{y}_i$ at the discrete time index $t+d$, is a linear combination of the most recent phase values (our regressors) at time t. Note that we do not have to use all the phase values on our spatial grid but are able to select the spatial order by choosing a region around our point of interest (changing P). We use $\vec{a}_i$ to represent the predictor coefficients. With the above, we define the following where we use T to denote the transpose:

$$\hat{y}_i(t+d) = \vec{a}_i^T \cdot \vec{u}(t) \tag{5.3}$$

$$\vec{u}(t) = \begin{pmatrix} y_0(t) & y_1(t) & y_2(t) & \dots & y_P(t) \end{pmatrix}^T \tag{5.4}$$

We can expand this to include a set of Q most recent measurements and thereby including more temporal information.

$$\vec{w} = \begin{pmatrix} \vec{u}(t)^T & \vec{u}(t-1)^T & \vec{u}(t-2)^T & \dots & \vec{u}(t-Q)^T \end{pmatrix}^T \tag{5.5}$$

We therefore allow for both spatial and temporal regressors through Equation 5.5, where w is a vector of PQ×1. We have a spatial order of P and a temporal order of Q resulting in the total of PQ regressors.

With $<>_t$ being the time average operator, we minimize the cost function:

$$min_{\vec{a}_i} < ||y_i(t+d) - \vec{a}_i^T \vec{w}(t)||^2 >_t \tag{5.6}$$

finding the vector of predictor (filter) coefficients, $\vec{a}_i$, now a $PQ \times 1$ vector. Equation 5.6 represents the time-averaged mean square prediction error.

The strength of this method is that the algorithm immediately extracts any spatio-temporal information from the data - the regressors - provided. It is important to realize for AO that the temporal sampling is much finer than the spatial sampling.

Solving Equation 5.6 for our zero-mean stochastic process, the solution can be written in terms of the inverse of the auto-covariance matrix and cross-covariance vector (Haykin, 2002).

$$\vec{a}_i = \mathbf{C}^+_{\vec{w}\vec{w}} \vec{c}_{\vec{w}y_i} \tag{5.7}$$

where + denotes a pseudo inverse. $\mathbf{C}_{\vec{w}\vec{w}}$ is the auto-covariance matrix of $\vec{w}$, the vector containing the regressors, and $c_{\vec{w}y_i}$ is the vector containing the cross-covariance between the true phase value,y_i and $\vec{w}$.

Looking at Equation 5.7 the optimal AO predictor based on the spatial covariance (Equation 5.1) can be derived for stationary turbulence (Beghi et al., 2007). However, we choose a data-driven approach where we estimate the covariances using measured data collected over a short period. During the collection period (or training period), this batch LMMSE predictor cannot be used (or we can use a previously calculated solution) and is considered off-line.

In the batch-wise approach, once the prediction vector is found it is fixed for the rest of the simulation. By making use of the matrix inversion lemma, we can form a recursive solution in which the pseudo-inverse of the auto-covariance is updated according to Equation 5.8 and the cross-covariance is updated by Equation. 5.9 (Haykin, 2002).

$$\mathbf{C}^+_{\vec{w}\vec{w}}(t) = \mathbf{C}^+_{\vec{w}\vec{w}}(t-1) - \frac{\mathbf{C}^+_{\vec{w}\vec{w}}(t-1)\vec{w}(t-1)\vec{w}^T(t-1)\mathbf{C}^+_{\vec{w}\vec{w}}(t-1)}{1+\vec{w}^T(t-1)\mathbf{C}^+_{\vec{w}\vec{w}}(t-1)\vec{w}(t-1)} \tag{5.8}$$

$$c_{\vec{w}y_i}(t) = c_{\vec{w}y_i}(t-1) + y_i(t-1)\vec{w}^T(t-1) \tag{5.9}$$

Substituting Equations 5.8 and 5.9 into Equation 5.7 can then update the prediction vector using:

$$\begin{aligned}\vec{a}_i(t) = \vec{a}_i(t-1) + \mathbf{C}^+_{\vec{w}\vec{w}}(t-1)y_i(t-1)\vec{w}^T(t-1) - \\ (c_{\vec{w}y_i})(t-1) + y_i(t-1)\vec{w}^T(t-1))\frac{\mathbf{C}^+_{\vec{w}\vec{w}}(t-1)\vec{w}^T(t-1)\vec{w}(t-1)\mathbf{C}^+_{\vec{w}\vec{w}}(t-1)}{1+\vec{w}^T(t-1)\mathbf{C}^+_{\vec{w}\vec{w}}(t-1)\vec{w}(t-1)}\end{aligned} \tag{5.10}$$

The recursive solution goes on-line immediately with the initial covariance being set to diagonal matrices with large values (as done with recursive least-squares methods). The solution is quick to converge compared to gradient based methods. The recursive solution depends on all previous measurements finding the optimal solution for all previous data.

5.3.3 The effect of atmospheric parameters on prediction

As mentioned above, using the covariance in Section 5.2.1 we can derive our optimal predictor in terms of the theoretical covariance. We can then see how the predictor depends on the atmospheric parameters.

For example, the diagonal elements in $\mathbf{C}_{\vec{w}\vec{w}}$ (Conan, 2000) are given by:

$$C_\alpha(0) = \frac{L_0}{r_0}^{5/3} \frac{\Gamma(11/6)}{2\pi^{8/3}} \left(\frac{24\Gamma(6/5)}{5}\right)^{5/6} \tag{5.11}$$

while the off-diagonal elements are given by Equation 5.1.

We can then represent $\mathbf{C}_{\vec{w}\vec{w}}$ as a matrix $\mathbf{F}_{\vec{w}\vec{w}}$ multiplied by the scalar $C_\alpha(0)$. Therefore:

$$\mathbf{C}^{+}_{\vec{w}\vec{w}} = \frac{1}{C_\alpha(0)} \mathbf{F}^{+}_{\vec{w}\vec{w}} \tag{5.12}$$

Similarly, we can represent the cross-covariance vector as:

$$\vec{c}_{\vec{w}y_i} = C_\alpha(0) f_{\vec{w}y_i} \tag{5.13}$$

Inserting Equations 5.13 and 5.12 into Equation 5.7 we obtain the following:

$$\vec{a}_i = \mathbf{F}^{+}_{\vec{w}\vec{w}} f_{\vec{w}y_i} \tag{5.14}$$

Equation 5.14 does not depend on r_0 (only present in g), but is instead dependent on L_0 and v (applying Frozen Flow approximation). Therefore, when v or L_0 vary our optimal predictor changes as well.

5.3.4 Dealing with time-varying behavior

Both the batch and recursive methods are originally designed for stationary problems and so we apply them to our stationary case. To make these methods suitable for time varying cases, the batch can be retrained and reset as frequently as needed. We can introduce a forgetting factor for the recursive LMMSE that is applied during the predictor update, Equation 5.8. This allows for the recursive method to ignore the previous states of the turbulence by gradually reducing the weighting of old observations in the prediction.

5.3.5 Comparison to other predictors

Before looking at the performance and behavior of the LMMSE predictor we first put our work in context of prediction for AO. We aim to give a brief overview of prediction in AO for methods with similar structure to ours but do not claim to be a complete overview. The batch LMMSE is very similar to the Empirical Orthogonal Function (Guyon and Males, 2017) approach with a slightly different implementation for the matrix inversion. Many other data-driven predictors have been proposed including the traveling wave predictor by Hardy (1998) that makes use of the Frozen Flow hypothesis. By knowing the wind vector, one can spatially shift the current phase measurements; predicting what the wavefront will look like at the time of our correction. We can therefore represent the traveling wave predictor in our own framework where we do not need knowledge of the wind speed but instead it is extracted intrinsically in the LMMSE algorithm. More specifically, if we choose our regressors such that we only allow the most recent measurement, our LMMSE will find a pure spatial solution that is equivalent to the traveling wave predictor. Finally, we can have a pure temporal solution that only uses recent measurements for the phase point of interest. When we limit ourselves to the most recent measurement only for the batch-wise LMMSE predictor, we get the equivalent of the closed-loop integrator with some gain. The integrator and our s1t1 are often not classified as a predictor; however, they are sometimes considered zero order predictors (Hardy, 1998). If we include multiple previous measurements, we can form a higher order temporal predictor that is similar to an AR-structure approach (Le Roux et al., 2004) (that might be used in the optimal control framework).

Within the multi-congugate AO (MCAO) community, the inclusion of a prediction step combined with phase reconstruction has result in the spatial angular (SA) predictor which makes use of Frozen Flow to perform spatial shift, for a given layer, as part of the reconstruction. Looking at a single layer, on-axis, the SA would perform the same as our spatially only LMMSE algorithm (Correia et al., 2015; Jackson et al., 2015). Other MCAO work has focused on prediction using a Kalman filter as the phase estimator (Piatrou and Roggemann, 2007) and then performing a moving grid prediction (based off prior wind knowledge) during the DM fitting step. This combines both spatial and temporal information to perform prediction which is also possible in our frame work.

5.4 Simulation Experiments

In this section, we present and discuss a number of different simulation results, starting with the case of stationary turbulence in order to gain intuition on how the LMMSE behaves under these conditions. We then present the results for time variant turbulence, applying the LMMSE predictor for the case of varying wind speed from field measurements.

5.4.1 Stationary turbulence

We limit the input data into the LMMSE algorithms by selecting a grid size of 5-by-5 phase points (regressors) of the most recent measurement to predict the central phase point 3 time steps into the future. For ease, we abbreviate our LMMSE with spatial order 5 and temporal order 1 to s5t1 (see Section 5.3.2). We then define our 's1t1' solution as our classical solution. For this case, the algorithm only sees the most recent measurement of one spatial point. This is a pure temporal solution with a history of 1 frame (the most recent measurement). We simply train it with a few frames and keep the solution static. Looking at the pure spatial LMMSE we see the prediction coefficients found by the LMMSE in a Frozen Flow case with a $r_0 = 0.13$ metres (at 500 nanometres) and $v = 10$ m/s, Figure 5.4. Both the batch and recursive solutions show that the phase value at the yellow grid point has been identified as the largest contributor to the behavior of the central phase (outlined in red) at the next time step. Here the phase itself is the largest contributor. However, they both give a slight weighting (∼0.1) to the neighboring point, indicating that the wind is shifting horizontally. The solution is not spread over many spatial points because the sub-apertures are so large and we are sampling the atmosphere at 1 kiloHertz, with the phase screen traveling less than 0.5 subapertures per sample interval.

On the right in Figure 5.4 we plot the results for the stationary case. We run 10 simulations with the same input parameters (for all future runs as well). We calculate the root-mean-square (RMS) for the 10 residual phase screens at the same time instance. We shaded regions indicate the 1-sigma level. We see that s5t1 performs better than our s1t1 for a single layer Frozen Flow atmosphere. This behavior holds true under a variety of turbulence conditions (different values of v, r_0, and L_0). This validates our LMMSE algorithms; under stationary conditions, we can use prediction to increase our performance compared to the static pure temporal solution s1t1.

In the first 5 seconds of Figure 5.5 we show how different spatio-temporal predictors with different orders converge differently and are even able to achieve different final performance levels despite having converged fully for different amounts of spatio-temporal information. The amount of data in the solution controls how fast the solution fully converges as well as the residual variance. For higher order spatio-temporal solutions, the convergence rate is slower but the residual variance is smaller. It is important to note that the amount of input data increases much more for increases in spatial information as we radially increase the spatial information (as opposed to temporal information) as to not be biased towards a specific wind direction. The LMMSE is convenient in that it allows us to choose the amount of input data used for prediction to minimize computation time - either through an identification routine (i.e., single value decomposition while finding the batch solution or manually based on prior knowledge). We choose to limit the amount of information by knowledge of the physical constraints of the AO system such as the spatial sampling of the wavefront sensor and the temporal resolution as well as wind conditions. For example, for our system we expect a maximum of 14 m/s winds, therefore, our turbulence in one time step does not move more than one subaperture. Hence, we need one spatial subaperture mimimum to capture most of the effects. We chose to increase this to two subapertures to provide edge information but maintaining symmetry as to not have preference to a wind direction means we land up with a 3-by-3 grid instead of the full grid of 74-by-74. Not only is this attractive to reduce computation but for recursive methods, allows for the solution to converge faster.

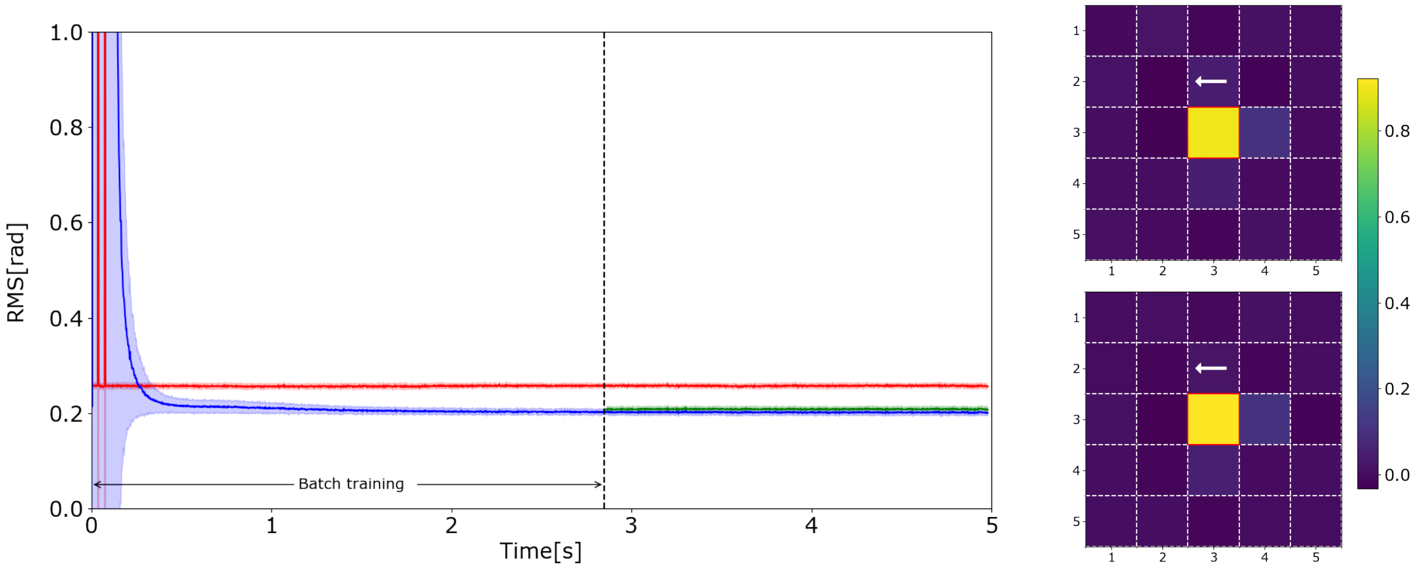

Figure 5.4: Left: The mean residual wavefront error for multiple simulations as a function of time for our s1t1 classical solution (red line), batch LMMSE (green line), and recursive LMMSE (blue line). Right: The prediction coefficients for one phase point (outlined in red) for both the batch (top) and recursive (bottom) solutions. The arrow indicates the wind direction.

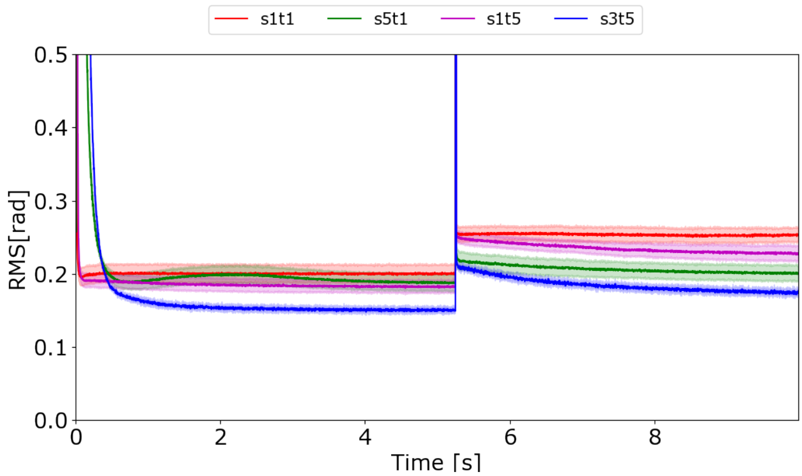

Figure 5.5: Error and convergence of linear predictors with various regressor orders (top) before and after a jump in wind speed (bottom).

5.4.2 Effects due to time varying wind speed

With knowledge of how the LMMSE behaves under stationary conditions, we can study the effects of time varying atmospheric turbulence on our predictors. For this work we set the regressors to be a 3-by-3 spatial grid for 5 previous measurements for each phase point (s3t5). We focus our attention on the effect of a varying wind.

To start, we look at a very simple case for varying wind. Figure 5.5 shows the effect of an instantaneous wind speed jump of 7 m/s. First, we note that as the wind speed increases, the benefit of our predictor increases (i.e., the relative difference between the s3t5 solution and the classical solution). We can see that the recursive algorithm takes a long time (a few seconds) to converge back to its optimal solution after a change in wind speed.

In Figure 5.6 we compare the three different types of LMMSE algorithms for our s3t5 solution under a wind speed jump. The first being the non-adaptive solution: the recursive LMMSE predictor. By knowing the moment when the wind speed changes we are able to recalibrate our batch LMMSE predictor to minimize the loss in performance - this is one type of adaptive solution. Finally, we show our second adaptive algorithm (and third LMMSE algorithm), the forgetting LMMSE predictor. We can see that after the wind jump the forgetting converges faster than the recursive. Eventually the forgetting LMMSE predictor converges the optimal solution calculated off-line in this case. The recursive LMMSE predictor updates the covariance estimate when new data becomes available (Equations 5.8 and 5.9). THe estimation makes use of all previous data. Therefore, it will not be able to forget the data before the jump and therefore, will not achieve the same performance as the other algorithms.

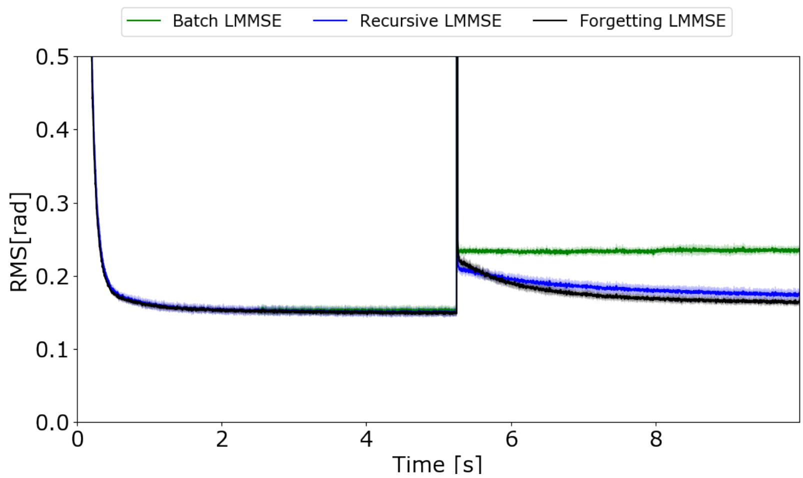

Figure 5.6: Wind jump of 7 m/s on a METIS scaled system showing the convergence of the recursive LMMSE (blue) and the forgetting LMMSE (black) as well as the resetting of the batch LMMSE (green) for s3t5.

Wind speed fluctuations

We now look at the behavior for wind speed fluctuations, shown from Figures 5.7 to 5.12. We do this for two different L_0 values: one smaller than the telescope diameter (24 metres) and one larger than the telescope diameter (80 metres). We plot our adaptive LMMSE solutions: the forgetting LMMSE and the resetting batch LMMSE. As in reality, the batch has no knowledge of the wind speed behavior and is arbitrarily reset. For the classical solution (s1t1), we once again plot the s1t1 solution. Finally, we plot our ideal s3t5 predictor. The ideal predictor is the s3t5 solution under infinite tracking speed and mimicking an instantaneous stationary case. We pre-determine the s3t5 predictor for each potential wind speed assuming stationary conditions and then use a look-up table to find our ideal predictor performance for Figures 5.7 to 5.12. This provides us with a lower bound of a s3t5 predictor's performance. We run the simulation for multiple cases of varying wind on the same night and average the results. This is done for the three different nights shown in Section 5.2.1. We plot the mean wind speed and 1-σ (standard deviation) levels (shaded region) for the wind speed as well as the different predictors.

5.5 Analysis

We summarize the results of Section 5.4.2 and Figures 5.7 through 5.12 in Table 5.3. We then make the following conclusions:

1. All of our LMMSE approaches lose performance when compared to the ideal predictor under varying wind (ratio for the batch and forgetting LMMSE is greater than 1).

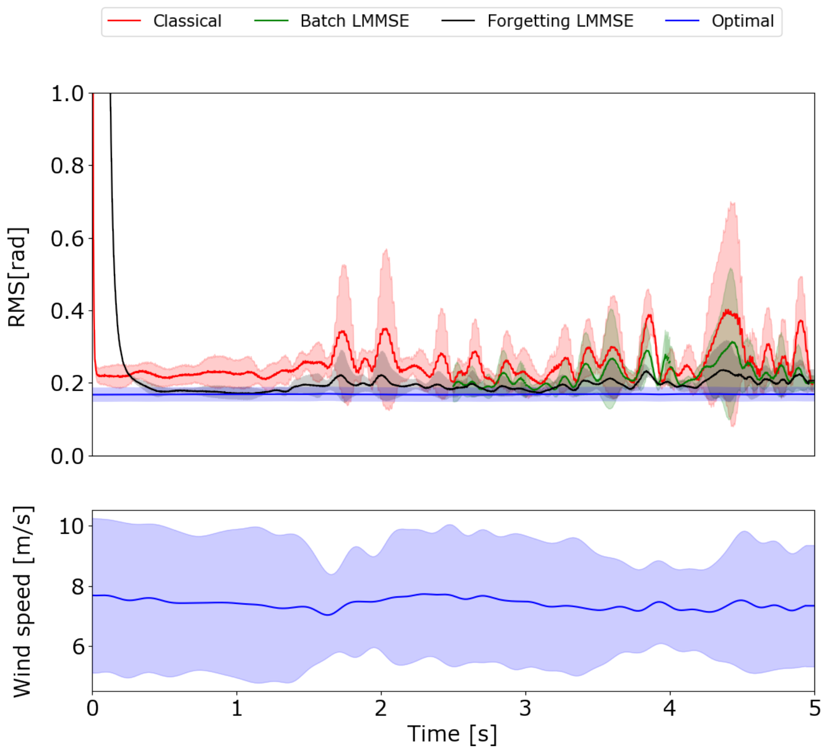

Figure 5.7: 2007.06.15, $L_0 = 24$ m

Table 5.3: Summary of Figures 5.7 to 5.12 showing the ratio of the mean rms value of an algorithm and the mean rms to the optimal LMMSE.

Date	2007.06.15		2008.05.09		2006.11.22	
Outerscale	24 m	80 m	24 m	80 m	24 m	80 m
Classical	1.42	1.40	1.96	1.59	1.19	1.49
Batch LMMSE	1.21	1.19	1.83	1.55	1.59	1.77
Forgetting LMMSE	1.08	1.13	1.47	1.35	1.04	1.36

2. The forgetting implementation does better than the resetting batch implementation (forgetting LMMSE ratio is smaller than the batch LMMSE ratio).
3. The difference between s3t5 and the classical solution becomes smaller under varying wind.
4. The optimal solution has a much smaller variance compared to the other algorithms.

We conclude that a different predictive control approach (that can either track faster or is less sensitive to non-stationarities) is needed to predict atmospheric turbulence in the presence of time-varying turbulence as it is noticeably different than the sta-

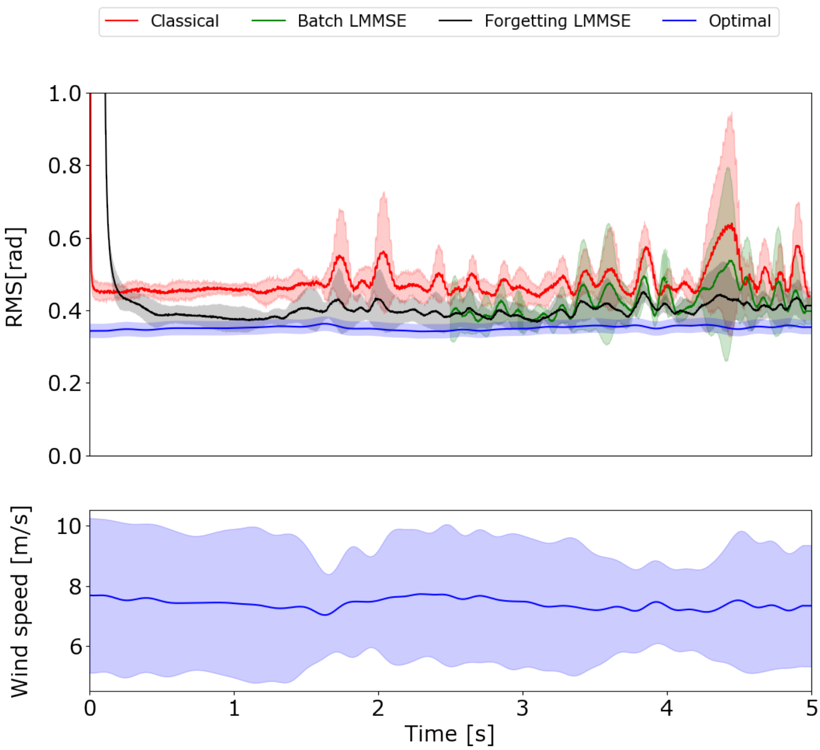

Figure 5.8: The average response for our predictors (upper panel) for three different wind conditions corresponding to Table 1 (lower panel), with $L_0 = 80$ m for wind on the day of 2007.06.15. We plot the s1t1 predictor (red), the s3t5 resetting batch LMMSE (green), the s3t5 forgetting LMMSE (black), and the s3t5 ideal LMMSE (blue). We first allow the batch to train on 2.5 seconds of data (to be consistent with previous simulations) and then reset it every 1 second.

tionary case.

More specifically, from the plots in Figures 5.7 through 5.12 the benefits of our LMMSE predictors are modest. From the optimal solution, we not only see a loss in residual mean wavefront error (see Table 5.3) but also have much larger variances for our LMMSE. Ideally, a predictor would also provide a stable correction.

In all three wind cases, the forgetting LMMSE predictor is able to do fairly well, reaching the ideal solution, for the first couple of seconds. However, the algorithm is unable to handle the non-stationarities as seen by the increase in variance compared to the optimal solution that has infinite tracking capabilities. We attribute this to the continuously changing wind. As we see in Figure 5.6, the forgetting algorithm needs between 0.5 s to 1 s to recover from a large jump, in part due to the number of regressors, and in part due to the magnitude of the change in wind speed. The forgetting LMMSE predictor performs better for slowly evolving changes than fast

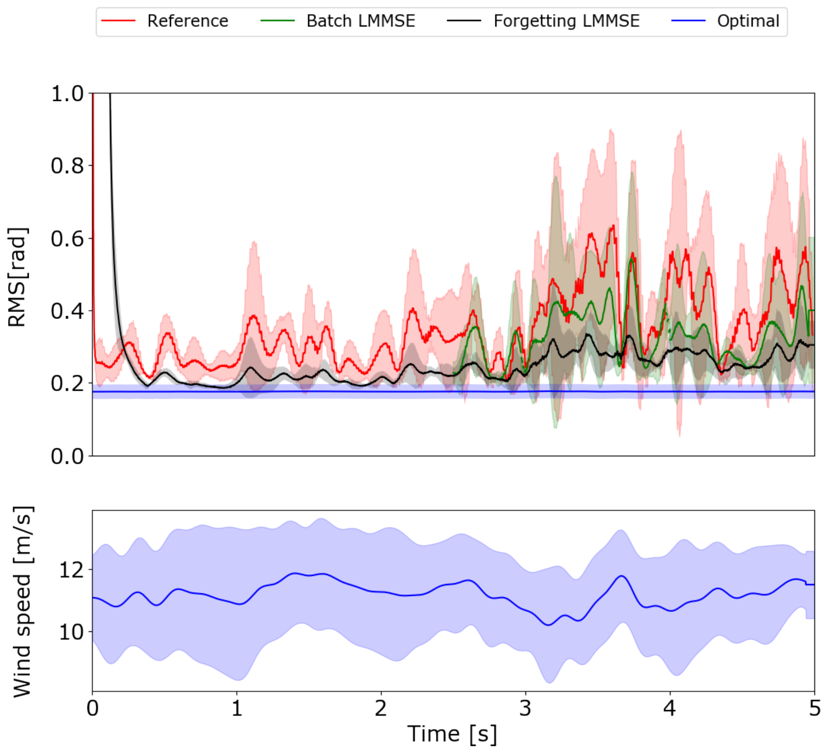

Figure 5.9: The average response for our predictors (upper panel) for three different wind conditions corresponding to Table 1 (lower panel), with $L_0 = 24$ m for wind on the day of 2008.05.09. We plot the s1t1 predictor (red), the s3t5 resetting batch LMMSE (green), the s3t5 forgetting LMMSE (black), and the s3t5 ideal LMMSE (blue). We first allow the batch to train on 2.5 seconds of data (to be consistent with previous simulations) and then reset it every 1 second.

changes. From Table 5.3 we see that the forgetting LMMSE does better than the resetting batch predictor in every case.

5.5.1 Further Discussion

From the stationary tests we can conclude that the LMMSE algorithms with higher order spatio-temporal solutions have a benefit compared to a pure temporal solution making use of only the most recent measurement as we would expect from using Frozen Flow to generate our atmospheric turbulence phase. This agrees with the literature that prediction (whether model-based or data-driven) can provide a reduction in the servo-lag error and the overall residual wavefront error.

The wind fluctuations reported by the TMT site testing group adversely impact the basic predictor—the LMMSE—except for the specific case of slowly moving wind speed. Wind speeds can fluctuate by over 1 m/s on time scales less than 1 second.

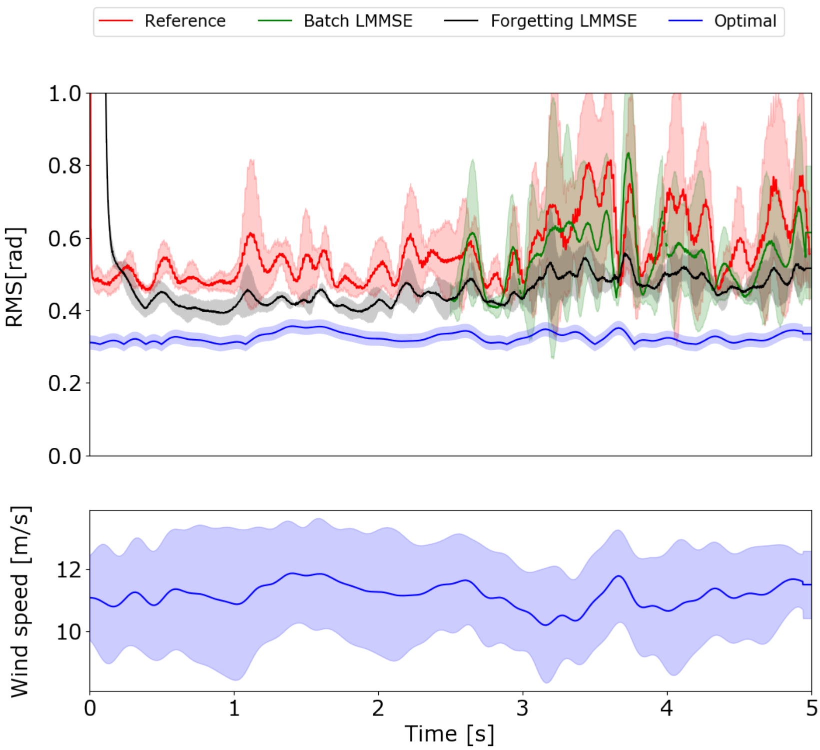

Figure 5.10: Same as Figure 5.7 but for $L_0 = 80$ m with winds according to the date 2008.05.09.

Under time-varying conditions we would expect only a minor performance improvement for a single conjugate AO system with a low order LMMSE predictor compared to no prediction when the system is dominated by the servo-lag error. It is important, however, to note that due to the measurement height of 7 metres these measurements might not reflect what is actually seen by an AO system as the dome and other buildings will influence the low-layer winds. These fluctuations might also be extreme when compared to other astronomical sites. Finally, by limiting our analysis to the ground layer (due to available data), we might be over estimating the strength and timescales of the wind fluctuations and therefore the effect on prediction as in many cases the higher layers are the dominate source for the wind driven halo (Cantalloube et al., 2018).

Assessing our prediction in the presence of our wind fluctuations we quickly see why on-sky test campaigns for predictive AO control are more challenging than common laboratory tests. A single wind jump step already provides a challenge for the LMMSE, moving it away from the ideal predictor solution (Figure 5.5). When we extend our simulation to real wind data, the LMMSE has a harder time tracking the changes (Figures 5.7 through 5.12).

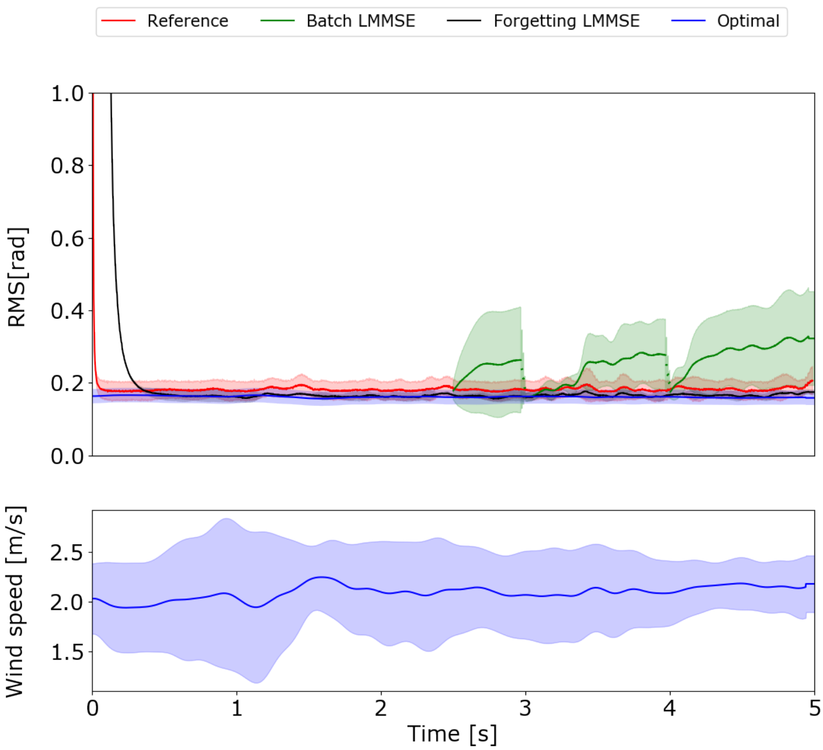

Figure 5.11: Same as Figure 5.7 but for $L_0 = 24$ m for winds according to 2006.11.22.

In the above work we have looked only at the specific case where the temporal delay is a main limiter in performance and hence the use of a LMMSE as a predictor over the time delay only. However, we can also benefit from using these algorithms when we have other dominating error terms. For an increase in a factor of 25 in measurement noise we plot the performance of our high order LMMSE predictors in Figure 5.13. We are able to perform better than the classical solution for varying winds.

5.6 Conclusions

In this paper, we model dynamic wind behavior, based on the TMT site testing data. We look at different implementations of a low order LMMSE predictor to predict atmospheric phase fluctuations over a time delay of two frames. For the stationary case, both the batch and recursive implementations perform better than a pure temporal predictor; i.e., that the current measurement is the best prediction. Under time varying turbulence, however, we loose performance due to wind speed fluctuations. For slower wind speeds and L_0 smaller than the telescope diameter, we are able to approach ideal performance with our LMMSE. The classical solution is also able to

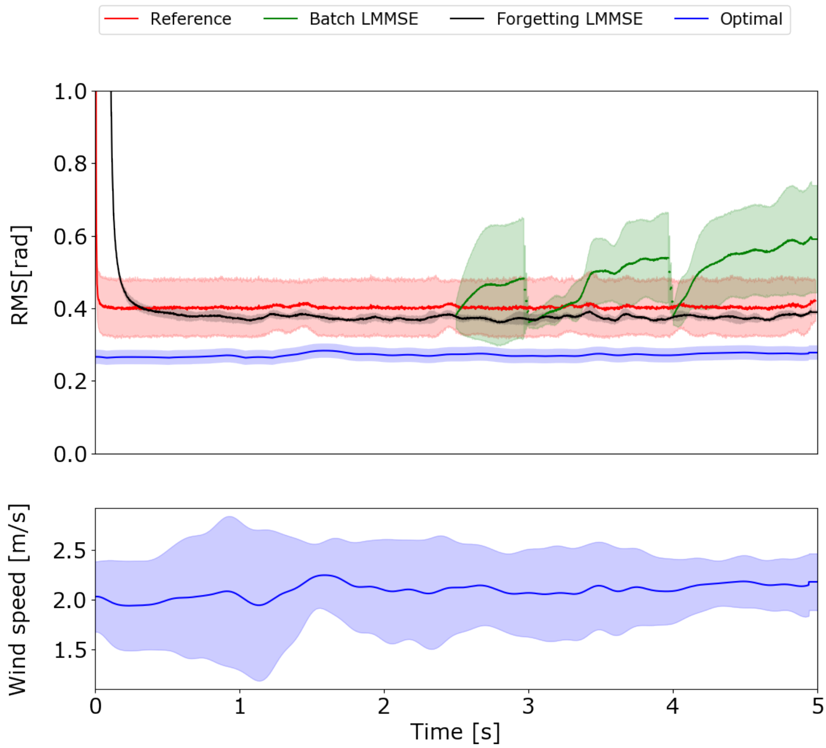

Figure 5.12: Same as Figure 5.7 but for $L_0 = 80$ m with winds according to 2006.11.22.

perform well under these conditions. As the wind speed increases, we see a larger difference between the LMMSE and the ideal solution. Eventually, for high wind speeds, the order of the spatio-temporal predictor no longer affects the performance. The lowest order LMMSE performs just as well as the higher orders. For our given spatial and temporal sampling there are conditions (smaller L_0 and wind speeds approximately m/s) in which we do reach an optimal predictor solution.

This work demonstrates that for an AO system the process of selecting and designing a predictive control framework for time varying wavefront phase fluctuations is much different than for the stationary case. In ongoing research, we are aiming at more suitable predictive control schemes that will be better able to deal with the statistical variability of atmospheric turbulence, especially for cases of high wind speed variance.

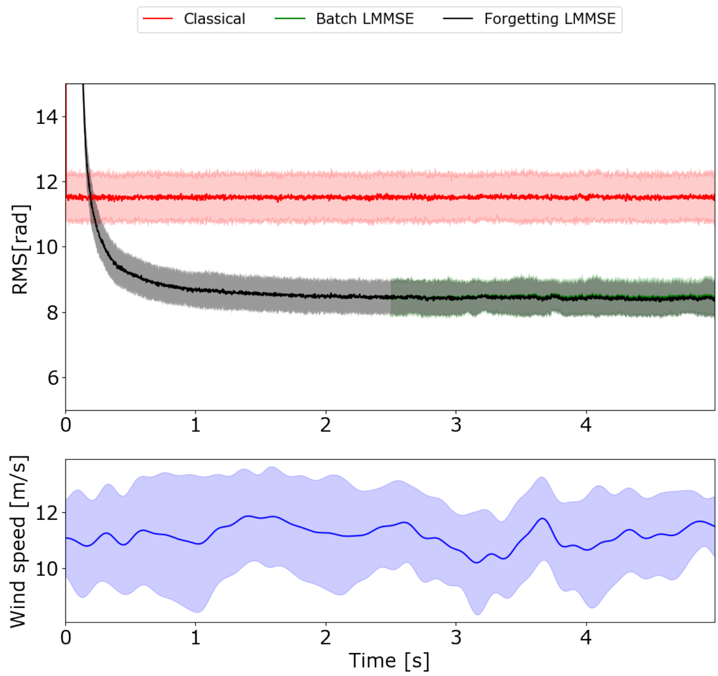

Figure 5.13: Prediction performance for the case of the noise being 0.5 times the turbulence variance.

References

Assémat, François, Richard W. Wilson, and Eric Gendron (Feb. 2006). "Method for simulating infinitely long and non stationary phase screens with optimized memory storage". In: *Opt. Express* 14.3, pp. 988–999.

Beghi, A., A. Cenedese, and A. Masiero (Dec. 2007). "Atmospheric turbulence prediction: A PCA approach". In: *2007 46th IEEE Conference on Decision and Control*, pp. 566–571.

Beuzit, J.-L. et al. (July 2008). "SPHERE: a 'Planet Finder' instrument for the VLT". In: *Proc.SPIE* 7014, p. 701418.

Brandl, B. R. et al. (Aug. 2016). "Status of the mid-infrared E-ELT imager and spectrograph METIS". In: *Proc.SPIE* 9908, p. 990820.

Cantalloube, F. et al. (2018). "Origin of the asymmetry of the wind driven halo observed in high-contrast images". In: *Astronomy & Astrophysics* 620, p. L10.

Chauvin, G., A.-M. Lagrange, C. Dumas, B. Zuckerman, D. Mouillet, I. Song, J.-L. Beuzit, and P. Lowrance (Oct. 2004). "A giant planet candidate near a young brown dwarf. Direct VLT/NACO observations using IR wavefront sensing". In: *Astronomy and Astrophysics* 425, pp. L29–L32.

Conan, R. (2000). *Modelisation des effets de l'echelle externe de coherence spatiale du front d'onde pour l'observation a haute resolution angulaire en astronomie: application a l'optique adaptative, a l'interferometrie et aux tres grands telescopes*.

Correia, C. M., K. Jackson, J.-P. Véran, D. Andersen, O. Lardière, and C. Bradley (June 2015). "Spatio-angular minimum-variance tomographic controller for multi-object adaptive-optics systems". In: *OSA* 54, p. 5281.

Doelman, Niek, Rufus Fraanje, and Remco den Breeje (2011). "OPTIMAL CONTROL OF TIP-TILT MODES on-sky adaptive optics demonstration". In: *AO4ELT* 2.

Doelman, Niek, Rufus Fraanje, Ivo Houtzager, and Michel Verhaegen (2009). "Adaptive and Real-time Optimal Control for Adaptive Optics Systems". In: *European Journal of Control* 15.3, pp. 480–488.

Gray, M., C. Petit, S. Rodionov, M. Bocquet, L. Bertino, M. Ferrari, and T. Fusco (Aug. 2014). "Local ensemble transform Kalman filter, a fast non-stationary control law for adaptive optics on ELTs: theoretical aspects and first simulation results". In: *Optics Express* 22, p. 20894.

Guyon, O. and J. Males (July 2017). "Adaptive Optics Predictive Control with Empirical Orthogonal Functions (EOFs)". In: *ArXiv e-prints*.

Hardy, J. W. (1998). "Adaptive Optics for Astronomical Telescopes". In: *Oxford University Press Jul 1998*.

Haykin, Simon (2002). *Adaptive filter theory*. 4th. Upper Saddle River, NJ: Prentice Hall.

Hinnen, Karel, Michel Verhaegen, and Niek Doelman (June 2007). "Exploiting the spatiotemporal correlation in adaptive optics using data-driven H2-optimal control". In: *J. Opt. Soc. Am. A* 24.6, pp. 1714–1725.

Jackson, Kate, Carlos Correia, Olivier Lardière, Dave Andersen, and Colin Bradley (Jan. 2015). "Linear prediction of atmospheric wave-fronts for tomographic adaptive optics systems: modelling and robustness assessment". In: *Opt. Lett.* 40.2, pp. 143–146.

Jovanovic, N. et al. (Sept. 2015). "The Subaru Coronagraphic Extreme Adaptive Optics System: Enabling High-Contrast Imaging on Solar-System Scales". In: *Publications of the Astronomical Society of the Pacific* 127, p. 890.

Kasper, Markus (2012). "Adaptive optics for high contrast imaging". In: *Proc.SPIE* 8447, pp. 8447 - 8447 –10.

Kooten, Maaike van, Niek Doelman, and Matthew Kenworthy (May 2019). "Impact of time-variant turbulence behavior on prediction for adaptive optics systems". In: *J. Opt. Soc. Am. A* 36.5, pp. 731–740.

Le Roux, B., R. Ragazzoni, C. Arcidiacono, J.-M. Conan, C. Kulcsar, and H.-F. Raynaud (Oct. 2004). "Kalman-filter-based optimal control law for star-oriented and layer-oriented multiconjugate adaptive optics". In: *Proc.SPIE* 5490, pp. 1336–1346.

Looze, Douglas P. (Jan. 2009). "Linear-quadratic-Gaussian control for adaptive optics systems using a hybrid model". In: *J. Opt. Soc. Am. A* 26.1, pp. 1–9.

Macintosh, B. et al. (Sept. 2014). "First light of the Gemini Planet Imager". In: *Proceedings of the National Academy of Science* 111, pp. 12661–12666.

Massioni, P., C. Kulcsár, H.-F. Raynaud, and J.-M. Conan (Nov. 2011). “Fast computation of an optimal controller for large-scale adaptive optics”. In: *Journal of the Optical Society of America A* 28, p. 2298.

Meerschaert, Mark M. and Farzad Sabzikar (2013). “Tempered fractional Brownian motion”. In: *Statistics and Probability Letters* 83.10, pp. 2269–2275.

Milli, J. et al. (Sept. 2017). “Performance of the extreme-AO instrument VLT/SPHERE and dependence on the atmospheric conditions”. In: *AO4ELT5*.

Otten, G. P. P. L. et al. (Jan. 2017). “On-sky Performance Analysis of the Vector Apodizing Phase Plate Coronagraph on MagAO/Clio2”. In: *The Astrophysical Journal* 834, p. 175.

Paschall, R. N. and D. J. Anderson (Nov. 1993). “Linear quadratic Gaussian control of a deformable mirror adaptive optics system with time-delayed measurements”. In: *OSA* 32, pp. 6347–6358.

Petit, C., J.-M. Conan, C. Kulcsár, H.-F. Raynaud, and T. Fusco (2008). “First laboratory validation of vibration filtering with LQG control law for Adaptive Optics”. In: *Optics Express* 16, p. 87.

Piatrou, Piotr and Michael C. Roggemann (Mar. 2007). “Performance study of Kalman filter controller for multiconjugate adaptive optics”. In: *Appl. Opt.* 46.9, pp. 1446–1455.

Por, Emiel H., Sebastiaan Y. Haffert, Vikram M. Radhakrishnan, David S. Doelman, Maaike van Kooten, and Steven P. Bos (2018). “High Contrast Imaging for Python (HCIPy): an open-source adaptive optics and coronagraph simulator”. In: *Proc.SPIE* 10703, pp. 10703 - 10703 –14.

Schock, M. et al. (2009). “Thirty Meter Telescope Site Testing I: Overview”. In: *Publications of the Astronomical Society of the Pacific* 121.878, p. 384.

Srinath, S., L. A. Poyneer, A. R. Rudy, and S. M. Ammons (Dec. 2015). “Computationally efficient autoregressive method for generating phase screens with frozen flow and turbulence in optical simulations”. In: *Optics Express* 23, p. 33335.

van Kooten, Maaike A. M., Niek Doelman, and Matthew Kenworthy (2018). “Implications for contrast as a result of the wind vector and non-stationary turbulence”. In: *Proc.SPIE* 10703, pp. 10703 - 10703 –14.

van Kooten, Maaike, Niek Doelman, and Matthew Kenworthy (Sept. 2017). “Performance of AO predictive control in the presence of non-stationary turbulence”. In: *AO4ELT5*.

Ziad, Aziz (2016). “Review of the outer scale of the atmospheric turbulence”. In: *Proc.SPIE* 9909, pp. 9909 - 9909 –12.

Chapter 6

Robustness of prediction for extreme adaptive optics systems under various observing conditions: An analysis using VLT/SPHERE adaptive optics data.

"Do not then stumble at the end of the road".

J.R.R. Tolkien, *The Two Towers*

Summary

For high-contrast imaging (HCI) systems, such as VLT/SPHERE, the performance of the system at small angular separations is contaminated by the wind-driven halo in the science image. This halo is a result of the servo-lag error in the adaptive optics (AO) system due to the finite time between measuring the wavefront phase and applying the phase correction. One approach to mitigating the servo-lag error is predictive control. We aim to estimate and understand the potential on-sky performance that linear data-driven prediction would provide for VLT/SPHERE under various turbulence conditions. We used a linear minimum mean square error predictor and applied it to 27 different AO telemetry data sets from VLT/SPHERE taken over many nights under various turbulence conditions. We evaluated the performance of the predictor using residual wavefront phase variance as a performance metric. We show that prediction always results in a reduction in the temporal wavefront phase variance compared to the current VLT/SPHERE AO performance. We find an average improvement factor of 5.1 in phase variance for prediction compared to the VLT/SPHERE residuals. When comparing to an idealised VLT/SPHERE, we find an improvement factor of 2.0. Under our 27 different cases, we find the predictor results in a smaller spread of the residual temporal phase variance. Finally, we show there is no benefit to including spatial information in the predictor in contrast to what might have been expected from the frozen flow hypothesis. A purely temporal predictor is best suited for AO on VLT/SPHERE. Linear prediction leads to a significant reduc-

This chapter has been published as: Maaike van Kooten et al. (2020). "Robustness of prediction for extreme adaptive optics systems under various observing conditions - An analysis using VLT/SPHERE adaptive optics data". In: *Astronomy and Astrophysics* 636, A81. DOI: 10.1051/0004-6361/201937076. URL: https://doi.org/10.1051/0004-6361/201937076.

tion in phase variance for VLT/SPHERE under a variety of observing conditions and reduces the servo-lag error. Furthermore, prediction improves the reliability of the AO system performance, making it less sensitive to different conditions.

6.1 Introduction

In the search for new exoplanets and earth analogs, dedicated high-contrast imaging (HCI) systems have allowed the angular separation of host stars from their surroundings to reveal cirucmstellar disks and exoplanets. The combination of extreme adaptive optics (XAO) to provide high spatial resolution, coronagraphs to suppress the host star's light, and data reduction techniques to remove residual effects, allows HCI systems to reach post-processed contrasts of 10^{-6} at spatial separations of 200 milliarcseconds (Zurlo et al., 2016). VLT/SPHERE is a HCI system that has discovered two confirmed planets: HIP 65426b (Chauvin, G. et al., 2017) and PDS 70b (Keppler et al., 2018). It has also discovered a vast array of debris, protoplanetary, and circumstellar disks (e.g., Avenhaus et al., 2018; Sissa et al., 2018). Operating with a tip/tilt deformable mirror (TTDM), a 41-by-41 high order deformable mirror (HODM), and a Shack-Hartmann wavefront sensor (SHWFS) sampling at 1380 Hz, the XAO system of VLT/SPHERE, SAXO delivers Strehl ratios greater than 90 % in the H band! (Beuzit et al., 2019).

A major challenge with VLT/SPHERE (and other HCI systems to varying degrees) is the presence of the wind-driven halo (WDH) that dominates the wavefront error at small angular separations. The WDH is a manifestation of the servo-lag error and appears as a butterfly pattern in the coronagraphic/science images (see Cantalloube et al., 2018, for details on the WDH). The servo-lag error is due to the finite time between the measurement of the incoming wavefront aberration (caused by atmospheric turbulence) and the subsequent applied correction. The resulting wavefront error is due to the outdated disturbance information and the closed-loop stability constraints. Owing to this, the halo is aligned with the dominant wind direction and severely limits the contrast at small angular separations even after post-processing techniques. The servo-lag error prevents VLT/SPHERE from achieving its optimal performance when coherence times are below 5 milliseconds (Milli et al., 2017).

The XAO system, SAXO, has a temporal delay of approximately 2.2 SHWFS camera frames. The HODM is controlled using an integrator with modal gain optimisation (Petit, Sauvage, et al., 2014). Within this framework, one solution to minimise the delay in SAXO itself is to run everything faster. However, this solution poses a number of hardware challenges with a new HODM that can run at the desired speed, a wavefront sensor camera with fast readout, and a more powerful real-time-computer. One alternative solution is to upgrade the controller with a control scheme that predicts the evolution of the wavefront error over the time delay. In this paper, we look at the potential of prediction to improve the performance of SAXO especially when the servo-lag error is the dominant residual wavefront error source (i.e., small coherence times).

Many different groups have worked on predictive control as a means of improving the performance of an adaptive optics (AO) system by minimising the servo-lag error. We highlight a few results from the last 15 years. Prediction, within the context of optimal control, is an ingredient in finding the optimal controller. Linear quadratic Gaussian (LQG) control has been explored by Petit, Conan, et al. (2008) for general AO systems to perform vibration filtering with the Kalman filter. On-sky demonstrations of the LQG controller for tip-tilt/vibrational control are provided in Sivo et al. (2014). Laboratory work to include higher order modes for atmospheric turbulence compensation (Le Roux et al., 2004) has demonstrated a reduction in the temporal error showing predictive capabilities. The H2 optimal controller (closely related to LQG) has been tested on-sky (Doelman et al., 2011) showing a reduction in the temporal error for tip-tilt control. For multi-conjugate AO systems, a temporal aspect to the phase reconstruction for each layer has been implemented; the spatial-angular predictor is formed by exploiting frozen flow hypothesis and making use of minimum mean square error estimator (with analytical expressions for the stochastic process) (Jackson et al., 2015).

Within the HCI community, there have been many efforts to incorporate prediction into the AO control algorithm. Building on Poyneer and Macintosh, 2006, predictive Fourier control, proposed in Poyneer, Macintosh, and Véran, 2007, makes use of Fourier decomposition and the closed-loop power spectral density (PSD) to find components due to frozen flow. Using Kalman filtering a predictive control law is determined resulting in a reduction of the servo-lag error. Other methods in HCI have focused on splitting the prediction step from the controller. This is done by first estimating the pseudo-open loop phase (slopes, or modes), applying a prediction filter, and then controlling the HODM using the predicted phases as input into the controller. This approach allows for a system architecture that can turn prediction on and off without affecting the control loop. A similar structure has been implemented using the CACAO real-time computer (Guyon, Sevin, et al., 2018). Empirical orthogonal functions (EOF) is a data-driven predictor that aims to minimise the phase variance. Implemented on SCExAO (an HCI instrument at the Subaru telescope using the CACAO real-time computer) it has been demonstrated (Guyon, Sevin, et al., 2018) that EOF improves the standard deviation of the point-spread-function over a set of images. However, the improvement is less than expected from initial simulations (Guyon and Males, 2017). Similar methods minimise the same cost function as EOF but with a different evaluation of the necessary covariance functions (see Section 6.3.1) as reported in Kooten et al. (2019) and Jensen-Clem et al. (2019). Current a posteriori tests, using AO telemetry (Jensen-Clem et al., 2019), show an average factor of 2.6 improvement for contrast for separations from 0 to 10 λ/D. This approach to prediction will be implemented at the Keck telescope. One benefit to separating the prediction and the control steps is that the behaviour of the input disturbance (atmospheric induced phase fluctuations) can be studied for a given system and telescope site location, along with tests performed with AO telemetry data. We take this approach in this work, building on our earlier work (Kooten et al., 2019), looking solely at the predictability of the pseudo open-loop slopes under various atmospheric conditions. Previous work on prediction in the AO community has focused on one or two case(s) on-sky for demonstrations of prediction, successfully showing the feasibility of predictive control. We look at how a linear minimum mean square error (LMMSE) predictor performs a posteriori on VLT/SPHERE AO telemetry data under a large set of various observing conditions (such as guide star magnitude, coherence time, and seeing conditions).

We organise this paper as follows: we introduce and summarise our SAXO data set in Section 6.2. In Sec 6.3 we outline our methodology, including the structure of our predictor (Section 6.3.1). We elaborate on how we apply the predictor to the VLT/SPHERE SAXO telemetry data and we present our results in Section 6.4, discussing them in Section 6.5. We look at how the predictor performs under different conditions as well as the stationarity of the turbulence. The implications of the results are discussed in Section 6.5.4, concluding in Section 6.6 including future research directions.

6.2 SAXO data

The SAXO system has the option to save the full (or partial) XAO telemetry, including HODM positions, SHWFS slopes, SHWFS intensities, interaction matrix, at the discretion of the instrument user. In this paper, we make use of 27 SAXO data sets taken between 2017 and 2019. By limiting ourselves to these years we also have estimations of the atmospheric conditions (seeing, coherence time, and turbulence

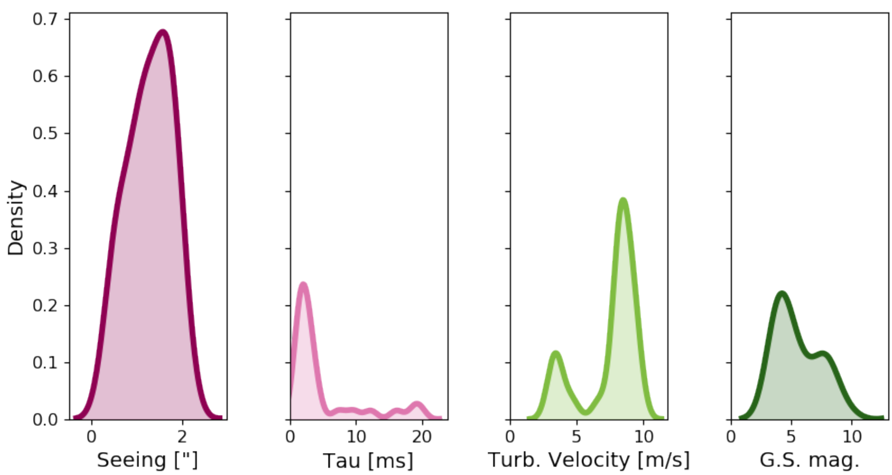

Figure 6.1: Kernel density functions for the seeing, coherence time, turbulence velocity, and guide star magnitude (r band) showing the conditions under which the VLT/SPHERE telemetry was taken. The first three panels are measurements closest to the time of the observation output by the MASS-DIMM (accessed via ESO Paranal query form). The corresponding targets were found at the VLT/SPHERE ESO archive and their r-band magnitudes were found in the VizieR catalog. The kernel density functions are a non-parametric estimation of the probability functions.

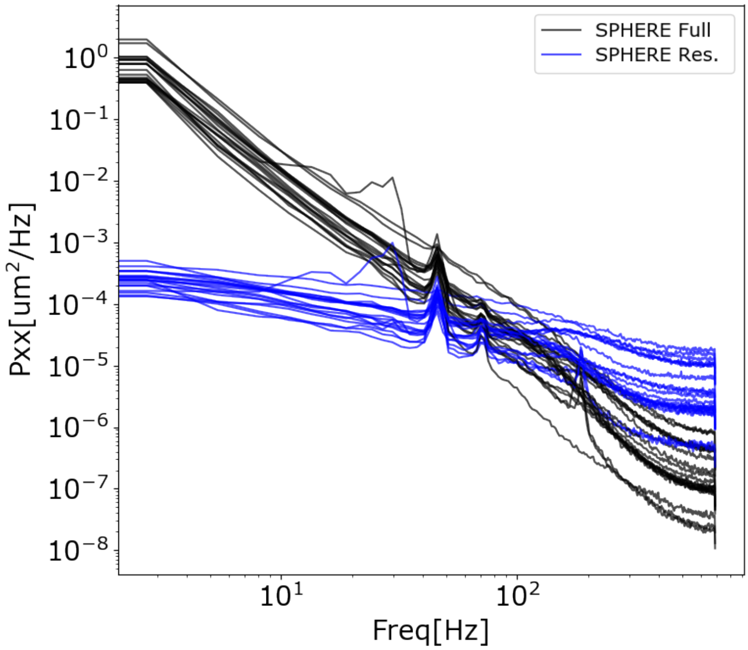

Figure 6.2: Power spectral densities, estimated using the Welch method, for all the data sets; both for the full VLT/SPHERE estimated pseudo open-loop phases and for the reconstructed VLT/SPHERE residual phases.

velocity) from the MASS-DIMM instrument located approximately 100 meters away from UT4, which houses the VLT/SPHERE instrument. The conditions under which our data were acquired are summarised in Figure 6.1, where we plot the kernel density functions estimated from the data. We note that the data set is biased toward shorter coherence times (tau), where the median coherence time are 2.5 milliseconds; from Milli et al. (2017) and Cantalloube et al. (2018) we expect the WDH to be dominant (and thereby the servo-lag error) when the coherence time drops below 5 milliseconds. For completeness, the data set has a couple of data sets with longer coherence times. The turbulence velocity is the velocity of the characteristic turbulent layer as determined by the MASS-DIMM instrument and is associated with a characteristic altitude determine from the atmospheric profile. Therefore, it does not necessarily indicate the speed of the jet stream layer but provides a tracer atmosphere velocity. For most of the data we have bright guide star magnitudes with a mean of 5 magnitudes in the r band (the wavefront sensor bandwidth), resulting in high signal-to-noise ratios (S/N) for the SHWFS in all cases. The seeing has a Gaussian-like distribution with a mean of 1.3 arc-seconds. A full summary of the entire data set (including time of observation) is provided in Table 6.2 in the Appendix. Each of the 27 data sets differ in length and range from 10 to 60 seconds, allowing us to probe different conditions while still having the opportunity to observe the behaviour of turbulence on timescales of a minute.

To study the influence of prediction on our data sets, we estimated the pseudo-open loop phases, thereby applying prediction to the zonal two-dimensional grid of phase values and not the modes. We performed the open-loop estimation using the HODM commands only because SAXO saves the full HODM voltages, not just the updates (see Appendix 6.B). We converted to phase using the standard SAXO HODM modes. As a result, we neglected the spatial frequencies beyond the spatial bandwidth of the HODM and therefore underestimated the open-loop phase at higher spatial frequencies. We took this approach after first considering the more traditional method of using the wavefront sensor measurements and unravelling the pseudo open-loop phase from the SHWFS measurements and knowledge of the controller state. Without full knowledge of the modal gains and controller at each time step, as in our case, this method provides an inaccurate estimation.

In Figure 6.2, we plot the resulting PSDs for the final pseudo open-loop phase from the VLT/SPHERE telemetry (SPHERE full) and the closed-loop phase of VLT/SPHERE residuals and identify some key features. There are peaks around 40 Hertz and 60 Hertz in both the open and closed-loop PSDs. Performing a modal analysis we find that the peaks appear for Zernike modes 7-11 (Noll indexing; Noll, 1976) with varying amplitudes. The second feature is the increase in power at high temporal frequencies for the closed-loop PSD (i.e., the so-called waterbed effect, a result of Bode's sensitivity integral).

6.3 Methodology

Although we are ultimately interested in the improvement in contrast using prediction, we limit ourselves in this work to studying the minimisation of the servo-lag error. From Guyon (2005), Kasper (2012), and Cantalloube et al. (2018), we see that minimising the lag results in an improvement in contrast but ultimately also depends on the coronagraph of choice and how it interacts with the residual phase at small angular separations. We also do not have focal plane images taken at the same time as the data sets, making a clear claim of improvement unreliable. The metric we adopt is the temporally and spatially averaged wavefront phase variance.

6.3.1 LMMSE prediction

For our predictor we chose a data-driven method called the LMMSE predictor. This approach provides a flexible framework that allows us to implement the predictor in three different ways: batch, recursive, and with an exponential forgetting factor (Kooten et al., 2019).

A single point i of a phase screen at time t is given by $y_i(t)$, while $\vec{u(t)}$ is a $P^2 \times 1$ column vector containing a collection of P^2 phase values on a discrete spatial grid at time t. We assume that the future value of a given phase point, $\hat{y}_i$ at the discrete time index $t+d$, is a linear combination of the most recent phase values at time t. The predictor coefficients are denoted as $\vec{a}_i$. The cost function of our predictor, with

<> $_t$ as the time average operator, is then

$$min_{\vec{a}_i} < ||y_i(t+d) - \vec{a}_i^T \vec{w}(t)||^2 >_t, \tag{6.1}$$

where $\vec{w(t)}$ includes a set of Q most recent measurements,

$$\vec{w(t)} = \left(\vec{u}(t)^T \quad \vec{u}(t-1)^T \quad \vec{u}(t-2)^T \quad \ldots \quad \vec{u}(t-Q)^T\right)^T. \tag{6.2}$$

We allowed for both spatial and temporal regressors gathered into $\vec{w(t)}$ – a $P^2Q\times1$ vector. We denoted predictors of various orders by indicating the spatial order P (spatially limiting ourselves to a box of order P, symmetric around the phase point of interest, resulting in P^2 spatial regressors) followed by the temporal order Q; for example, a 's5t2' predictor has $P=5$ and $Q=2$.

Solving Equation 6.1 for our zero-mean stochastic process, the solution can be written in terms of the inverse of the auto-covariance matrix and cross-covariance vector (Haykin, 2002).

$$\vec{a}_i = \mathbf{C}^+_{\vec{w}\vec{w}} \vec{c}_{\vec{w}y_i}, \tag{6.3}$$

where + denotes a pseudo inverse; $\mathbf{C}_{\vec{w}\vec{w}}$ is the auto-covariance matrix of $\vec{w}$, the vector containing the regressors; and $c_{\vec{w}y_i}$ is the vector containing the cross-covariance between the true phase value, y_i and $\vec{w}$.

We can estimate the covariances in Equation 6.3 directly from a training set, forming a fixed batch solution. Alternatively, we can form a recursive solution making use of the Sherman-Morrison formula (a special case of the Woodbury matrix inversion lemma). In Equation 6.4 through to Equation 6.6 we inserted the exponential forgetting factor in the update in the following equations, thereby forming our final LMMSE implementation. The recursive form is given in Equations 6.4 and 6.5 with $\lambda=1$, such that all previous data is weighted equally, as follows:

$$\vec{c}_{\vec{w}y_i}(t-d) = \lambda \vec{c}_{\vec{w}y_i}(t-d-1) + \vec{w}(t-d) y_i(t-d) \tag{6.4}$$

$$\mathbf{C}^+_{\vec{w}\vec{w}}(t-d) = \lambda^{-1} \mathbf{C}^+_{\vec{w}\vec{w}}(t-d-1) - \vec{k}(t-d) \tag{6.5}$$

with

$$\vec{k}(t-d) = \frac{\lambda^{-2}\mathbf{C}^+_{\vec{w}\vec{w}}(t-d-1)\vec{w}(t-d)\vec{w}^T(t-d)\mathbf{C}^+_{\vec{w}\vec{w}}(t-d-1)}{1+\lambda^{-1}\vec{w}^T(t-d)\mathbf{C}^+_{\vec{w}\vec{w}}(t-d-1)\vec{w}(t-d)}. \tag{6.6}$$

By updating Equations. 6.4 and 6.5, the coefficients can be found for each time step using Equation 6.3. The recursive solution goes on-line immediately with the initial auto-covariance being set to diagonal matrices with large values (as done with recursive least-squares methods) and the cross-covariance vector set to ones. By adjusting the forgetting factor, we can weigh old data by less compared to the most recent measurements, therefore allowing the tracking of slowly varying signals.

6.3.2 Comparison with EOF

Methods such as LMMSE and EOF (see Guyon and Males (2017)) and similar techniques (see Jensen-Clem et al., 2019) all minimise the same cost function, but the evaluation of Equation 6.3 is different in each case; we note that the cost function is slightly different when including exponential forgetting factor. In EOF, the solution is estimated with the inverse of the auto-covariance determined using a singular-value-decomposition that is re-estimated on minute timescales. The amount of data used to estimate the prediction filter, the numerical robustness, the noise properties of the system, and the atmospheric turbulence above the telescope all contribute to the performance of these algorithms and the final computational load. Therefore one implementation might be more suited for specific conditions than the other, but the three methods can, in ideal conditions, result in the same performance.

6.3.3 Applying prediction to SAXO telemetry

From the estimated open-loop phases (which results in a 240-by-240 phase screen using the HODM modes) we bin the data to 60-by-60 phase screens for computational memory purposes. We then performed prediction on the estimated open-loop phases assuming a 2-frame delay. For each phase point, we estimated a unique set of prediction coefficients using the equations as outlined in Section 6.3.1. Our aim is to focus on the prediction capabilities, ignoring the control aspect by assuming a perfect system – no wavefront sensor noise and a HODM that can perfectly correct all spatial frequencies predicted – and only including the delay. We note that this results in no fitting error, no spatial bandwidth limitations, and no temporal bandwidth limitations on the achievable performance.

We ran batch, recursive, and forgetting (with $\lambda = 0.998$ as this value gives the best performance assuming $\lambda \neq 1$) LMMSE predictors for each prediction order. We then subtracted the predicted phase from the pseudo open-loop phase 2 frames later resulting in the residual predictor phase. From the phases we calculated the averaged phase variance by taking the final 5 seconds of the data set, and therefore, all the different predictors have converged; we calculated the spatio-temporally averaged phase variance. We started with the performance of a s1t1 predictor. The s1t1 is a zero-order predictor because it only makes use of the most recent measurement for that given phase point, making it analogous to an optimised integrator (with a gain close to unity) in our simulations; we refer to the s1t1 as the ideal VLT/SPHERE performance.

We performed simulations testing a variety of predictors with different spatial and temporal orders including s1t3, s1t10, s3t1, and s3t3. We looked at how the three different implementations of the LMMSE for each prediction order behave (see Figure 6.3). In Section 6.4 we present the results for the recursive s1t10 predictor, which performs the best out of all the different orders.

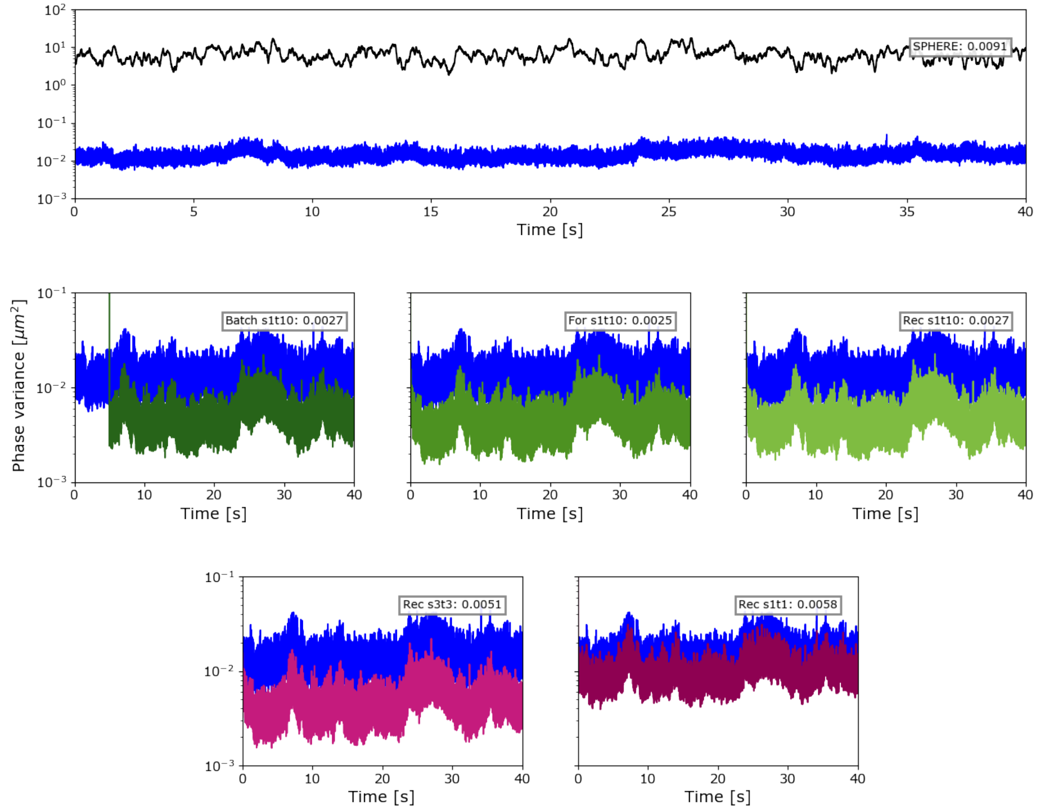

Figure 6.3: In the top panel, we plot a time series showing the estimated pseudo open-loop in black, compared with the VLT/SPHERE residual in blue for a random SAXO telemetry data set. The other plots (all with the same y-scale) show various predictor residual phase variances (various green and purple lines) compared to the VLT/SPHERE residuals for the same data. The averaged phase variance, in μm^2, for the last 5 seconds is indicated in the top right corner of each plot. The forgetting s1t10 (abbrev. for) does not perform significantly better than the recursive s1t10 (abbrev. res). Secondly, the s3t3 does not perform better than the s1t10.

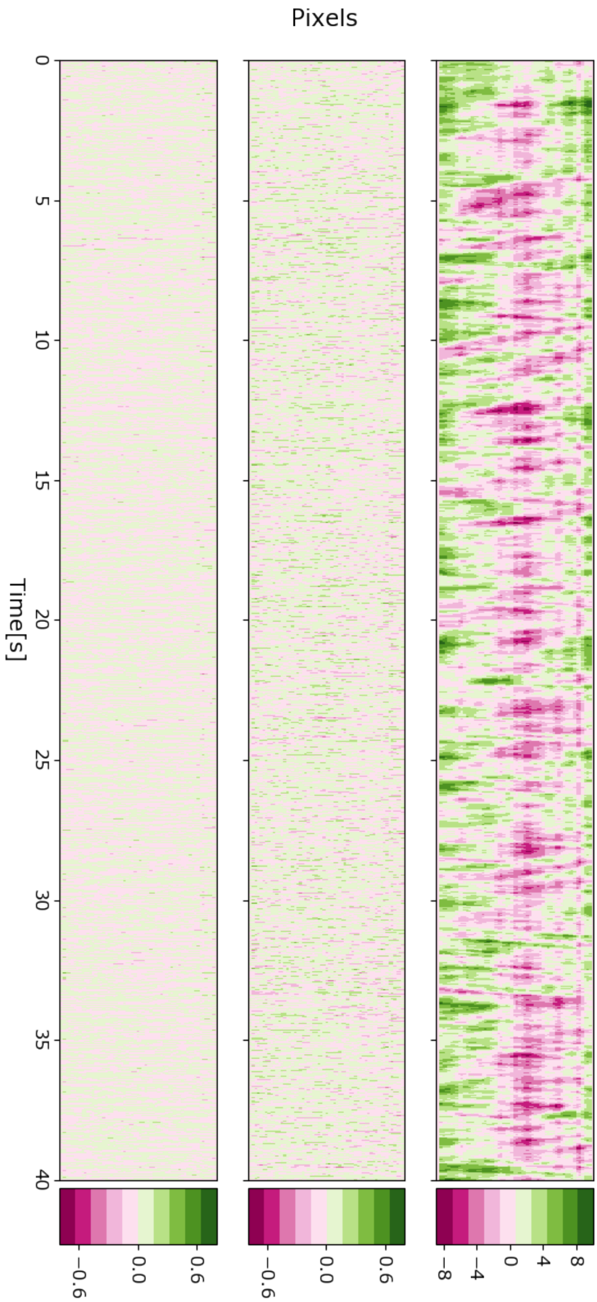

Figure 6.4: Vertical slice across the telescope aperture (y-axis) showing the wavefront phase in μm (indicated by the colour-bars), plotted as a function of time for the pseudo open-loop phase (top), the VLT/SPHERE residual phase (middle), and s1t10 predictor residual phase (bottom) for the same night as Figure 6.3. Comparing the bottom two panels (colour map is the same in both), we can see the prediction residuals have a flatter and more uniform appearance compared to the real VLT/SPHERE residuals.

6.4 Results

We find that prediction provides a reduction in averaged phase variance when compared to the VLT/SPHERE SAXO residuals. An example of how prediction behaves spatially and temporally for a slice across the telescope aperture is shown in the bottom panel of Figure 6.4. We see a reduction in the phase compared to the VLT/SPHERE residuals and see a more uniform solution in time and space. In Figure 6.5 we summarise the results of running prediction on all of our data sets. As mentioned above, the averaged phase variance is found by using the last 5 seconds of the data. The data sets all vary in length. When we see a reduction in the residual phase variance, we would expect an improvement of performance for the XAO system for all cases independent of the guide star magnitude, the seeing, and the coherence time. We observe a reduction in the spread of residual phase variance, with prediction providing a more uniform performance for various conditions; see the kernel density function plots in the top panel of Figure 6.5.

In Figure 6.6 we plot the ratio of the recursive s1t10 predictor residual phase variance to the VLT/SPHERE residual phase variance defining this as the "ratio of

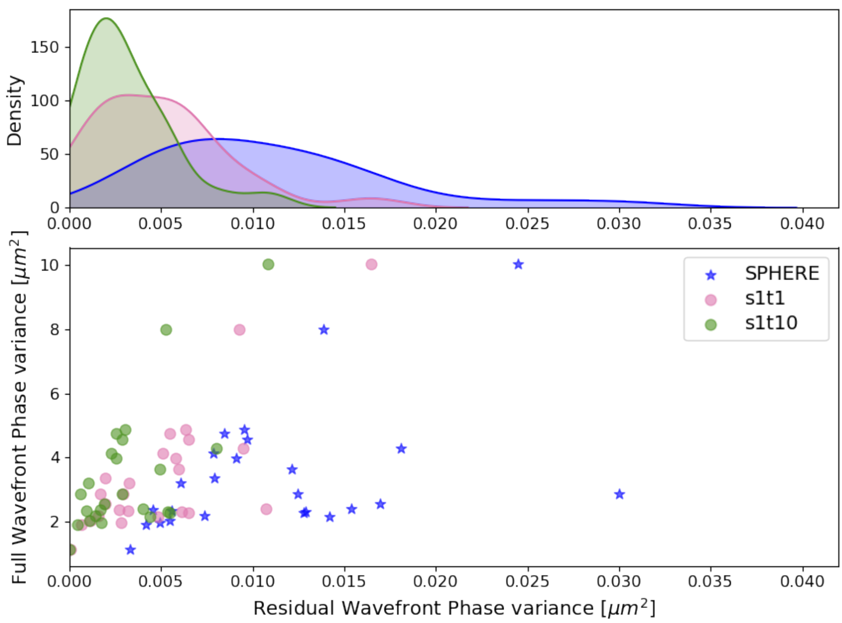

Figure 6.5: Top: Kernel density function estimation for the averaged phase variances plotted in the bottom plot. The change in spread of the values is shown. Bottom: Pseudo open-loop averaged wavefront phase variance compared to residual averaged wavefront phase variance for VLT/SPHERE, a batch s1t1 (i.e., idealised integrator for VLT/SPHERE), and a recursive s1t10 predictor. The points move from right to left, indicating that a s1t1 does better than VLT/SPHRE and a high order predictor does even better than the s1t1.

improvement” as a function of coherence time. In the same figure, we add the ratio of improvement for the same recursive s1t10 predictor and an idealised VLT/SPHERE integrator (batch s1t1) against coherence time. We calculate the average ratio of improvement to be 5.1 and 2.0, respectively. Figure 6.6 shows the relative seeing conditions indicated by the size of the marker; smaller marker sizes indicate better seeing conditions.

We evaluate several predictors, varying both spatial and temporal orders. We find that there is no gain in performance by adding spatial regressors and find that temporal regressors perform equally as well. These results are summarised in Table 6.1.

We see minimal evidence of non-stationary behaviour of optical turbulence. First, by looking at the coherence times in Table 6.2, we do not see significant change in coherence time for data taken on the same night – showing that on 100 seconds time scales the statistics of optical turbulence do not vary significantly. Second, on shorter timescales, we do not see evidence of non-stationary turbulence. In Figure 6.3, we plot the batch, recursive, and the forgetting LMMSE for a s1t10 predictor. From the average residual phase variances, we see that the batch and recursive perform the same over the full 40 second period. We do see a slight improvement for the forgetting LMMSE, implying a slight time-variant behaviour of the pseudo open-loop phase but nothing significant.

6.5 Discussion

6.5.1 Comparison of the prediction residuals to the VLT/SPHERE residuals

We should note the difficulties in performing a direct comparison between the predictor residuals to the real VLT/SPHERE residuals. There are a few challenges, with the first being a difference in delay. In our estimation of the open-loop phase we choose

Table 6.1: Averaged phase variance for the pseudo open-loop, VLT/SPHERE residuals, s1t3 residuals, s3t3 residuals, and the s3t1 residuals. Comparing the last three columns, there is no gain by including spatial regressors to the prediction algorithm and the s1t3 does better than the s3t3.

Time of data on 2017-07-19	Pseudo open-loop $[\mu m^2]$	VLT/SPHERE $[\mu m^2]$	s1t3 $[\mu m^2]$	s3t3 $[\mu m^2]$	s3t1 $[\mu m^2]$
22:54:55.000	1.963	0.005	0.002	0.002	0.002
23:16:39.000	2.856	0.012	0.001	0.001	0.002
23:22:02.000	2.400	0.015	0.004	0.004	0.011
23:50:33.000	2.148	0.014	0.004	0.004	0.005

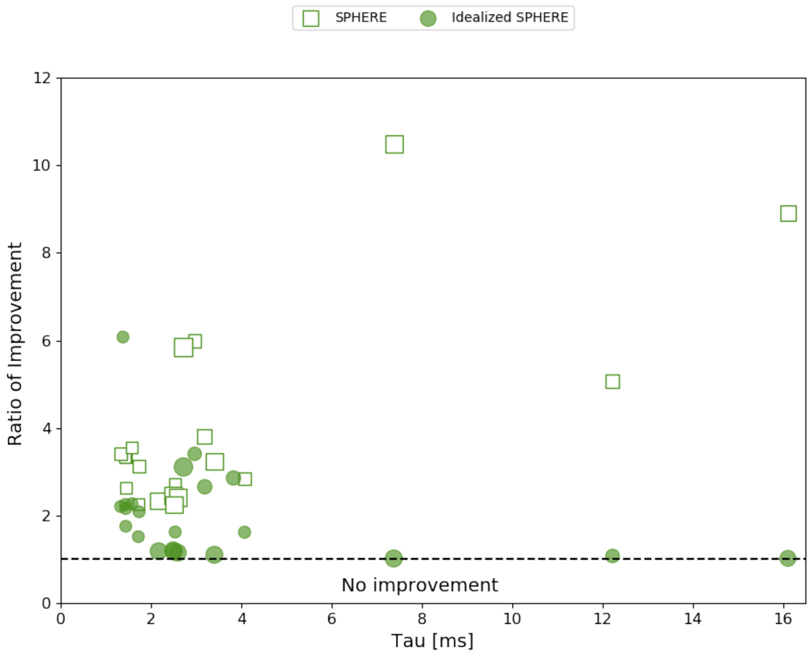

Figure 6.6: Ratio of improvement, found by taking the ratio of an idealised integrator on VLT/SPHERE to a recursive spatial-temporal predictor (s1t10) phase variance as calculated from the last 5 seconds of data, as a function of coherence time. The size of the markers indicates the MASS-DIMM seeing conditions at the time of observation. The average ratio of improvement is 5.1 when comparing the prediction to the real VLT/SPHERE residuals. When looking at the idealised VLT/SPHERE, we find an average ratio of improvement of 2.0 in wavefront variance reduction.

to round the frame delay to a whole frame; therefore our predictor sees a delay of 2 frames (or 1.45 milliseconds) while the real system delay, and thereby encoded in the real VLT/SPHERE residuals, is 2.2 frames (1.59 milliseconds). We therefore assume that the VLT/SPHERE residuals immediately have a larger phase variance compared to the case where the true delay is 2 frames. An alternative option to rounding the delay frames is to interpolate, which is a step that would have also introduced an error. We make use of the HODM commands which are saved as the total voltage on the HODM, not the update to the HODM. The SHWFS, however, is used to determine the real VLT/SPHERE residuals and therefore see higher order spatial frequencies, potentially increasing the residuals if this was not the case. Perhaps the most substantial contribution to the final performance of VLT/SPHERE results from the fact that the VLT/SPHERE performance will be limited by operational parameters. The controller will need to be stable and robust on-sky, potentially resulting in a loss of performance when compared to our idealised situation. Therefore, in Figures 6.5 and 6.6 we plot the idealised VLT/SPHERE (batch s1t1) as well as the VLT/SPHERE residuals. The true gain in prediction will be between the idealised VLT/SPHERE and real VLT/SPHERE residuals and the ratio of improvement will fall between 5.1 and 2.0.

6.5.2 Performance under different conditions

Our data set and analysis is unique, showing that with prediction, there will be an improvement under almost all conditions even for long coherence times, and no loss in performance with prediction is observed. However, the data set does not show any clear correlations between predictor performance and observational conditions (see Figures. 6.6 and 6.7). We briefly discuss the behaviour for various observing parameters including coherence times, turbulence velocity, seeing, and finally guide star magnitudes.

Looking closely at Figure 6.6 and the behaviour for various coherence times we do not find any correlation between the coherence time and performance for the true VLT/SPHERE residuals. However, when looking at the idealised VLT/SPHERE behaviour we see, at smaller coherence times, an exponential-like gain in the ratio of improvement in which the asymptote is the Nyquist sampling frequency ($2/WFS_f = 2/1380 = 1.45ms$). This behaviour for the idealised case is as expected, where we have a larger improvements for shorter coherence times. We then look at the relation between the ratio of improvement and turbulence velocity (middle plot of Figure 6.7). We expect a similar behaviour to that of the coherence time as they are related. We note that we also see no correlation for the ground layer wind speeds measured by the nearby meteorological tower. Studying the relation between the seeing and the ratio of improvement we notice an asymptotic behaviour where the ratio improves for better seeing conditions. We do not see any dependence between performance and S/N (or guide star magnitudes; left plot of Figure 6.7). For the VLT/SPHERE residuals, the lack of correlation between performance and S/N is as expected from laboratory and on-sky validation of SAXO by Fusco et al., 2016 at these guide star magnitudes. We also note that for long coherence times VLT/SPHERE is often looking at fainter targets since the conditions are ideal. This is the case for our data as well (see Table 6.2). In summary, we see a relation between the true VLT/SPHERE residuals and the seeing, but for the idealised VLT/SPHERE case we see a relation between the improvement and the coherence time, as expected. The lack of correlation between ratio of improvement and the other observing parameters could be a result of the different locations of VLT/SPHERE and MASS-DIMM (which measures the observing parameters) and that the values determined over minute averages do not reflect the exact values at the time of observation. Alternatively, the behaviour of the SAXO controller is limited by internal system requirements (such as vibration rejection) and not the observing conditions, resulting in a lack of correlation between observing conditions and gain in performance.

Studying Figure 6.6, we can see that the ratio of improvement when using idealised VLT/SPHERE as a benchmark behaves very differently than the true VLT/SPHERE case. For a direct comparison to VLT/SPHERE, we do not see any correlations between the ratio of improvement and the coherence time. However, for the

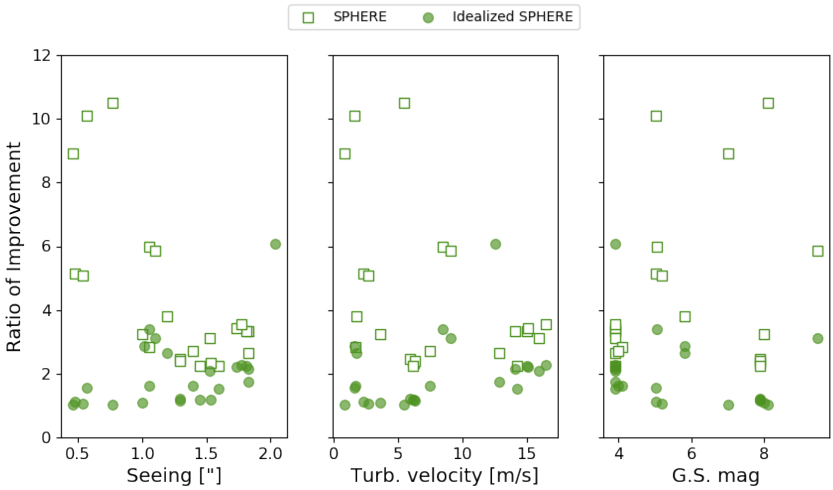

Figure 6.7: Ratio of improvement compared to seeing (left), turbulence velocity (middle), and guide star magnitude in r band (right) during the time of observation.

idealised case, we see that at longer coherence times we have no improvement since the SAXO XAO system can already perform well.

6.5.3 Time-invariant turbulence statistics

Observing the behaviour of the three (batch, recursive, and exponential forgetting) implementations of the LMMSE, we can comment on the stationarity of the turbulence. The LMMSE finds the optimal prediction coefficients determined from the training set. The batch is trained on the first 5 seconds and the recursive trains continuously. We note the residual phase variances for the last 5 seconds for each case; we do not see a significant difference between the batch and recursive solutions in any case, indicating the statistics of the turbulence has not changed over the measurement period. Studying the recursive solution, we look at the behaviour of the prediction coefficients in time across the aperture. We do not see any notable changes over the entire period once the solution has converged. We do see more fluctuations in the prediction coefficients for phase points located on the edges with a predictor using spatial information such as the s3t3. Conversely, the exponential forgetting LMMSE does show a slight improvement, however, this could be due to noise in the system that the LMMSE predictor can and does remove.

6.5.4 Implications of results

For all conditions we see an increase of performance with prediction when compared to the VLT/SPHERE residuals, under an idealised assumption there are a few cases where the ratio of improvement is one, indicating no gain but also, notably, no loss in performance.

A more notable result is from the kernel density functions plotted in the top panel of Figure 6.5. The spread of the averaged phase variance is less for the s1t10 predictor, indicating a more uniform performance in phase variance reduction for different observing conditions. From an observational point of view, having a more stable correction under different conditions is desirable, especially for the cases on surveys in which observers might be targeting similar objects and can perform reference star differential imaging from a library.

The ratio of improvement we find is 5.1, but this is probably an overestimate of the improvement we could achieve on-sky. In previous prediction work, Guyon and Males (2017) show an improvement of 7 in root-mean-square (rms) residual wavefront error while offline telemetry tests by Jensen-Clem et al. (2019) show a factor of 2.5 rms wavefront error; we note that the errors in both of these works refer to systems located on top of Mauna Kea. Although an exact direct comparison using these values is impossible, we note that we show a more modest predictive improvement compared to these studies.

When studying the prediction order we do not see a large gain from including spatial information. This is due to large sub-aperture size and the high rate of temporal sampling, which results in the turbulence only moving across a sub-aperture after many frames; for example, assuming 10 m/s and 0.2 m sub-aperture size, it takes approximately 28 frames before a cell of turbulence moves to the next sub-aperture. The turbulence is still dynamic but we sense the average variations that fall within the wavefront sensor sub-aperture. We have much finer temporal sampling. We expect a temporal-only predictor to be best suited for HCI, and by removing the spatial information, we are no longer sensitive to wind direction (spatial solution requires a symmetric choice of regressors) which therefore reduces the computational size of the prediction problem.

We do not see evidence of time-invariant turbulence, meaning that our predictor does not need to be able to track changes in turbulence behaviour on timescales less than 1-2 minutes of observations. We see a slight increase in performance from the exponential forgetting factor LMMSE solution but the difference is very slight and not substantial enough to suggest this as the best choice. From a computational point of view, the batch LMMSE is the best option and resetting it every 1 to 2 minutes (or as needed based on longer telemetry data) using 5 seconds of training data would be the best implementation.

6.6 Conclusions and future work

We find a reduction in the phase variance in comparison to the VLT/SPHERE residuals and determine the ratio of improvement to be 5.1 for SAXO telemetry data. When prediction is compared to an idealised VLT/SPHERE system, we find an improvement ratio of 2.0. In all cases, no matter what the observing conditions, prediction performs well with no loss in performance. Most importantly, we note that under all the 27 various observing conditions studied, we see a reliable and overall more consistent improvement of the system performance. The data set, in combination with our predictors, reveals that the optical turbulence as seen by the telescope is time-invariant and that the temporal regressors have a larger impact on the performance of the predictor than spatial regressors. We recommend a batch (updating every few minutes as necessary) temporal-only predictor for the VLT/SPHERE to reduce the servo-lag error. In future work we will seek to investigate the effects of prediction on contrast for different types of coronagraphs and to determine whether predictive control can be used to directly optimise the raw contrast.

6.A Overview of SAXO data

In this Appendix we provide a full summary of our data set. The XAO telemetry data is stored on the SAXO server and a log of when AO data was taken can be found on the ESO science archive under the VLT/SPHERE instrument. The 2019 data was kindly provided to us by Markus Kasper while the other data sets were accessed by Julien Milli.

Table 6.2: Summary of the VLT/SPHERE data used in this work as well as the MASS-DIMM atmospheric conditions as recorded closest to the measurement time. The target r-band magnitude is provided as to provide a relative estimation of the signal-to-noise ratio for the wavefront sensor. The length of the telemetry data ranges from 10 to 60 seconds.

Date	Seeing["]	Tau[ms]	Turbulence Velocity [m/s]	Guide star Magnitude r-band
2017-07-17T23:15:30.000	1.708	1.539	8.340	3.910
2017-07-17T19:07:58.000	2.037	1.381	-	3.910
2017-07-17T23:00:24.000	1.829	1.442	8.450	3.910
2017-07-17T23:02:51.000	1.827	1.443	8.450	3.910
2017-07-17T23:04:41.000	1.825	1.444	8.450	3.910
2017-07-17T23:10:31.000	1.812	1.434	8.450	3.910
2017-07-17T23:11:54.000	1.739	1.330	9.210	3.910
2017-07-17T23:29:56.000	1.776	1.579	9.280	3.910
2017-07-17T23:31:11.000	1.599	1.722	8.300	3.910
2017-07-17T23:33:29.000	1.524	1.738	7.970	3.910
2017-07-19T22:54:55.000	1.053	4.075	7.990	4.110
2017-07-19T23:16:39.000	1.014	3.829	9.120	5.819
2017-07-19T23:22:02.000	1.197	3.193	8.760	5.819
2017-07-19T23:50:33.000	1.001	3.406	9.700	8.010
2018-04-04T03:06:15.000	1.059	2.970	0.000	5.060
2018-04-04T03:12:50.000	1.099	2.721	0.000	9.480
2016-05-21T08:23:42.000	1.396	2.538	6.65	4.00
2016-05-21T09:29:07.000	1.533	2.171	8.16	7.890
2016-05-21T09:53:34.000	1.298	2.495	9.31	7.890
2016-05-21T09:55:48.000	1.292	2.596	9.03	7.890
2016-05-21T09:58:02.000	1.452	2.510	8.31	7.890
2019-01-26T01:49:48.00	0.770	7.381	3.39	8.110
2019-01-26T02:08:25.00	0.710	9.596	3.39	6.560
2019-01-26T03:34:39.00	0.460	16.113	4.65	7.017
2019-01-26T03:48:01.00	0.570	19.643	3.1	5.020
2019-01-26T04:59:53.00	0.480	18.774	3.67	5.020
2019-01-26T06:39:57.00	0.540	12.228	7.81	5.180

6.B Estimation of open-loop phase

In this Appendix, we explain how the SAXO VLT/SPHERE telemetry data is used to estimate the pseudo open-loop phase, providing an estimation of the open loop phase of the wavefront at the pupil plane due to atmospheric turbulence. Usually the pseudo-open loop phases are estimated using wavefront sensor data and controller state (deformable mirror updates, gain, and interaction matrix). Specifically, by summing the measured wavefront sensor phase and the previous deformable mirror updates, an estimation of atmospheric phase can be made. We make make use of an alternative method using the HODM for which we have the full voltages applied to the mirror. Spatially, the HODM has comparable sampling to the SHWFS (41-by-41 actuators versus 40-by-40 sub-apertures) and therefore using the HODM for estimating the open-loop phase does not restrict the spatial bandwidth. Similarly, the temporal bandwidth of the system is determined by SHWFS frame rate, while the temporal bandwidth of the HODM is much higher. By using the HODM we do not lose any spatial or temporal bandwidth.

From Figure 6.2, we can see that the SAXO provides a good correction for our data sets, as expected, therefore the HODM surface is representative of the full atmospheric phase. We assume the residual errors are negligible owing to the high expected Strehl ratio for our conditions (80-90% in the H band, see Fusco et al., 2016). From Fig. 6.2, we also see that the closed-loop PSDs estimated from the wavefront sensor residuals are relatively flat, indicating a good correction. We can then take the HODM surface as representative of the full atmospheric phase. In an open-loop system, the full atmospheric phase is measured by the wavefront sensor and then used to determine the deformable mirror commands. The surface of the deformable mirror therefore represents the estimated open-loop phase of the wavefront in the pupil plane. It can be expressed in the form of a lifted vector as

$$y(t) = DM_{surface}(t), \tag{6.7}$$

where $DM_{surface}(t)$ is a $41^2 \times 1$ vector.

Therefore, using a posteria data, since we know the full voltage on the DM surface we can estimate the pseudo open-loop phase.

References

Avenhaus, Henning et al. (Aug. 2018). “Disks around T Tauri Stars with SPHERE (DARTTS-S). I. SPHERE/IRDIS Polarimetric Imaging of Eight Prominent T Tauri Disks”. In: *The Astrophysical Journal* 863.1, p. 44.

Beuzit, J.-L. et al. (Sept. 2019). “SPHERE: the exoplanet imager for the Very Large Telescope”. In: *Astronomy & Astrophysics*.

Cantalloube, F. et al. (2018). “Origin of the asymmetry of the wind driven halo observed in high-contrast images”. In: *Astronomy & Astrophysics* 620, p. L10.

Chauvin, G. et al. (2017). "Discovery of a warm, dusty giant planet around HIP26". In: *Astronomy & Astrophysics* 605, p. L9.

Doelman, N., R. Fraanje, and R. den Breeje (2011). "Real-sky adaptive optics experiments on optimal control of tip-tilt modes". In: *2nd Conference on Adaptive Optics for Extremely Large Telescopes* 1.1.

Fusco, T. et al. (2016). "SAXO, the SPHERE extreme AO system: on-sky final performance and future improvements". In: *Adaptive Optics Systems V*. Ed. by Enrico Marchetti, Laird M. Close, and Jean-Pierre Véran. Vol. 9909. International Society for Optics and Photonics. SPIE, pp. 273–290.

Guyon, O. and J. Males (July 2017). "Adaptive Optics Predictive Control with Empirical Orthogonal Functions (EOFs)". In: *ArXiv e-prints*.

Guyon, Olivier (Aug. 2005). "Limits of Adaptive Optics for High-Contrast Imaging". In: *The Astrophysical Journal* 629.1, pp. 592–614.

Guyon, Olivier, Arnaud Sevin, et al. (2018). "The compute and control for adaptive optics (CACAO) real-time control software package". In: *Adaptive Optics Systems VI*. Ed. by Laird M. Close, Laura Schreiber, and Dirk Schmidt. Vol. 10703. International Society for Optics and Photonics. SPIE, pp. 469–480.

Haykin, Simon (2002). *Adaptive filter theory*. 4th. Upper Saddle River, NJ: Prentice Hall.

Jackson, Kate, Carlos Correia, Olivier Lardière, Dave Andersen, and Colin Bradley (Jan. 2015). "Linear prediction of atmospheric wave-fronts for tomographic adaptive optics systems: modelling and robustness assessment". In: *Opt. Lett.* 40.2, pp. 143–146.

Jensen-Clem, Rebecca, Charlotte Z. Bond, Sylvain Cetre, Eden McEwen, Peter Wizinowich, Sam Ragland, Dimitri Mawet, and James Graham (2019). "Demonstrating predictive wavefront control with the Keck II near-infrared pyramid wavefront sensor". In: *Techniques and Instrumentation for Detection of Exoplanets IX*. Ed. by Stuart B. Shaklan. Vol. 11117. International Society for Optics and Photonics. SPIE, pp. 275–284.

Kasper, Markus (2012). "Adaptive optics for high contrast imaging". In: *Proc.SPIE* 8447, pp. 8447 - 8447 –10.

Keppler, M. et al. (Sept. 2018). "Discovery of a planetary-mass companion within the gap of the transition disk around PDS 70". In: *Astronomy and Astrophysics* 617, A44.

Kooten, Maaike van, Niek Doelman, and Matthew Kenworthy (May 2019). "Impact of time-variant turbulence behavior on prediction for adaptive optics systems". In: *J. Opt. Soc. Am. A* 36.5, pp. 731–740.

— (2020). "Robustness of prediction for extreme adaptive optics systems under various observing conditions - An analysis using VLT/SPHERE adaptive optics data". In: *Astronomy and Astrophysics* 636, A81. DOI: 10.1051/0004-6361/201937076. URL: https://doi.org/10.1051/0004-6361/201937076.

Le Roux, B., R. Ragazzoni, C. Arcidiacono, J.-M. Conan, C. Kulcsar, and H.-F. Raynaud (Oct. 2004). "Kalman-filter-based optimal control law for star-oriented and layer-oriented multiconjugate adaptive optics". In: *Proc.SPIE* 5490, pp. 1336–1346.

Milli, J. et al. (Sept. 2017). "Performance of the extreme-AO instrument VLT/SPHERE and dependence on the atmospheric conditions". In: *AO4ELT5*.

Noll, Robert J. (Mar. 1976). "Zernike polynomials and atmospheric turbulence∗". In: *J. Opt. Soc. Am.* 66.3, pp. 207–211.

Petit, C., J.-M. Conan, C. Kulcsár, H.-F. Raynaud, and T. Fusco (2008). "First laboratory validation of vibration filtering with LQG control law for Adaptive Optics". In: *Optics Express* 16, p. 87.

Petit, C., J.-F. Sauvage, et al. (2014). "SPHERE eXtreme AO control scheme: final performance assessment and on sky validation of the first auto-tuned LQG based operational system". In: *Adaptive Optics Systems IV*. Ed. by Enrico Marchetti, Laird M. Close, and Jean-Pierre Véran. Vol. 9148. International Society for Optics and Photonics. SPIE, pp. 214–230.

Poyneer, Lisa A. and Bruce A. Macintosh (Aug. 2006). "Optimal Fourier control performance and speckle behavior in high-contrast imaging with adaptive optics". In: *Opt. Express* 14.17, pp. 7499–7514.

Poyneer, Lisa A., Bruce A. Macintosh, and Jean-Pierre Véran (Sept. 2007). "Fourier transform wavefront control with adaptive prediction of the atmosphere". In: *J. Opt. Soc. Am. A* 24.9, pp. 2645–2660.

Sissa, E. et al. (2018). "New disk discovered with VLT/SPHERE around the M star GSC 07396-00759". In: *Astronomy & Astrophysics* 613, p. L6.

Sivo, Gaetano et al. (Sept. 2014). "First on-sky SCAO validation of full LQG control with vibration mitigation on the CANARY pathfinder". In: *Opt. Express* 22.19, pp. 23565–23591.

Zurlo, A. et al. (2016). "First light of the VLT planet finder SPHERE - III. New spectrophotometry and astrometry of the HR9 exoplanetary system". In: *Astronomy & Astrophysics* 587, A57.

“Don’t adventures ever have an end? I suppose not. Someone else always has to carry on the story”.

J.R.R. Tolkien,
The Fellowship of the Ring

List of Publications

First Author, Peer Reviewed:

Maaike van Kooten, Niek Doelman, et al. (2020a). "Brightening of Kepler light curves: from binary star systems to forward scattering dust clouds". In: *Under review*

Maaike van Kooten, Niek Doelman, et al. (2020b). "Robustness of prediction for extreme adaptive optics systems under various observing conditions - An analysis using VLT/SPHERE adaptive optics data". In: *Astronomy and Astrophysics* 636, A81. DOI: 10.1051/0004-6361/201937076. URL: https://doi.org/10.1051/0004-6361/201937076

Maaike van Kooten, Niek Doelman, et al. (May 2019). "Impact of time-variant turbulence behavior on prediction for adaptive optics systems". In: *J. Opt. Soc. Am. A* 36.5, pp. 731–740

Maaike van Kooten, Jean Pierre Veran, et al. (2017). "Alternative pyramid wavefront sensors". In: *Journal of Astronomical Telescopes, Instruments, and Systems* 3.2, p. 029001

Conference Proceedings

Maaike van Kooten, Niek Doelman, et al. (2018). "Implications for contrast as a result of the wind vector and non-stationary turbulence". In: *Adaptive Optics Systems VI*. vol. 10703. International Society for Optics and Photonics, p. 107032C

Maaike van Kooten, Niek Doelman, et al. (2017). "Performance of AO predictive control in the presence of non-stationary turbulence". In: Instituto de Astrofisica de Canarias

Maaike van Kooten, Colin Bradley, et al. (2016). "Fast modulation and dithering on a pyramid wavefront sensor bench". In: *Adaptive Optics Systems V*. vol. 9909. International Society for Optics and Photonics, 99096G

Emiel H Por et al. (2018). "High contrast imaging for python (HCIPy): an open-source adaptive optics and coronagraph simulator". In: *Adaptive Optics Systems VI*. vol. 10703. International Society for Optics and Photonics, p. 1070342

John Pazder et al. (2014). "The FRD and transmission of the 270-m GRACES optical fiber link and a high numerical aperture fiber for astronomy". In: *Advances in Optical and Mechanical Technologies for Telescopes and Instrumentation*. Vol. 9151. International Society for Optics and Photonics, p. 915124

Etsuko Mieda et al. (2016). "Testing the pyramid truth wavefront sensor for NFIRAOS in the lab". In: *Adaptive Optics Systems V*. vol. 9909. International Society for Optics and Photonics, 99091J

Olivier Lardière et al. (2017). "Double-Pyramid Wavefront Sensors: Tolerance Relaxation and Cheaper Alternatives using Achromatic Double-Roof Prisms". In: *Adaptive Optics for Extremely Large Telescopes V (AO4ELT5)*

SY Haffert et al. (2018). "On-sky results of the Leiden EXoplanet Instrument (LEXI)". in: *Adaptive Optics Systems VI*. vol. 10703. International Society for Optics and Photonics, p. 1070323

List of Selected Presentations

2019

Performance of different wavefront predictors for SPHERE AO. AO4ELT6. June 2019. Quebec City, Canada (Poster)

Instrumentation at Leiden Observatory: from liquid crystals to control. Herzberg Institute of Astrophysics, National Research Council. April 2019. Victoria, Canada (Oral)

2018

Predictive control for High Contrast Imaging. NYRIA Workshop. October 2018. Leiden, The Netherlands. (Oral)

Seeing the future. Leiden Observatory Science Day. September 2018. Leiden, The Netherlands. (Oral)

Implications for contrast as a result of the wind vector and non-stationary turbulence. SPIE Astronomical Telescopes & Instrumentation. June 2018. Austin, United States. (Oral)

Toward modelling non-stationary turbulence. March 2018. Wavefront sensing and control for AO Workshop. Durham, England. (Oral)

Seeing through the atmosphere: How to get the most out of a ground-based telescope. Open Seminar Series Geoscience & Remote Sensing. May 2018. Delft, The Netherlands. (Oral)

2017 & earlier

Pupil plane wavefront sensor technologies at Leiden Observatory. Face2Phase Conference. October 2017. Delft, The Netherlands (Oral)

Performance of AO predictive control in the presence of non-stationary turbulence. AO4ELT5 Conference. June 2017. Tenerife, Spain (Poster)

Fast modulation and dithering on a pyramid wavefront sensor bench. SPIE Astronomical Telescopes & Instrumentation. June 2016. Edinburgh, Scotland. (Poster)

Curriculum Vitae

Born to Gerrit and Mary van Kooten in Richmond, Canada, on 20 July 1992, I am the 3rd of 4 daughters. Growing up, my father, a professor in land-use and agricultural economics, had a part time appointment at Wageningen University & Research, meaning that my family spent time in Wageningen where I attended peuterspeelzaal and later basisschool (Group 3). At the age of 9, we moved from Richmond to Reno, USA. Here, I have my first memories of enjoying arithmetic and typing classes. Moving back to Canada, (Victoria), my parents enrolled me in French immersion as I was bored in normal classes. For the next 3 years I fully enjoyed science, maths, and learning French. My teachers inspired me to explore many topics outside of the curriculum, which led to me presenting a science project on nuclear fusion and the life-cycle of stars.

I attended Lambrick Park High school, where I took all the mathematics and science courses offered, while spending much of my spare time playing sports including Judo, and field hockey. While I had always enjoyed physics, and had a fascination for stars for as long as I could remember, I was convinced I would enter into a Bachelor program in pure mathematics.

In September 2010, I started my Bachelor's program in Physics and Astronomy at the University of Victoria (UVic) after my mother encouraged me to look at other programs beside mathematics. Supplementary to my classroom work, I completed three work terms at the Herzberg Institute of Astrophysics (HIA). My first position was in the visitor center where I gave telescope tours, prepared education material, and led science camps for kids. I subsequently worked on analysing sub-millimetre data, followed by working in the fiber optics laboratory. As a 4th-year project, I looked for transit events around white-dwarfs with the local 1.8 m telescope. Through these experiences and the people I met at HIA, I knew that astronomy instrumentation was the field for me. I began my Master's of Applied Science degree in UVic's Mechanical Engineering department in 2014, with Colin Bradley as my supervisor. I performed initial work on the wavefront sensing setup to be used by the Thirty Meter Telescope's AO system, investigating different implementations of pyramid wavefront sensors.

In September 2016, I returned to the Netherlands to start my PhD at Leiden Observatory. Working with Niek Doelman and Matthew Kenworthy, my research topic was predictive control for extreme AO systems found in high-contrast imaging instruments. With full control over the direction of my research, I have explored topics including atmospheric turbulence profiling and simulations, as well as linear data-driven prediction, and performed tests on VLT/SPHERE AO data.

I will begin the next stages of my career in astronomy instrumentation as a postdoctoral researcher at the University of California, Santa Cruz, in October 2020. There I will continue exploring AO control and perform on-sky tests at the Keck Telescope.